Experimental Parameter Study of the Richtmyer-Meshkov Instability

Bradley J. Motl

August 2008

UWFDM-1379

Ph.D. thesis.

FUSION TECHNOLOGY INSTITUTE

UNIVERSITY OF WISCONSIN

MADISON WISCONSIN

Experimental Parameter Study of the Richtmyer-Meshkov Instability

Bradley J. Motl

Fusion Technology Institute
University of Wisconsin
1500 Engineering Drive
Madison, WI 53706

http://fti.neep.wisc.edu

August 2008

UWFDM-1379

Ph.D. thesis.

Experimental Parameter Study of the Richtmyer-Meshkov Instability

By

Bradley J. Motl

A dissertation submitted in partial fulfillment of the requirements for the degree of

Doctor of Philosophy

(Nuclear Engineering & Engineering Physics)

at the

UNIVERSITY OF WISCONSIN – MADISON

2008

Abstract

An experimental parameter study of the Richtmyer-Meshkov (RM) instability for a sinusoidal, membraneless interface is carried out in a vertical shock tube for a range of Atwood numbers ($A = (\rho_1\text{-}\rho_2)/(\rho_2+\rho_1)$), $0.29 < A < 0.95$, and shock strengths, $1.1 < M < 3$. The RM instability occurs when a perturbed interface between two fluids of differing densities is impulsively accelerated, and ultimately leads to the turbulent mixing of the two fluids. The instability is of interest to researchers in the fields of inertial confinement fusion, astrophysics, and hypersonics where the turbulent mixing may enhance or degrade a desired or observed result. The current study utilizes planar imaging techniques to diagnose a nearly single-mode, two-dimensional gas interface. Amplitude growth rates in the linear and nonlinear regimes are measured and compared to several analytic models and the hydrodynamics code *Raptor* (LLNL).

Results are presented for eight scenarios which include three interface gas pairs. The initial condition for each gas pair is characterized, and results indicate that the interface is predominantly single-mode and two-dimensional for a specified region of interest within the shock tube. Shocked interface visualization results reveal the presence of qualitatively different features and growth rates for each Mach/Atwood number scenario. Experimental data, presented in both dimensional and non-dimensional formats, compares well with single-mode results from *Raptor*. The non-dimensional scaling collapse the experimental data to a single line from early to moderate non-dimensional times. The experimental and *Raptor* amplitude growth rate data show best agreement with a model proposed by Mikaelian across the studied parameter space.

Acknowledgements

First and foremost I would like to thank the University of Wisconsin-Madison and the Department of Engineering Physics for giving me an opportunity to study Nuclear Engineering & Engineering Physics at a world class teaching and research institution. Moreover, I thank Professor Riccardo Bonazza for giving me an opportunity to conduct research at the Wisconsin Shock Tube Laboratory, and being a supportive and caring advisor. His wisdom has gone far beyond the bounds of the shock tube laboratory.

I have been blessed to have such a wonderful research group. I can not thank enough, scientists Dr. Jason Oakley and Dr. Mark Anderson for always being willing to help me work through problems I encountered while conducting experiments or analyzing data. The research contained within this thesis could not have been realized without the help of Dr. Devesh Ranjan. At all hours of the day, Dr. Ranjan has been willing to help me run experiments and troubleshoot the plethora of problems that arose. I really cherish the friendship we forged working day in and day out in the laboratory. A big thanks goes to Paul Brooks for always keeping the laboratory running smoothly and being willing to drop what he was working on to help me. I always appreciated his friendly ribbing of graduate students in the machine shop. I would like to give a special thanks to Dr. John Neiderhaus and Chris Weber who have always been willing and able to run numerical simulations for my research, while also being willing to lend a hand in the laboratory whenever needed. Likewise, I would like to thank Nick Haehn and Trevor Bauer for helping me run experiments and Jeremy White for his computer programming advice.

I love the city of Madison, and there certainly have been a lot of additional folks who have made my time as a graduate student special. There are too many people to name, however, there are a few that have been particularly important to me. So, a special thanks goes to: Alan, Dave, Julie, Sara, Hannah, Scott, Erin, Kris, Nick, Karl, EW and DP.

My biggest thanks goes to my wife Sarah, and parents: John, Carolyn, Jim, and Jo. They have always encouraged me to dream big, and to follow my dreams no matter how many twists and turns they create in life. Their love and support are unmeasurable, and I greatly appreciate that. Lastly, I would like to thank my dog, Rooney, who never lets me enter or leave the apartment without a smile on my face.

This work was supported by the U.S. Department of Energy Grant No. DE-FG52-06NA26196 and a Sandia National Laboratories Graduate Fellowship.

Contents

List of Figures

List of Tables

Nomenclature

Abbreviations

AMR	Adaptive mesh refinement
D	Deuterium
FFT	Fast Fourier transform
ICF	Inertial confinement fusion
MM	Multimode
PLIF	Planar laser-induced fluorescence
PT	Pressure transducer
RT	Rayleigh-Taylor
RM	Richtmyer-Meshkov
SM	Single mode
T	Tritium

English Symbols

A	Pre-shock Atwood number across the interface
A^1	Post-shock Atwood number across the interface
$\bar{A}$	Average of the pre- and post-shock Atwood number

c	Sound speed in a given gas
D_{ab}	Diffusion coefficent
k	Wave number
m	Number of objects in a set
M	Mach number of incident shock wave
M_t	Mach number of transmitted shock wave
M_{tr}	Interface Mach number
P	Pressure
Re	Reynolds number
S	Standard deviation
t	Time after shock traverses the interface
T	Temperature
$\mathbf{U}$	Velocity vector
u_t	Transmitted shock wave fluid velocity
u_2	Incident shock wave fluid velocity
V_0	Interface velocity
V_D	Outflow gas velocity
W_i	Incident shock wave speed

W_r Reflected shock wave speed

W_t Transmitted shock wave speed

Greek Symbols

α Non-dimensional amplitude

δ Pre-shock diffusion thickness

δ^1 Post-shock diffusion thickness

$\bar{\delta}$ Average of pre- and post-shock diffusion thickness

η Perturbation amplitude

η_S Spike amplitude

η_0^0 Pre-shock initial perturbation amplitude

η_0^1 Post-shock initial perturbation amplitude

$\dot{\eta}_0$ Initial perturbation growth rate

$\dot{\eta}_\psi$ Initial perturbation growth rate

$\dot{\eta_\infty}$ Asymptotic bubble velocity

$\dot{\eta}$ Perturbation growth rate

$\dot{\eta}_C$ *Raptor* continuous growth rate

$\dot{\eta}_D$ *Raptor* discontinuous growth rate

η^* Meyer and Blewett initial perturbation amplitude

Γ	Circulation
λ	Wavelength
μ	Dynamic viscosity
ν	Kinematic viscosity
ψ_E	Calculated growth reduction factor
ψ_R	*Raptor* growth reduction factor
ρ	Diffusion profile
ρ_1	Heavy gas density
ρ_2	Light gas density
σ_{ab}	Characteristic Lennard-Jones length
τ	Non-dimensional time
τ_D	Characteristic diffusion time
τ_A	Particle travel time
τ_B	Outflow off time
ω	Vorticity vector
Ω_D	Diffusion collision integral

Chapter 1

Introduction

The Richtmyer-Meshkov instability is a hydrodynamic instability that results from the misalignment of density and pressure gradients across a fluid interface perturbation due to the application of an impulsive acceleration. This results in the time dependent growth of the initial perturbation, and eventually leads to the turbulent mixing of the gases. The main motivation behind the current study is to understand the physics behind the rate at which the gases mix, and to create a broad set of experimental data that can be used to provide validation data for numerical computer codes in a wide variety of research areas. Specifically, the effect of Atwood number and shock wave strength on the perturbation growth rate will be studied, in an effort to establish an universal scaling law that is suitable to describe these effects.

1.1 The Richtmyer-Meshkov Instability

The foundation for the Richtmyer-Meshkov instability was formed by Lord Rayleigh's [43] initial work on stability in fluids of different density in the late 1800's. In 1950, G.I. Taylor [55] developed a theory for the growth of a fluid interface perturbation under the influence of a constant acceleration (such as gravity) normal to the initial interface. In 1960 Richtmyer [47] expanded upon Taylor's original theory by taking into consideration an impulsive acceleration acting on the interface. Richtymer's theory was then qualitatively confirmed by shock tube experiments performed by Meshkov [33] in 1969. This class of problems is now known as the Richtmyer-Meshkov (RM) instability.

1.1.1 Richtmyer Theory

Richtmyer's study of the shocked gas interface problem started with an initial condition that consisted of a sine wave interface between two incompressible and inviscid fluids. It is assumed that the interface has no surface tension. As seen in Fig. 1, the initial shock wave is traveling downward in the $-z$ direction with an initial Mach number M, traversing the interface from the lighter fluid to the heavier fluid.

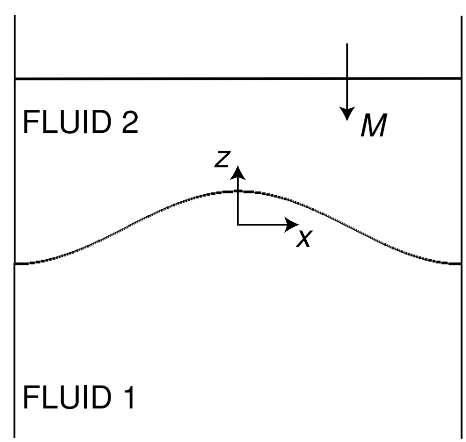

Figure 1: Initial gas interface with sinusoidal perturbation before being traversed by a planar shock wave.

The initial interface is described by:

$$\eta = \eta_0 \cos(kx), \tag{1.1}$$

where η_0 is the initial amplitude of the perturbation and k is the wavenumber. For the linear analysis that Richtmyer presented, the initial amplitude of the perturbation is much smaller than the wavelength, *i.e.* $k\eta_0 << 1$, where $k = 2\pi/\lambda$. It then followed from Taylor's work [55], with the addition of a time varying acceleration $g(t)$, that the growth or dampening of the initial amplitude with respect to time can be found from the following differential equation:

$$\frac{d^2}{dt^2}\eta(t) = kg(t)\eta(t)A, \tag{1.2}$$

where A is the Atwood number given by:

$$A = \frac{\rho_1 - \rho_2}{\rho_2 + \rho_1}, \tag{1.3}$$

where ρ_2 is the density of the top gas and ρ_1 is the density of the bottom gas.

In the case of a shock wave, the time varying acceleration, $g(t)$, is impulsive due to the shock wave being discontinuous in thermodynamic and kinematic states. This means that $g(t)$ is large over a very short period of time, and zero at all other times, and may be represented mathematically by the Dirac delta function. The velocity imparted by this acceleration is then given by:

$$V_0 = \int g(t)dt. \tag{1.4}$$

For the case described by Richtmyer, the acceleration occurs in the $-z$ direction and V_0 is negative. The initial perturbation amplitude and growth rate before the acceleration are then:

$$\eta = \eta_0^0, \qquad \frac{d\eta}{dt} = 0, \tag{1.5}$$

and the amplitude and growth rate immediately post-shock are given by:

$$\eta = \eta_0^0, \qquad \frac{d\eta}{dt} = -kV_0\eta_0^0 A, \tag{1.6}$$

where η_0^0 is the pre-shock perturbation amplitudes and A is the pre-shock Atwood number.

Richtmyer then developed a set of linearized equations with appropriate initial and boundary conditions that maintained the same assumptions as the the impulsive model, except the fluids were now assumed to be compressible. Once these equations were solved numerically, amplitude growth rate versus time plots were produced. In all of the cases presented, the growth rate grew in time until it reached a point where it oscillated with decreasing amplitude about a limiting value. Richtmyer [47] ultimately concluded that when the compression of the interface and the fluids was taken into account, the growth rate of the perturbation predicted by his initial model (Eq. (1.6)) agreed to within 5 to 10% of the impulsive, incompressible theory. Therefore, Eq. (1.6) was modified such that the amplitude and growth rate immediately post-shock becomes:

$$\eta = \eta_0^1, \qquad \frac{d\eta}{dt} = -kV_0\eta_0^1 A^1, \tag{1.7}$$

where η_0^1 is the post-shock perturbation amplitude and A^1 is the post-shock Atwood number. Meshkov [33] later estimated the post-shock amplitude to be:

$$\eta_0^1 = \eta_0^0\left(1 - \frac{|V_0|}{Mc}\right), \tag{1.8}$$

where c is the speed of sound in the light fluid and M is the incident Mach number. The formulation of the amplitude growth rate given in Eq. (1.7) is referred to as the "impulsive model." When the shock wave moves from a light gas toward a heavy gas the Atwood number is positive, and therefore, the growth rate is positive. When the shock wave goes from a heavy gas to a light gas the Atwood number is negative, and the initial growth rate is negative. This corresponds to a phase inversion of the interface.

1.1.2 Instability Evolution

The evolution of the Richtmyer-Meshkov instability begins when the incident shock wave traverses the perturbed interface and deposits vorticity on the interface due to a non-zero baroclinic vorticity source term embedded within the vorticity equation derived from the Navier-Stokes equations. Vorticity is defined as the curl of the velocity:

$$\boldsymbol{\omega} \equiv \nabla \times \mathbf{U}. \tag{1.9}$$

The curl of the compressible Navier-Stokes equation results in the vorticity transport equation, which is given as:

$$\frac{D\boldsymbol{\omega}}{Dt} = (\boldsymbol{\omega} \cdot \nabla)\,\mathbf{U} - \boldsymbol{\omega}\,(\nabla \cdot \mathbf{U}) + \frac{1}{\rho^2}\,(\nabla\rho \times \nabla p) + \nu\nabla^2\boldsymbol{\omega}. \tag{1.10}$$

The first term on the right hand side is the vortex stretching term. This term is important in three-dimensional flows where vortex lines are influenced by velocity gradients. The second term is the vortex dilatation term, which describes how fluid compressibility affects vorticity. The third term is the baroclinic source term which accounts for vorticity generated by the misalignment of pressure and density gradients. The last term indicates the rate at at which vorticity changes due to diffusion of the vorticity. At time zero, before the shock wave traverses the interface, $\boldsymbol{\omega}= 0$. Therefore, at time zero, Eq. (1.10) reduces to:

$$\frac{D\boldsymbol{\omega}}{Dt} = \frac{1}{\rho^2}\,(\nabla\rho \times \nabla p)\,, \tag{1.11}$$

which indicates that the Richtmyer-Meshkov instability is initially driven by baroclinic vorticity generation due to the shock wave traversing the interfacial density gradient. The vorticity from $-\pi < x < 0$ is positive, and of the same magnitude but opposite sign from $0 < x < \pi$, as depicted in Fig. 2.

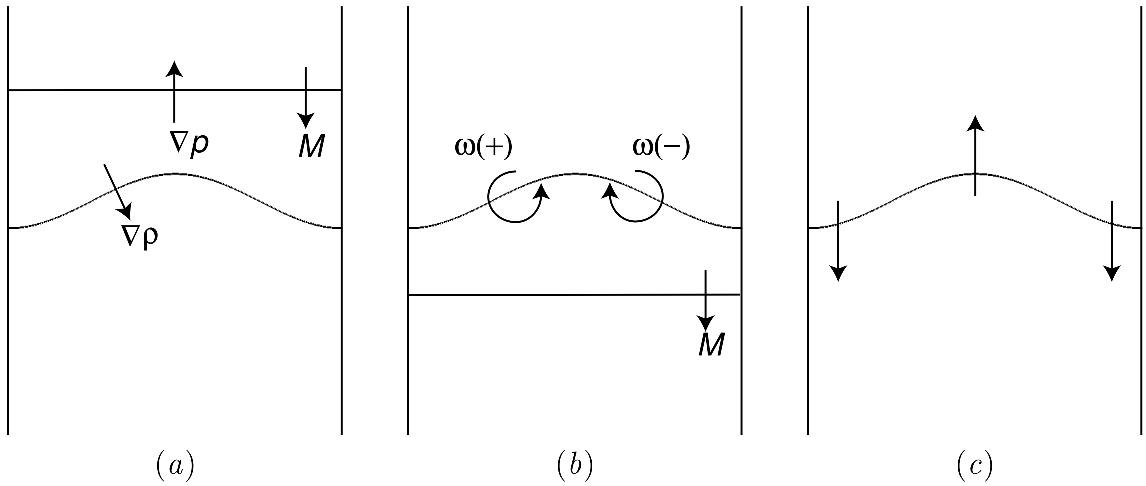

Figure 2: Vorticity deposition on a light-over-heavy gas interface due to an incident planar shock wave. (a) Initial configuration. (b) Direction of deposited vorticity. (c) Direction of initial interface growth.

At first, the deposited vorticity causes the initial amplitude of the perturbation to grow linearly in time as the vorticity facilitates the movement of fluid between the bubble and the spike. The linear amplitude growth is followed by a nonlinear growth regime which is characterized by the asymmetric "spiking" of the heavy fluid into the lighter fluid, while the light fluid appears to "bubble" into the heavy fluid [6]. The nonlinear growth is followed by a regime that is influenced by the Kelvin-Helmholtz instability, which causes roll-up structures on each side of the heavy fluid spike and results in the formation of mushroom-looking structures, as shown in Fig. 3. At late times, secondary small scale structures due to the Rayleigh-Taylor (RT) and Kelvin-Helmholtz instabilities develop on the interface, which ultimately lead to a turbulent mixing zone.

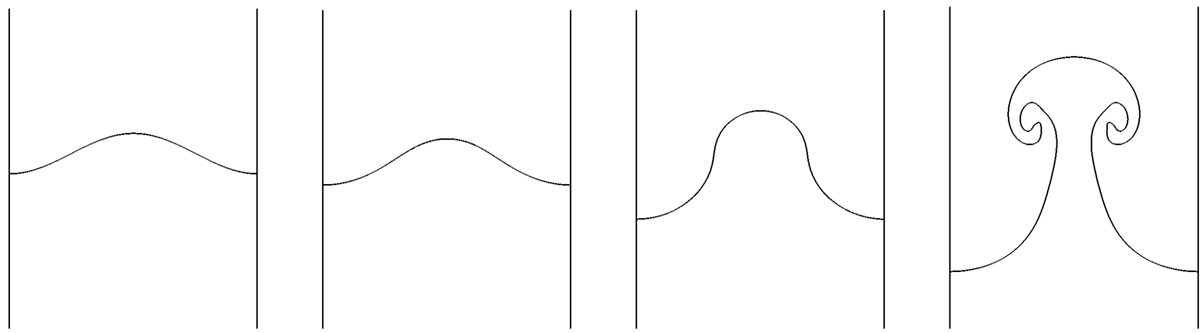

Figure 3: Evolution of the Richtmyer-Meshkov instability. (a) Initial configuration. (b) Linear growth regime. (c) Start of nonlinear growth. (d) Appearance of mushroom structures.

1.1.3 Meshkov Experiments

In 1969, Meshkov [33] presented an experimental study of the instability proposed by Richtmyer [47]. The experiments were performed in a cylindrical shock tube with an internal diameter of 208 mm and a length of 4 m. The driver (pressurized to 6.5 atm) and driven (at 1 atm) sections of the tube were separated by a diaphragm consisting of four layers of cellulose acetate film, each being 0.2 mm thick. The diaphragm was ruptured by an exploding electric wire and resulted in a shock strength of approximately M=1.5 in air.

The test section of the shock tube was rectangular with an inner section of 120 mm $\times$ 40 mm, and extended 0.7 m into the driven section. A nearly sinusoidal interface was then created by separating the driven and test gases with a 1 μm thick nitrocellulose film. Experiments were performed with $\lambda = 40$ mm and $\eta_0 = 2$ or 4 mm resulting in a $k\eta_0$ of 0.314 and 0.628 respectively, which does not necessarily satisfy Richtmyer's linear theory condition of $k\eta_0 << 1$. The test gases were filled by gravity flow and the purity was verified by recording changes in the capacitance of an air-gap condenser. Gravity flow is a process for filling the test section by feeding the heavier than air gas from below the section and feeding the lighter than air gas from above [33], thus relying on gravitational stratification to keep the gases from mixing. Experiments were performed with a variety of gas pairings that included air, He, CO_2, and Freon-22, and were diagnosed with a Schlieren setup coupled with a SFR-3M high speed camera.

Meshkov's experimental campaign was able to verify the existence of the instability proposed by Richtmyer. The interface was unstable for both the light over heavy gas and the heavy over light gas configurations. When the shock traveled from heavy to light gas, a phase change in the initial perturbation was noticed. Meshkov also found that the interface velocity changed abruptly and remained relatively constant after the shock wave traversed the perturbation.

Meshkov's experiments were in qualitative agreement with theory, however, good quantitative agreement between the experiment and theory could not be achieved due to shortcomings in the experiment. First and foremost, Richtmyer's linear theory condition of $k\eta_0 << 1$ was not met. In addition, low resolution of the optical system and interfacial diffusion affected the ability to make precise measurements. Film porosity and impurities (absolute purity could not be ensured by the capacitance technique described above) in the test gases could have resulted in altered growth rates. The experimentally determined growth rate was much lower than the growth rate determined by Richtmyer's impulsive theory.

In 1972, Meyer and Blewett [34] simulated Meshkov's experiments using a two-dimensional Lagrangian hydrodynamic code. They found that for the case of a shock traveling from a heavy to a light gas (A<0), Eq. (1.7) must be modified. They recommended that the initial post-shock amplitude, η_0^1, be replaced by η^*, where η^* is given as:

$$\eta^* = \frac{\eta_0^1 + \eta_0^0}{2}. \tag{1.12}$$

1.2 Applications

In the context of the current study, the application that is of most importance is the shock wave induced mixing of the fuel pellet with the ablator in inertial confinement fusion. In this application, the Atwood number approaches a value of one [4]. The RM instability also plays an important role in some astrophysical and hypersonic applications.

1.2.1 Inertial Confinement Fusion

Nuclear fusion is the process of combining multiple small atomic nuclei in order to create a larger nucleus. In the process, energy is released because the mass of the combined nucleus is less than the sum of the individual nuclei combined. The fusion reaction that is currently receiving the most attention for use in fusion reactors is the deuterium-tritium reaction due to its large reaction cross section. Deuterium (D) is a stable hydrogen isotope with one proton and one neutron, and tritium (T) is a radioactive hydrogen isotope with one proton and two neutrons. The D-T fusion reaction results in the production of a 3.5 MeV helium atom and a 14.1 MeV neutron:

$$\mathrm{D} + \mathrm{T} \rightarrow {}^4\mathrm{He}\ (3.5\ MeV) + \mathrm{n}\ (14.1\ MeV). \tag{1.13}$$

The energy of the neutrons is converted into heat (due to collisions with an attenuating medium), which may then be used for power production (*e.g.* by producing steam). Due to its short half-life, Tritium does not exist in large natural quantities, so it must be created by the reaction:

$$^{6}\mathrm{Li} + \mathrm{n} \rightarrow \mathrm{T} + {}^{4}\mathrm{He}\ . \tag{1.14}$$

A lithium (Li) compound blanket (surrounding the reactor chamber) is bombarded with neutrons that are produced in the initial fusion reaction [39]. Thus, D and Li are the primary fuels in the fusion system.

Ongena and Van Oost [39] concluded that fusion energy had many advantages over other major energy sources. The fuel (D and Li) is abundant, cheap, non-radioactive, and the extraction does not cause any significant ecological problem. Fusion reactors are inherently safe due to the passive nature of the reaction, therefore, an uncontrollable chain reaction is not possible. Lastly, the environmental impacts of fusion energy production are minimal. There is very little generation of greenhouse gases, and although shielding must be provided for the high energy neutrons, there is no direct radioactive waste produced.

The only places where the reaction in Eq. (1.13) occurs in nature, is where there are sun-like conditions. One method for facilitating the D-T fusion reaction on Earth is through inertial confinement fusion (ICF). In ICF, the D-T fuel is stored as a gas within a shell of solid D-T, which is surrounded by an ablative shell (see Fig. 4), which is several millimeters in diameter [29]. The process begins with large amounts of energy being deposited on the outside of the fuel pellet by either lasers, x-rays, or accelerated particles. This causes the ablator shell to ablate (absorb energy and blow off in a direction normal to the surface of the target [38]), and the D-T fuel to implode. The implosion causes the fuel to be confined to the center of the pellet, which allows for the high pressures and temperature needed to achieve fusion.

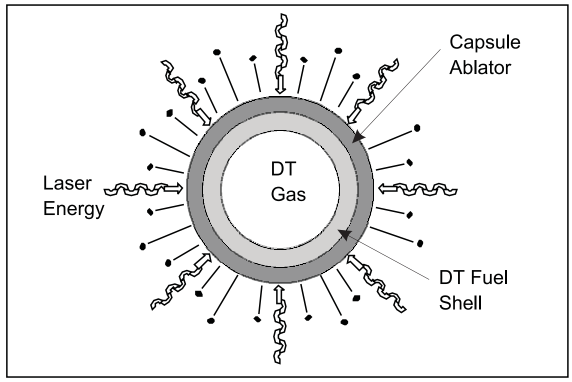

Figure 4: The deposition of energy on an inertial confinement fusion target, figure taken from Oakley [38].

The RM and RT instabilities play a vital role in the hydrodynamic mixing of the imploding fuel. Due to manufacturing limitations, there will be small perturbations on the interface between the ablator and the solid D-T fuel, and the interface between the solid D-T fuel and the gaseous D-T fuel. These small perturbations, when traversed by a shock wave, result in the distortion of the spherical symmetry and can either lead to a lower fusion energy yield or a failure of the reaction to occur at all. The present experimental shock tube study decouples the hydrodynamic instabilities from the effects of radiation and plasma.

1.2.2 Astrophysics

For the case of a supernova, the star's core collapses until it reaches a saturated nuclear density where the pressure is large enough to stop the influx of collapsing material. The inner core then acts like a piston and creates what is referred to as a "bounce," which creates a shock wave, and reverses the collapsing motion of the outer core [50]. The Richtmyer-Meshkov instability plays a role in the mixing of Rayleigh-Taylor unstable features known as "fingers" and "bullets" [25], [53], [54] that interact with the shock wave created by the core bounce. In general, the RM instability occurs in many circumstellar and interstellar environments where shocks interact with density non-uniformities [15].

1.2.3 Hypersonics

The Richtmyer-Meshkov instability can play a favorable role in the field of hypersonics, unlike the detrimental role it plays in the inertial confinement fusion application. The development of hypersonic vehicles depends on the technology of supersonic combustion ramjet (scramjet) engines. Scramjet engine efficiency depends on the mixing of hydrogen and air at high flow velocities (2,000 to 4,500 m/s) and short time scales (1 ms) [58]. It has been suggested that shock waves within the flow field may help to seed the hydrogen-air interface with baroclinic vorticity which leads to turbulent mixing and chemical reactions between the fuel and oxidizer [31].

Chapter 2

Previous Work

A limited volume of work has been performed in the Richtmyer-Meshkov (RM) field. Due to a variety of experimental methods utilized in the past, the following is a review of the most relevant previous results with respect to the current experimental campaign. In addition, several analytical models that will be compared to current results are discussed in detail.

2.1 Experimental Review

Previous experiments performed at Los Alamos National Laboratory and the University of Arizona are the most similar to the current study because they utilized an initial interface without any physical barrier between the gases. Previous work at the University of Wisconsin-Madison is applicable because strongly shocked gas interfaces were studied. Laser driven experiments performed on the Nova laser at Lawrence Livermore National Laboratory have studied the RM instability for solid targets at $M>10$.

2.1.1 Los Alamos National Laboratory

The evolution of the Rictmyer-Meshkov instability has been studied for the case of a thin fluid layer by Jacobs *et al.* [21], [22], [23], Budzinski *et al.* [8], and Rightley *et* *al.* [48], [49] in a horizontal shock tube. This method involved the flow of a heavy gas curtain within a shock tube filled with a light gas. The gas curtain utilized a contoured nozzle that created a spatially modulated planar gas jet with a sinusoidal perturbation on both sides of the curtain, which created two separate gas interfaces. One interface occurred at the boundary between the ambient light gas and the heavy gas jet. The other interface occurred at the boundary between the other side of the vertical jet and the light gas. The heavy gas then exited the shock tube through an outlet slot that prevented contamination of the light gas. For all of the experiments performed, the heavy gas was SF_6, the lighter gas was air, and the stock strength was M=1.2. Jacobs *et al.* [21], [22], [23] utilized planar laser-induced fluorescence (PLIF) to diagnose their experiment. The SF_6 was seeded with diacetyl vapor and only one image per experiment was obtained. Budzinski *et al.* [8] obtained two images per experiment and visualized with planar Rayleigh scattering. Rightley *et al.* [48], [49] seeded the SF_6 with fog particles to enhance the light scattering, and a sequence of up to 32 images was obtained for each experiment.

All of the research indicated that three distinct growth patterns emerged as a result of the shock wave traversing the curtain, depending on the precise initial condition of the curtain at the instant it was accelerated [8]. In approximately 40% of the experiments, a sinuous pattern developed, about 50% of the time upstream mushrooms formed, and about 10% of the time downstream mushrooms developed. Rightley [48] presented results of an initial condition superposed with a half wavelength and an initial condition with two modes. The presence of the two mode interface accelerated the onset of the mixing, whereas, the effect of the superposed half wavelength depended on whether the perturbation was concave or convex relative to the planar shock wave [48].

2.1.2 University of Arizona

The Rictmyer-Meshkov instability has been studied for the case of an air (or nitrogen)-sulfur hexafluoride, membraneless gas interface. The experiments were performed by Jones and Jacobs [24], Collins and Jacobs [10], and Jacobs and Krivets [19]. Each of these experiments utilized a vertical shock tube that is 4.3 m long (1 m long, 10.2 cm diameter driver section and a 3.3 m long, 8.9 cm square driven section). The shock tube was modified for the Jacobs and Krivets experiment by increasing the driver length to 2 m. The driver section was constructed of glass fiber wound around a circular epoxy pipe, whereas, the driven section was made of square fiberglass tubing. All but one of the test section walls were made of flat black anodized aluminium, the other wall was constructed of transparent acrylic which permitted the optical access that was needed for flow visualization [10].

The membraneless interface was created by flowing a light gas from the upper end of the shock tube driven section and a heavy gas from the lower end. At the interface location, the gases collided and exited through slots in the shock tube. This produced a stagnation surface, which minimized the diffusion layer of the flat interface [24]. A sinusoidal perturbation was then created by oscillating the entire shock tube about a pivot point with a crank connected to a stepper motor running at a frequency that was pre-determined to create a standing wave [10]. The experimental setup can be seen in Fig. 5, where the stepper motor is just above the interface.

The flow was visualized in the case of Collins and Jacobs experiments by planar laser-induced fluorescence (PLIF). The light gas (either air or N_2) was seeded with acetone vapour, which fluoresces in the visible spectrum when UV light in the 225-320 nm range is incident upon it [30]. One post shock image was taken for each experiment with a

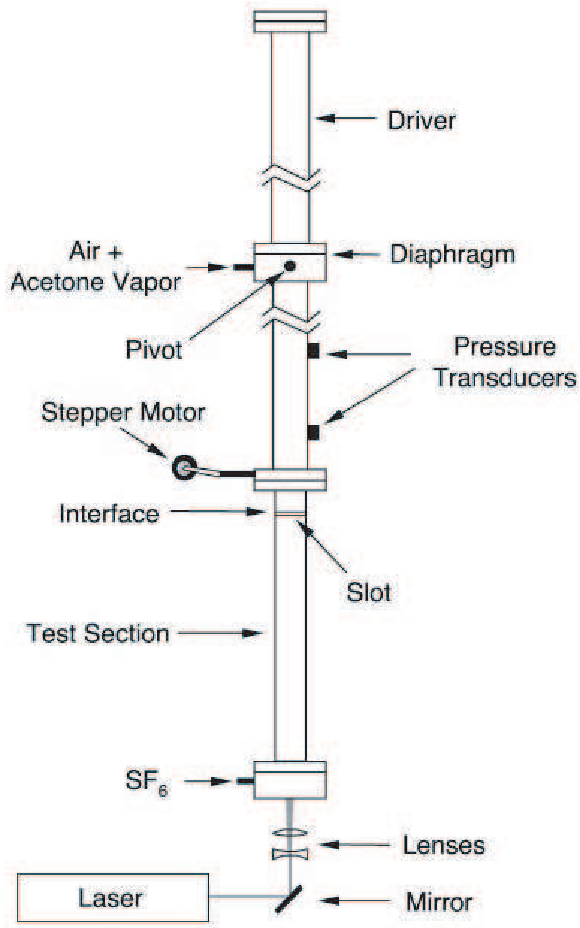

Figure 5: The University of Arizona experimental setup, figure taken from Jacobs and Krivets [19].

CCD camera.

The Jones and Jacobs [24] experiment was visualized by seeding the heavy gas with a fog, consisting of water droplets, that was produced by an ultrasonic atomizer. A strobe light was used to create a light sheet that scattered off of the water droplets. One post shock image was captured per experiment by a 35 mm camera.

Experiments were performed for a N_2 over SF_6 interface at M=1.10 [24], an air over SF_6 interface at M=1.11 and 1.21 [10], and an air over SF_6 interface at M=1.27 and 1.29 [19]. For each of these cases, a time sequence of corrected images was displayed that shows the evolution of the RM instability. Growth rate measurements were obtained and plotted both dimensionally and non-dimensionally. These measurements were compared to several analytical models. Among these, the Sadot *et al.* [51] model predicted the experimental data most accurately [10], [19].

2.1.3 University of Wisconsin-Madison

At the University of Wisconsin-Madison, a shock tube was constructed specifically for the shock-interface interaction and shock diffraction studies [3]. It will be described in detail in Section 3.1.

Richtmyer-Meshkov experiments have been performed by Puranik *et al.* [40] and Oakley [38]. Both of these experiments utilized a retractable plate to create a membraneless gas interface. The retractable plate was made out of copper and had a preformed sinusoidal shape. During the experiment, the shock wave was triggered at a specific time during the retraction of the copper plate.

The method of flow visualization for these experiments was planar Mie scattering, where laser light was scattered from submicron sized cigarette smoke particles. The smoke was injected into the shock tube from two ports and given ample time to uniformly mix with the test gas. The reflected light produced by the Mie scattering was collected with a CCD camera.

Puranik [40] studied a carbon dioxide over air gas interface accelerated by a M=3.08 shock wave. The initial condition was studied and characterized in a separate set of experiments, because they were limited to one image per an experiment. A late time evolution of the RM instability was presented in a sequence of images. Amplitude versus time plots were obtained and compared to two analytical models.

Oakley [38] studied a CO_2 over air interface for shock strengths M=1.41, 2.90, 3.08 and an Ar over N_2 interface for M=1.38 and 2.80. In these experiments, an initial condition and one post shock image were obtained for each experiment. A time sequence of images was presented for each case as well as plots of amplitude versus time. The experimental study was compared to various analytical models as well as a numerical hydrodynamics code developed at the University of Wisconsin-Madison.

2.1.4 Nova Laser Experiments

Dimonte and Remington [12], Dimonte *et al.* [11] and Holmes *et al.* [18] have all utilized the Nova laser located at Lawrence Livermore National Laboratory to conduct high Mach number (M>10) Richtmyer-Meshkov experiments. In these experiments, shock waves were generated by focusing eight Nova laser beams (28 kJ, 3 ns each) into a cylindrical hohlraum to create an X-ray spectrum that heated a target that was located on a hole in the hohlraum wall. The size of the entire hohlraum was on the order of 1 mm, and the hole in which the target laid had a diameter of 740 μm. The heating due to the X-ray spectrum caused an expanding ablation plasma at the surface of the

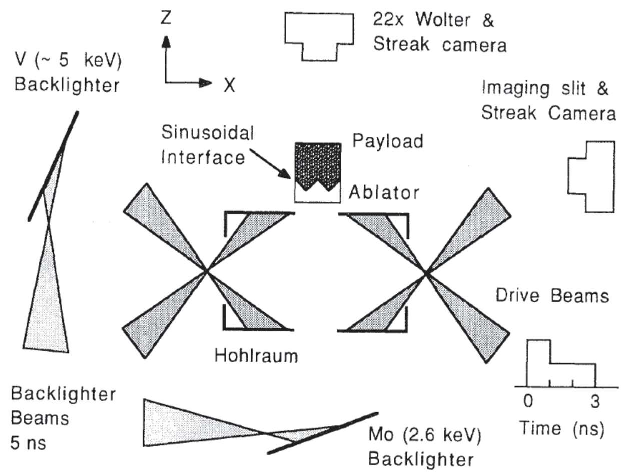

Figure 6: Schematic (not drawn to scale) of the experimental setup for the Nova laser experiments. Figure is taken from Dimonte and Remington [12].

target, and a shock wave that traveled into the target [18]. The target was constructed of a beryllium ablator and a low-density foam tamper that was made of either a CHO matrix doped with Na_2WO_4 or a brominated plastic CH(Br) [11]. A two dimensional sinusoidal perturbation was pre-imposed on the interface between the ablator and the tamper. Both the ablator and tamper became plasmas because of the X-ray preheat and subsequent shock wave [12]. It is important to note that the laser pulses had a predefined shape that created large shock wave strengths and maintained a Rayleigh-Taylor stable density interface [12]. These experiments were diagnosed with radiography in two configurations; a face-on and side-on view for the interface amplitude growth and a side-on view for the shock parameters [11]. Figure 6 is a schematic of the target used in the Nova laser experiments.

Dimonte and Remington [12] performed high compression experiments that were compared to the radiation and hydrodynamics simulation code called LASNEX. Their linear growth results agree with the Meyer-Blewett [34] formula (Eq. (1.12)) that the effective initial amplitude is the average of the pre and post shock initial amplitude. They also found that when the amplitude was large (on the order of $\eta \approx \lambda/3$) the fundamental mode of the interface saturates and harmonics develop that mark the transition to a slower growth rate regime [12]. Dimonte *et al.* [11] performed experiments at two drive strengths; one high temperature and one low temperature. These experiments were simulated with LASNEX as well as the CALE code. The CALE code was used to simulate the RM instability in two dimensions, whereas, the two codes were compared to each other in one dimension with quantified shock characteristics [11]. The results once again confirmed the Meyer-Blewett result. At large amplitude, the growth rate approached a decaying asymptotic limit. They also found that there was an upper limit to the magnitude of the growth rate because nonlinearities kept the interfacial spike from surpassing the transmitted shock wave [11].

Holmes *et al.* [18] performed the most comprehensive laser driven study of the RM instability. Mach 15.3 (incident shock strength) experiments were performed with initial perturbations of 4 and 10 μm at a constant wave number. Further experiments were carried out for the 4 μm interface at M=10.8. These experiments were compared to the nonlinear models of Zhang & Sohn [59] and Velikovich [57] as well as three hydrodynamics codes: RAGE, PROMETHEUS, and FronTier. The authors cited remarkable agreement between the experiments, models and simulations. Some deviations between the models and the experiments/simulations were noted. The Zhang & Sohn model underestimated the experimental and simulation growth rate when $k\eta_0^0 > 1$ because the model is matched to the linear theory which assumes $k\eta_0^0 \ll 1$, whereas, the Velikovich model described the early-time reduction well, but not the late-time decay because the model is not time dependent [18]. The authors postulated that strong shock effects could be studied at $M \geq 5$ [18].

The Nova laser has played host to other experimental campaigns that investigate ICF applications. Remington *et al.* [45], [46] used shaped laser pulses to perform large growth and multimode Rayleigh-Taylor experiments. Klein *et al.* [26] studied the shock sphere interaction of copper micropheres that were 100 μm in diameter at $M \sim 10$.

2.2 Analytical Model Review

Three analytical models have been chosen to compare with the experimental results of the current study. The Sadot *et al.* [51] model was chosen because it models Jacobs' [19] data well, and it assumes an initially single mode interface. The Mikaelian [36] model was chosen because it is an explicit, analytic expression for the evolution of the RM instability, and it utilizes separate equations for the linear and nonlinear regimes. The Dimonte and Schneider [13] model was chosen because it is in the form of a simple power law and it is designed for a wide range of initial conditions such as an initially multimode interface. The Zhang & Sohn model was not chosen because it does not follow the accepted $1/t$ late-time growth rate decay [10]. The Velikovich model was not chosen because it lacks time dependance, and therefore does not predict late-time growth rate decay well [18]. The primary goal of comparing experimental data to models, is to determine which models represent the experimental data well in both the linear ($\eta/\lambda \leq 0.1$) and nonlinear growth regimes ($\eta/\lambda \geq 0.1$).

2.2.1 Sadot *et al.*

Sadot *et al.* [51] presented an empirical formula that fits the linear, early nonlinear, and asymptotic behavior of the bubble and spike evolution associated with the RM instability. The model was an extension of the work done by Alon *et al.* [1], [2] that presented a bubble-competition picture that encompassed three components; single mode perturbations, two-bubble competition, and multimode fronts. Adjacent bubbles within an interface merge together at a rate that is a function of the bubbles' wavelength as well as time. Experimental and simulation data suggest that the merger rate does not depend on the Atwood number. The resulting wavelength of the new bubble is the sum of the two initial bubbles' wavelengths. The combined bubble fills the space that was previously occupied by the two adjacent bubbles. Large bubbles overtake smaller ones, which eventually leads to one bubble that encompasses the entire perturbation width [1]. This idea was used to create a model to predict RM instability growth as the combination of two power laws. Initially the amplitude growth rate is given as:

$$\dot{\eta}(t) = \dot{\eta}_0 \left(1 \pm \dot{\eta}_0 k A^1 t\right), \tag{2.1}$$

where $\dot{\eta}_0$ is the initial growth rate in the linear regime, given by Richtmyer's impulsive model Eq. (1.7). The variables k and A^1 are the wavenumber and post-shock Atwood number respectively, and the plus and minus signs are for the bubble and spike respectively. The asymptotic spike velocity is given as:

$$\dot{\eta}(t) = \left(\frac{1+A}{1-A}\right)\frac{C\lambda}{t}, \tag{2.2}$$

whereas, the asymptotic bubble velocity is:

$$\dot{\eta}(t) = \frac{C\lambda}{t}, \tag{2.3}$$

and C is given by:

$$C = \begin{cases} \frac{1}{3\pi}, & A^1 \geq 0.5 \\ \frac{1}{2\pi}, & A^1 \rightarrow 0 \end{cases}. \tag{2.4}$$

The Sadot *et al.* growth rate for an initially single mode interface is an empirical fit to Eq. (2.1), (2.2), and (2.3) and is given as:

$$\dot{\eta}(t) = \dot{\eta}_0 \frac{1 + Bt}{1 + Dt + Et^2}, \tag{2.5}$$

The constant parameters B, D, E are given by:

$$B = \dot{\eta}_0 k, \tag{2.6}$$

$$D = (1 \pm A)\dot{\eta}_0 k, \tag{2.7}$$

$$E = \frac{(1 \pm A)}{(1 + A)} \left(\frac{1}{2\pi C} \right) \dot{\eta}_0{}^2 k^2, \tag{2.8}$$

A limitation of this model is the choice of C since a continuous relationship between A and C does not exist. In addition, the model does not correctly model the spike growth for $A \gtrsim 0.9$ [51]. Integration of Eq. (2.5) results in an equation for the amplitude of the spike or bubble (depending on constants D and E) with respect to time:

$$\begin{aligned} \eta = {} & \left[\frac{\dot{\eta}_0}{(4E - D^2)^{1/2}} \left(2 - \frac{BD}{E} \right) \right] \times \\ & \tan^{-1} \left[\frac{2Et + D}{(4E - D^2)^{1/2}} \right] + \\ & \frac{\dot{\eta}_0 B}{2E} \ln \left(1 + Dt + Et^2 \right) + K, \end{aligned} \tag{2.9}$$

where K is the constant of integration found by matching the time zero amplitude with the compressed amplitude [40].

Since the Sadot *et al.* model is an empirical fit to the initial and asymptotic growth, one would expect the model to correctly represent the early linear growth and the late nonlinear growth. Based on how the model was formulated, there is no indication as to how well it will model the transition from the linear to nonlinear regime. However, the model has shown good agreement with previous experiments [19].

2.2.2 Mikaelian

In 2003, Mikaelian [36] presented an explicit, analytic expression for the evolution of the two dimensional RM instability in the linear and nonlinear regimes. Since it is analytical, Mikaelian's model draws the distinction of being one of the few models that does not require numerical methods to solve ordinary or partial differential equations. This model assumes incompressible fluids as well as potential flow and was built on Mikaelian's [35] previous work which was based off of the results of Layzer [27]. Layzer presented an analytic model for the Rayleigh-Taylor instability that described the vertex (the location on the interface with the greatest height) height and velocity for two dimensional flow between two parallel walls with respect to time.

In the linear regime of the Mikaelian model, the amplitude with respect to time is given as Richtmyer's impulsive model:

$$\eta(t) = \eta_0^1 \left(1 + V_0 k A^1 t\right), \tag{2.10}$$

where V_0 is the interface velocity, and η_0^1 is the post-shock amplitude. Whereas, in the nonlinear regime, the amplitude versus time is given as:

$$\eta(t) = \eta_0^1 + \frac{3 + A^1}{3(1 + A^1)k} \ln\left(1 + 3\dot{\eta}_0 kt \frac{(1 + A^1)}{(3 + A^1)}\right), \tag{2.11}$$

where $\dot{\eta}_0$ is the initial growth rate. The threshold for changing from Eq. (2.10) to Eq. (2.11) occurs when

$$\eta(t) = \frac{1}{3k}. \tag{2.12}$$

Mikaelian's analytic model showed good agreement with numerical simulations performed by the *CALE* hydrocode [36]. However, the model may have limited application in specific circumstances where the impulsive model does not approximate the linear growth regime well.

2.2.3 Dimonte & Schneider

Dimonte and Schneider [13] developed a power law model in 2000, to study the RM instability of a multimode interface. The model combines an equation for the penetration amplitude with an equation that balances the buoyancy and drag on a bubble. The penetration amplitude equation has problems when there is a finite initial amplitude or a decelerating interface. These problems are corrected with the buoyancy/drag model. The bubble penetration depth h (analogous to perturbation amplitude) for an impulsively accelerated interface is given as:

$$h(t) = h_0 \zeta^{\theta_{s,b}}, \tag{2.13}$$

where h_0 is the initial penetration depth, and

$$\zeta \equiv \left(\frac{dh}{dt}\right)_0 \left(\frac{t - t_0}{\theta h_0}\right) + 1. \tag{2.14}$$

The bubble growth exponent θ is determined by:

$$\theta_b = \frac{1}{(1+N)}, \tag{2.15}$$

where N is an experimentally determined constant. The value of θ_b is experimentally determined to be 0.25 ± 0.05 across all Atwood numbers [13]. The spike growth exponent is slightly modified and is given as:

$$\theta_s = \theta_b R^{D_\theta}, \tag{2.16}$$

where R is the density ratio of the heavy to light gas and D_θ is an empirically determined value.

The Dimonte and Schneider [13] model is a power law model, therefore (assuming that the growh exponent does not equal one), it may not model the growth well at early times if that growth is linear. One would expect this model to work the best for initial conditions that are either nonlinear or nearly nonlinear at time zero.

Chapter 3

Experimental Program

The current experimental campaign is carried out in the Wisconsin Shock Tube Laboratory (WiSTL). This facility is used for various experimental programs that are applicable to fusion energy and astrophysics research. Previous results have been obtained for the Richtmyer-Meshkov instability [38], [40]; shock diffraction on cylinders [3]; shock-water layer interaction [32]; and shock-bubble interaction [41], [42].

3.1 The Shock Tube Structure

The WiSTL facility consists of a vertically oriented, downward firing shock tube that is located in the Mechanical Engineering Building on the University of Wisconsin-Madison campus. The shock tube is approximately 9 m tall and has a modular construction, which allows for the rearranging of the shock tube for different experimental configurations. It has a large internal cross-section which allows for the minimization of interface-boundary layer interactions. The shock tube was designed to have a strong structural capacity [3] that allows for studying strong shocks into gases at atmospheric pressure. As shown in Fig. 7, the shock tube consists of five main sections: driver, diaphragm, driven, interface, and test.

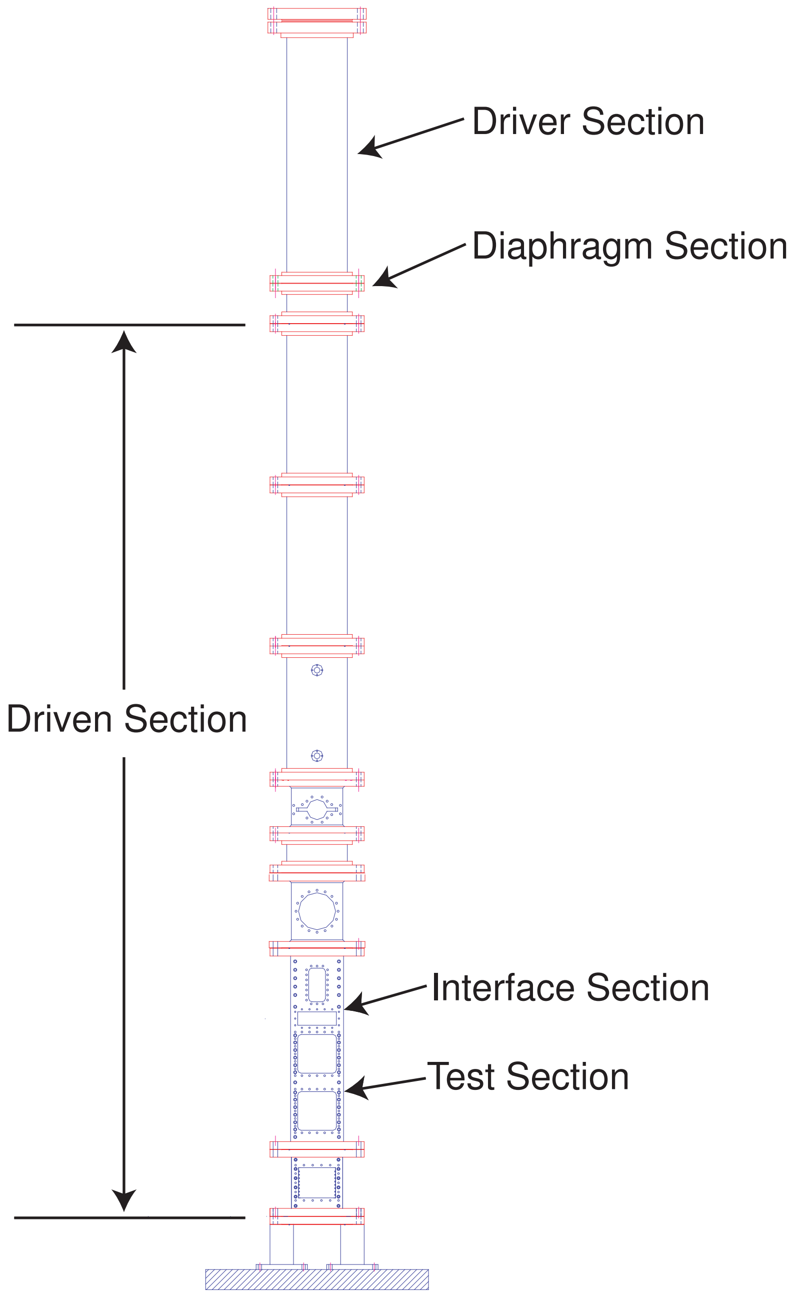

Figure 7: A schematic of the WiSTL shock tube.

3.1.1 Driver Section

The driver section consists of a circular, chrome-plated carbon steel pipe that is 2.08 m long. The driver is the top section of the shock tube, which allows for the downward firing of the shock wave. The inner diameter of the section is 0.472 m, and the wall thickness is 0.019 m. The driver is outfitted with a valve that allows for the supply of a driver gas, the venting of gas to outside the facility building, and the vacuuming of gas with a roughing pump to ensure gas purity. A pressure gauge is located on the driver section to monitor the pre-rupture pressure. Two boost tanks are connected via fast acting pneumatic valves to the driver section. The high-pressure (15 MPa) boost tanks allow for a more controlled initiation of the shock wave by rapidly raising the pressure of the driver section at the moment the experiment is ready to take place. Figure 8 is a photograph of the driver section and the two boost tanks.

3.1.2 Diaphragm Section

The first section below the driver is the diaphragm section of the shock tube. This section is 0.35 m long and has an inner diameter of 0.42 m. A flat, round metal diaphragm is placed in between the driver and diaphragm sections, and a shock wave is created when the driver is pressurized to a pressure that ruptures the diaphragm. Sharp knife edges that form a cross are located directly below the metal diaphragm. The knife edges allow the diaphragm to rupture in the form of four petals that stay attached to the outer circumference of the diaphragm during and after the experiment. Figure 9 is a photograph of the knife edge. The importance of this method of rupture is two-fold: to ensure the rupture pressure is consistent from one experiment to the next; and to

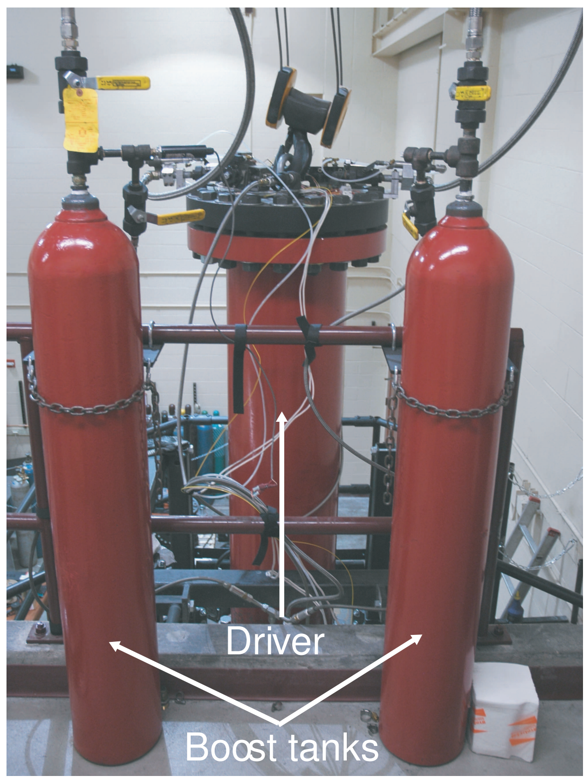

Figure 8: Photograph of the driver section.

minimize the risk of diaphragm fragments breaking off that could result in damage to the test section windows. Figure 10 depicts the a metal diaphragm before and after rupture.

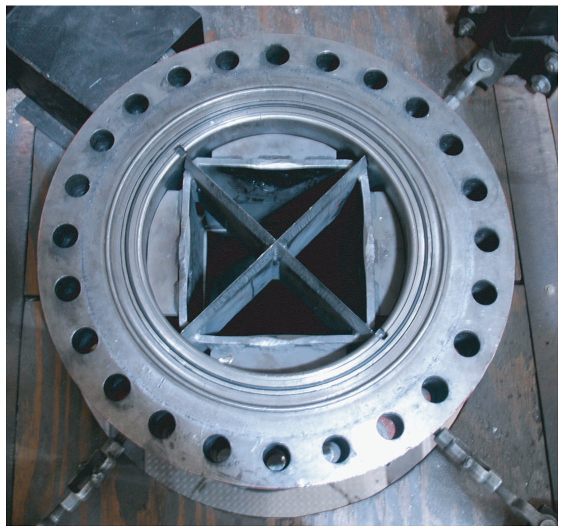

Figure 9: Photograph of knife edge in diaphragm section.

3.1.3 Driven Section

The driven section consists of all the various modular shock tube sections that are located below the diaphragm section. The test and interface sections are considered part of the driven section, and are discussed separately. The cross-section of the driven section consists of an internal liner, made of four stainless steel plates (9.5 mm thick) that are welded together to form a square (25.4 cm sides) cross section, that is contained within a circular carbon steel pipe (46 cm outer diameter, 42 cm inner diameter). The space between the liner and pipe is filled with concrete to provide structural support to the steel liner. The total length of the driven section is 6.41 m. The cross-section of the

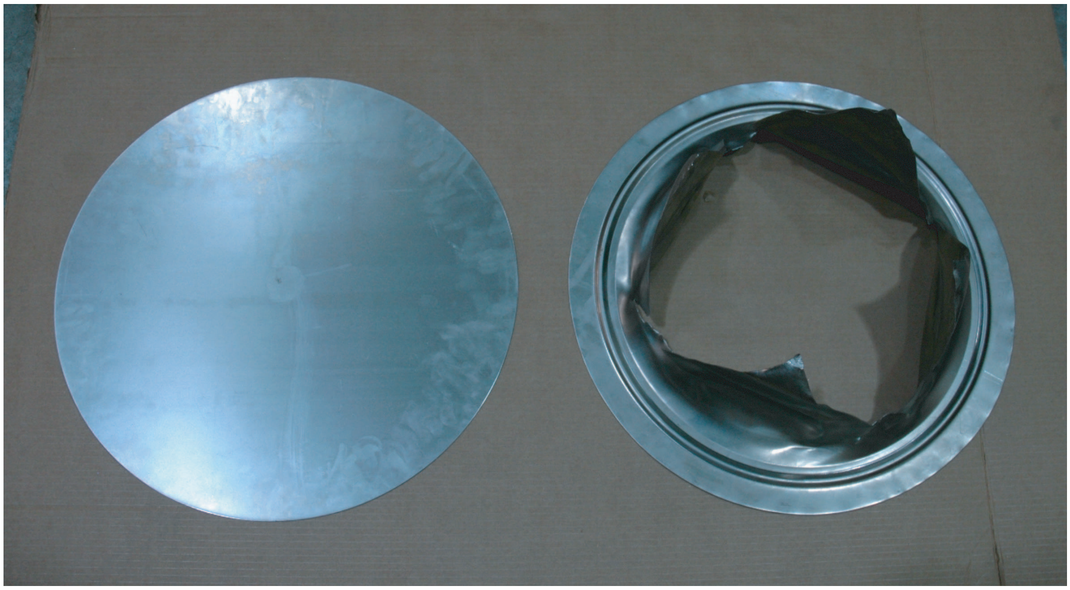

Figure 10: Photograph of a diaphragm prior to (left) and after (right) rupture.

driven section is depicted in Fig. 11.

3.1.4 Interface/Test Section

The interface section (where the interface between the driven and test gas is created) and the test section (where the post shock images are acquired) are located on the same modular piece of the shock tube. This section was designed specifically for the RM instability experiment and consists of four steel plates (each 7.3 cm thick) that are welded together to form a 25.4 cm (inner dimension) square cross-sectional box. Two rectangular slots at the top of the section contain the pistons that create the sinusoidal interface (discussed in detail in the next section). Four window ports are included on the section faces that are perpendicular to the piston slots in order to facilitate experimental imaging. One port is aligned with the piston slots in order to image the initial condition,

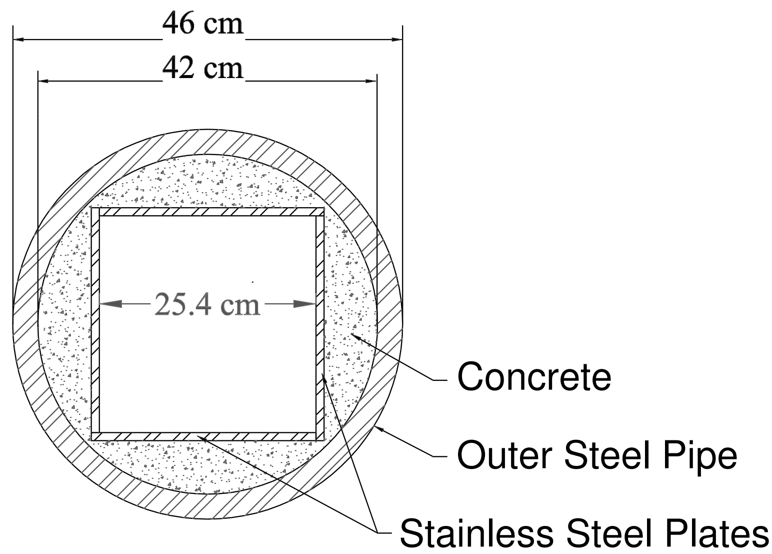

Figure 11: A cross-section of the driven section.

and the other three ports are consecutively placed on opposite sides of the section with a small overlap. Square windows with a square cross-section of 22.86 cm and circular windows with a diameter of 24 cm are interchangeable within the four window ports. Multiple ports are located on the same walls as the pistons and are available for laser access into the shock tube. Figures 12 and 13 are front and side view photographs of the interface and test sections. The overall length of the combined sections is 1.52 m.

3.2 Interface Creation

For these experiments, the Richtmyer-Meshkov instability is studied for three gas pairs. A 50% helium + 50% argon mixture over argon interface (A=0.29) is studied for initial

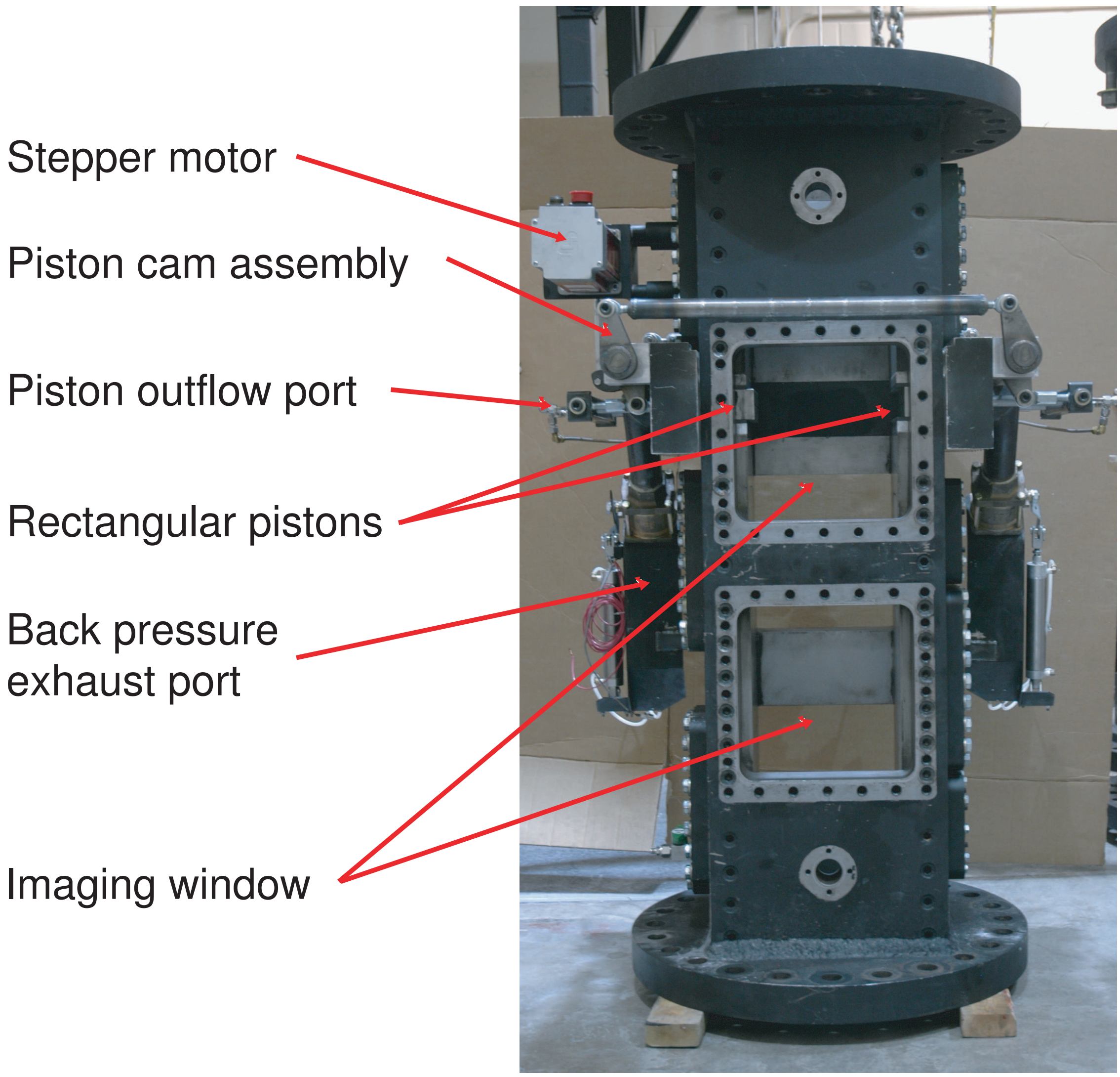

Figure 12: Photograph of the interface/test section: front view.

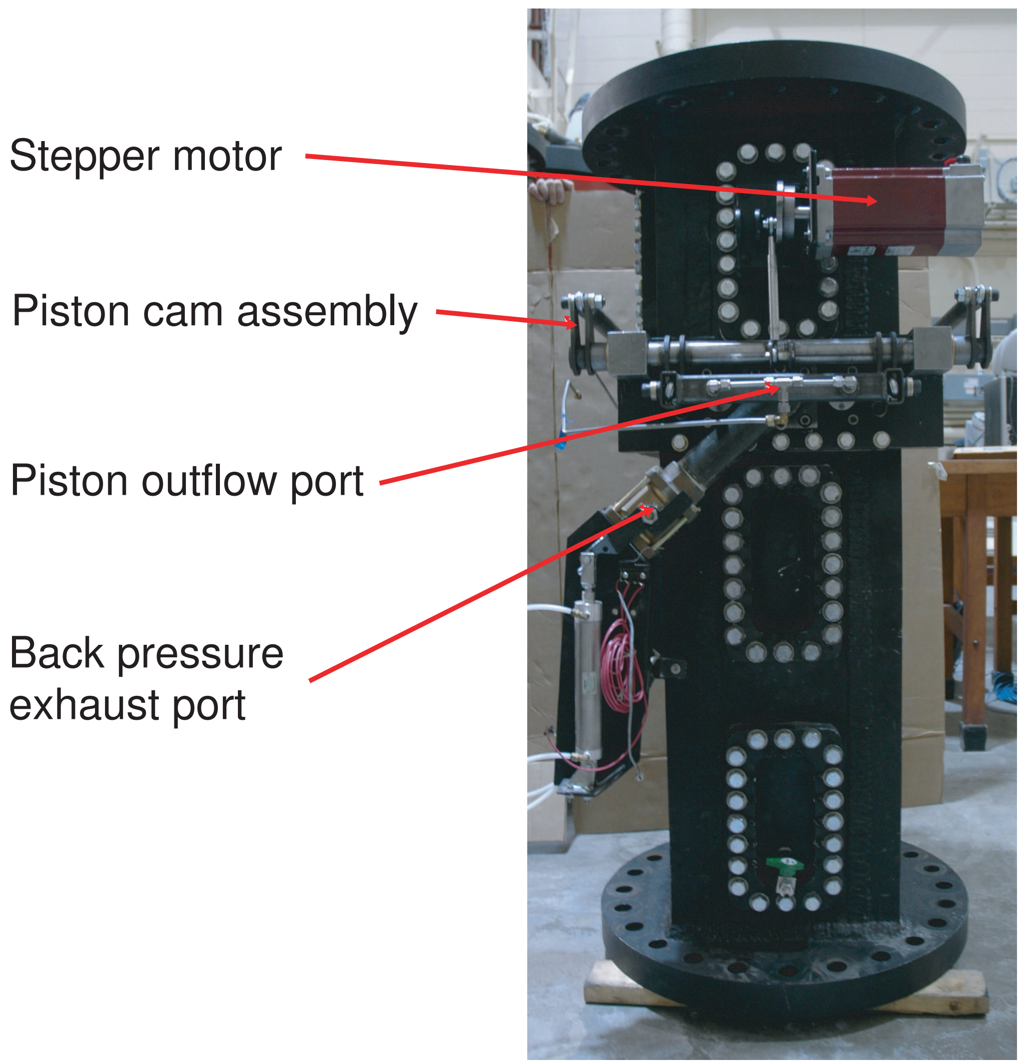

Figure 13: Photograph of the interface/test section: side view.

shock wave strengths of M=1.30 and M=1.90. A nitrogen over sulfur hexafluoride interface (A=0.68) is studied for shock wave strengths of M=1.26, M=2.05, and M=2.86. Lastly, a helium over sulfur hexafluoride interface (A=0.95) is studied for shock wave strengths of M=1.13, M=1.41, and M=1.95. The interface preparation method designed and used for this experiment is similar to the one used by Jones and Jacobs [24]. The interface section of the shock tube, shown in Fig. 12, was designed to accommodate two rectangular 5.08×25 cm aluminum pistons that span the horizontal dimension of the shock tube. The pistons have a 0.3175 cm slot that is connected to a vacuum pump that is set to an out-flow rate that maintains atmospheric pressure within the shock tube. The heavy gas is introduced into the bottom of the shock tube, and the light gas is introduced into the shock tube just below the diaphragm at the top of the driven section. The gas flow rates are controlled using variable area rotameters. The gases meet at the piston outflow slot location and create a flat, two-dimensional stagnation surface. The inlet flow rates were determined experimentally, and correspond to a stable, flat interface that aligns with the middle of the piston outflow slots. Table 1 indicates the inlet flow rate of the light and heavy gas for each gas pair described above. The difference in flow rates between the light and the heavy gas accounts for the difference in shock tube volumes above and below the interface.

Gas pair	Light gas (m^3/ s)	Heavy gas (m^3/ s)
50% He + 50% Ar / Ar	7.5×10^{-4}	4.5×10^{-4}
N_2 / SF_6	4.7×10^{-4}	1.7×10^{-4}
He / SF_6	8.5×10^{-4}	1.7×10^{-4}

Table 1: Inlet gas flow rates for each gas pair.

One of the two test gases is seeded with either acetone, cigarette smoke, or atomized hydrocarbon vacuum pump oil depending on the desired method of imaging. Acetone seeding is performed by running nitrogen through two consecutive acetone baths, originally filled to 800 ml each, that are kept at a constant temperature. On average, the mole fraction of acetone for a nitrogen/acetone mixture is 0.12. The gases are flowed continuously for 30 minutes at which point a flat interface and sufficient gas purity on either side of it are achieved. For the cigarette smoke and atomized oil cases, the test gas that is to be seeded flows into the shock tube for 30 minutes. The seeding material (either smoke or oil) is then inserted into the flow through a port on the side of the shock tube. Ample time is allowed to let the test gas draw the smoke or oil to the interface in a uniform manner (which takes 30 seconds to 5 minutes depending on the injection site and gas flow rate) For the case of cigarette smoke particle seeding, a smoke injector (see Fig. 14) is used to first draw smoke from a cigarette and then inject the smoke into the shock tube via a port that is either located approximately 2 m above the interface (for the case of light gas seeding) or approximately 0.75 m below the interface (for heavy gas seeding). Hydrocarbon vacuum oil seeding is performed by filling the liquid reservoir of a TSI Six-Jet Atomizer (Model 9306A) with Kurt J. Lesker Company TKO 19 Ultra hydrocarbon based (White Mineral Oil) vacuum pump oil. The same gas as the test gas (from a different gas bottle source) is then flowed through the atomizer at a maximum inlet pressure of 379.0 kPa (55 PSI). The inlet gas then flows through six atomizer jets that entrain the oil and impact it on a spherical impactor to break up the oil particles. The flow then flows through a ball valve connected to the shock tube approximately 0.75 m below the interface. Figure 15 is a photograph of the oil atomizer.

The gas interface is then given a two-dimensional perturbation by oscillating the aluminum pistons with a high-torque Pacific Scientific hybrid stepper motor (model #

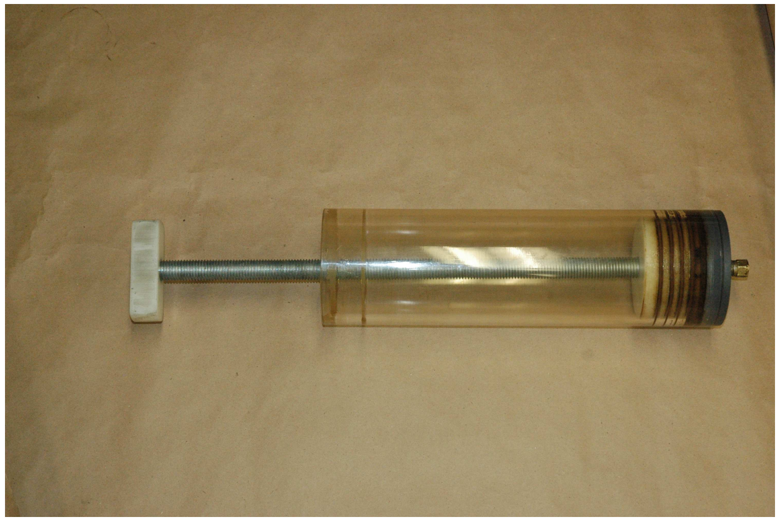

Figure 14: Photograph of cigarette smoke injector.

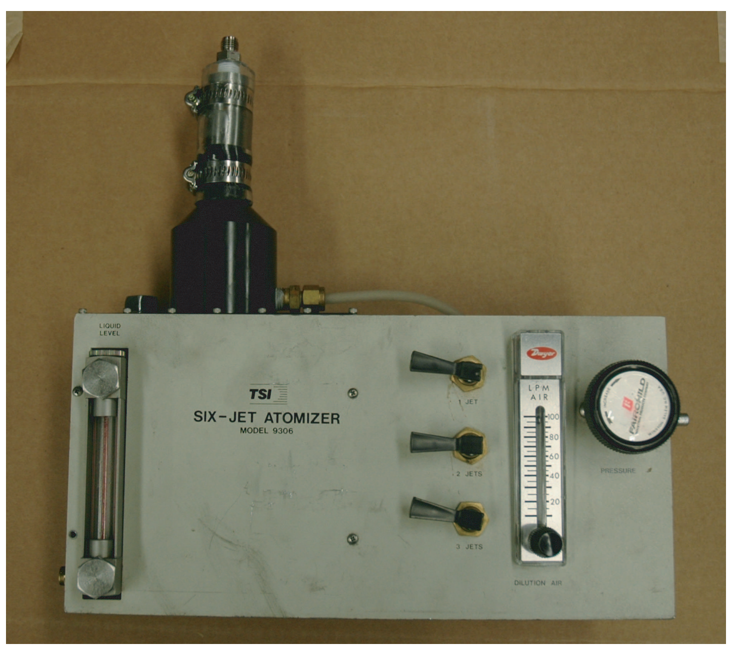

Figure 15: Photograph of hydrocarbon oil atomizer.

K43HCHL-LEK-M2-01). The stepper motor is driven by a Pacific Scientific microstepping drive module (model # 6410-001). The drive module is controlled by a National Instruments LabVIEW PCI-7342 digital acquisition card that interacts with a user created LabVIEW program, and is powered by a 52.8 V, variable current power supply. The total linear travel of the pistons for each oscillation is 2.86 cm. Table 2 indicates the stepper motor parameters used to create a standing (or quasi-standing) wave for each gas pair. The stepper motor parameters are only valid for the inlet flow rates indicated in Table 1.

Gas pair	Frequency (Hz)	Revolutions	Acceleration (rev/ s^2)
50% He + 50% Ar / Ar	1.25	14	3000
N_2 / SF_6	2.10	3	3000
He / SF_6	2.55	3	5000

Table 2: Stepper motor parameters for each gas pair.

Determination of the driving frequency is made by an exhaustive trial and error process. Experiments are performed by rotating the pistons via the stepper motor at frequencies between 0.2 Hz and 3.5 Hz at 0.1 Hz increments. For each frequency, multiple numbers of revolutions are tested. For cases where the driving frequency was less than approximately 1.0 Hz, the pistons tend to push the gas to the top and bottom of the pistons, instead of pushing the gas horizontally to create a wave. When driven at high frequencies (approximately 3.0 Hz and above), the pistons move through the gas at such a high speed that the gas does not seem to react to the piston movement. Both low and high frequency cases correspond to the creation of a non-repeatable small amplitude interface that appears to be three-dimensional.

Lighthill [28] derives an expression for finding the oscillating frequency, σ, of a standing wave for a non-diffuse interface between two fluids of different density. The frequency is given as:

$$\sigma = \frac{\sqrt{gkA}}{2\pi}, \tag{3.1}$$

where g is the acceleration of gravity, k is the wave number, and A is the Atwood number. Equation (3.1) is valid if the depth of fluid on either side of the interface is at least 0.28 λ (*i.e.* the fluid is deep on both sides of the interface). For a N_2/SF_6 interface having A=0.678, the wavenumber is 0.375 cm^{-1} and the depth of fluid on both sides of the interface is much greater than 0.28 λ. The resulting frequency from Eq. (3.1) is 2.51 Hz, whereas the driving frequency of the experiment is 2.10 Hz. Therefore, Eq. (3.1) does not appear to be valid for the fluids and parameters that are being investigated in this experimental campaign. Specifically, the current experiments have a finite diffusion thickness which Eq. (3.1) does not take into account.

3.3 Diagnostics

The experiments are diagnosed using cameras that image either the scattered light from smoke or oil particles or the fluorescence of acetone from a laser sheet perpendicular to the gas interface.

3.3.1 Laser Sources

For the experiments where the N_2 is seeded with acetone, the flow is visualized by planar laser-induced fluorescence (PLIF). Fluorescence occurs if the laser light incident on the gas is resonant with an optical transition of the gas. A fraction of the incident photons are absorbed within the flow field and a fraction of the absorbed photons are then re-emitted with a different spectral distribution [52]. The acetone vapor fluoresces in the visible spectrum when ultraviolet (UV) light in the 225-320 nm range is incident upon it [30]. To perform PLIF, three Lambda Physik excimer lasers (two LPX200 models and one COMPex201) are utilized. The lasing is produced by excimers (short-lived molecule made up of two species with one or more of the species in an excited state [5]) in the excited state that give off a photon when they decay to their ground state. The three Lambda Physik lasers operate on Krypton Fluoride (KrF) fill gas, emitting light with a 248 nm wavelength. The laser energy per pulse is between 300 - 600 mJ, with a pulse width of 25 - 30 ns. Appropriate optics are used to steer the laser beams into the shock tube and create a uniform laser sheet. Figure 16 is a photograph of one of the excimer lasers, and Fig. 17 is a schematic of a typical optic setup for experiments utilizing an excimer laser.

Figure 16: Photograph of an excimer laser.

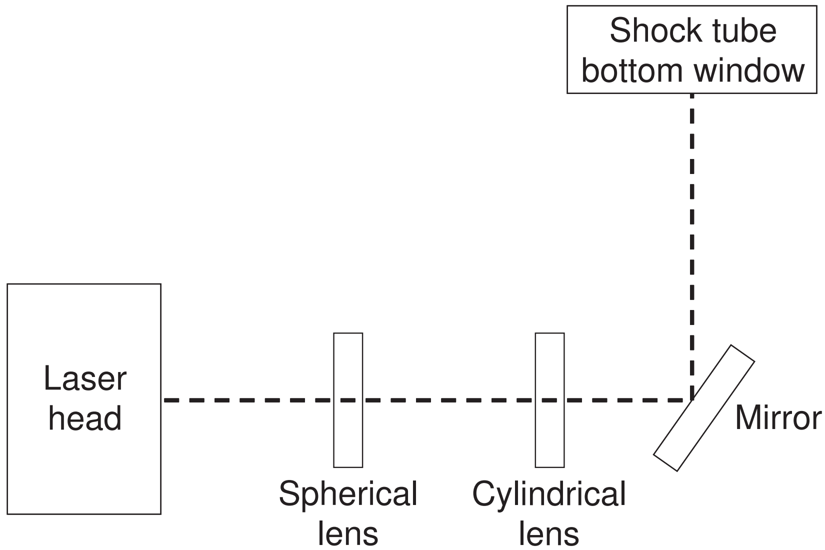

Figure 17: Schematic of typical optic setup for the excimer laser.

The cigarette-smoke-seeded flow is visualized by Mie scattering. Mie scattering involves the scattering of light from particles much larger than the light wavelength embedded within the flow, such as smoke or fog. A Continuum Surelite II Nd:YAG laser having two heads is used as the light source. The laser cavities have an output wavelength of 1064 nm and then go through an external frequency doubler crystal, which gives a final wavelength of 532 nm. The laser energy per pulse of the Nd:YAG laser is 200-250 mJ at 532 nm, with a pulse width of approximately 10 ns. Appropriate optics are used to steer the individual laser beams into the shock tube and create a uniform laser sheet. Figure 18 is a photograph of the Nd:YAG laser, and Fig. 19 is a schematic of a typical optic setup for experiments utilizing the Nd:YAG laser. The purpose of the photodiode is to provide a feedback signal that indicates that the laser is firing at the appropriate time.

Two different imaging techniques were utilized because of limitations of the PLIF imaging. Ideally, PLIF would be a better visualization method because it may be used (if properly calibrated) to determine the concentration of the seeded fluid [30]. All of the seeding materials used in the current experimental study experience pyrolysis at temperatures approaching 1000 K. In addition, acetone (with an incident laser wavelength of 248 nm) experiences a significant decrease in fluorescence as the temperature increases from 300 - 1000 K [56], thus making it an inappropriate choice for moderate and high incident shock strengths.

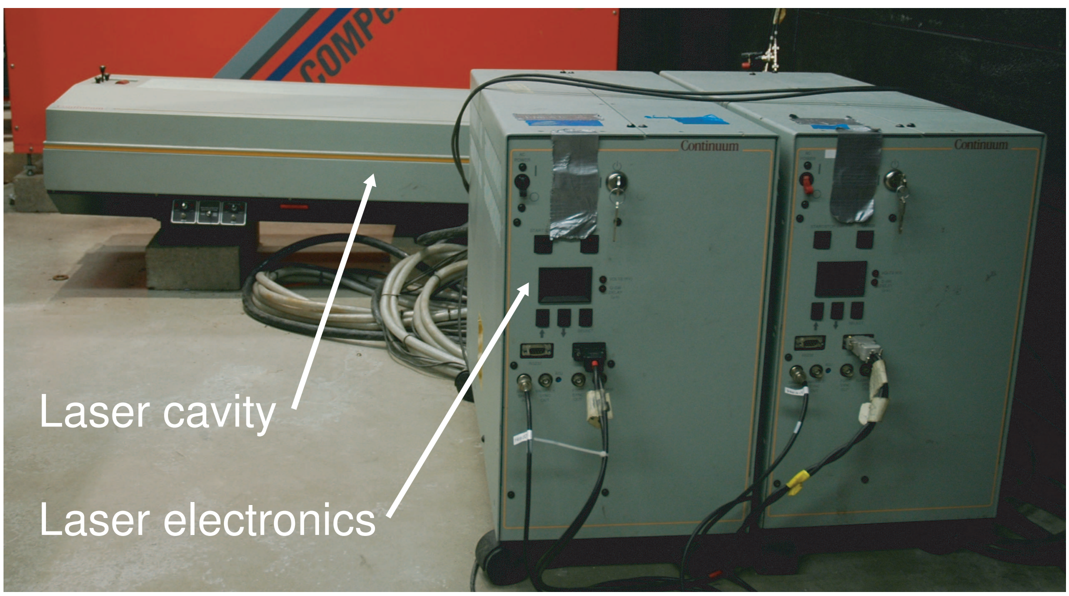

Figure 18: Photograph of the Nd:YAG laser showing both power supplies, one for each laser cavity.

3.3.2 Cameras

The initial condition image and subsequent post-shock images are each captured by an ANDOR Charge Coupled Device (CCD) camera system, model # DV434-BU2, with a 1 MHz CCI-010 system PCI controller. The CCD array and its pre-amplifier are

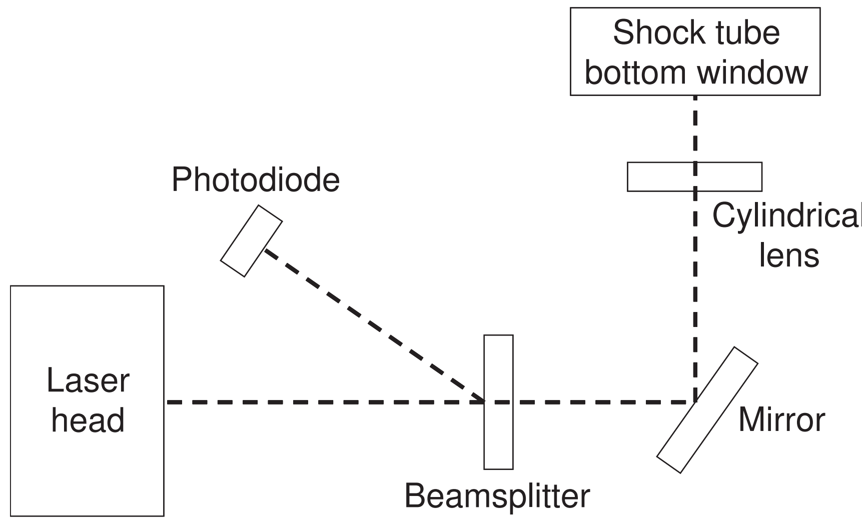

Figure 19: Schematic of typical optic setup for the Nd:YAG laser.

housed in a detector head along with a thermoelectric cooler and temperature sensor. The CCD is operated at a temperature of -60°C (for minimization of the dark current noise) that is achieved with thermoelectric cooling. The detector head is connected to an ANDOR controller card that is installed in a desktop computer equipped with the Windows operating system. Images are obtained with 16-bit resolution on a 1024×1024 pixel array. The shutter time, which is the time the mechanical shutter takes to open, for the ANDOR camera is 20 ms and therefore must be opened prior to triggering a shock wave. The exposure time is set to 5 seconds which allows for inconsistencies in the diaphragm rupture time. The maximum readout time of 32 μs per pixel was chosen to achieve the lowest read-out amplifier noise. Mounted on the camera are a Nikon 50 mm focal length, f/1.2 aperture camera lens and a light filter that either accepts or rejects a specific bandwidth of light depending on the laser and imaging method that is used in the experiment. Figure 20 is a photograph of the camera, lens, and light filter used in the present experimental study.

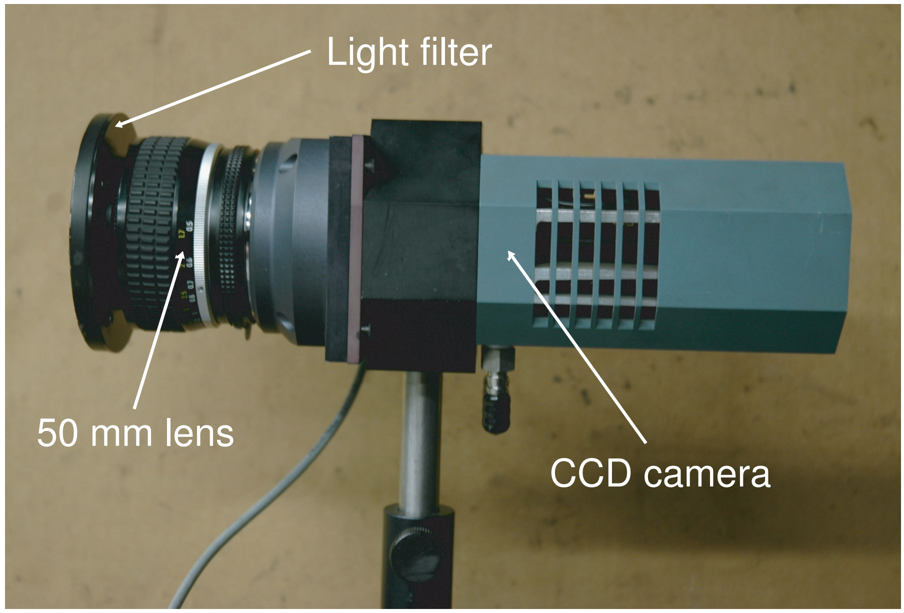

Figure 20: Photograph of ANDOR camera assembly.

3.4 Experimental Procedure

The experiment begins with placing a metal diaphragm between the driver and diaphragm sections of the shock tube. The test and interface gases are then flowed to create a flat interface as previously discussed. While the interface is being prepared, the two boost tanks are filled to a high pressure with the driver gas. Once the flat interface is achieved, the lasers are exercised to ensure that the optics are aligned correctly and that the lasers are firing at the correct energy. The driver is filled with gas to a pressure that is approximately 10% less than the diaphragm rupture pressure. The ANDOR cameras are placed on standby just prior to the start of the piston motion. The pistons are controlled by a National Instruments LabVIEW program through a PCI-7342 digital acquisition (DAQ) computer board. During the piston motion, electronic triggers from the PCI-7342 board are sent out to open the camera shutters, close the vacuum pump valve, and open the valve between the boost tank and the driver. A second computer runs a LabVIEW program that utilizes four PCI-6110E DAQ boards to process data from nine piezoelectric pressure transducers (PT) located along the side of the entire shock tube, including one PT located at the end wall. A PT located 0.66 m above the interface is used to detect the pressure jump from the shock wave, and then serves as the trigger to fire the lasers at predetermined delay times based on shock strength and interface speed. An initial condition image is collected within microseconds prior to shock acceleration, as well as one or two post shock images. After the experiment, the initial and post-shock images are saved, the PT data is used to determine the speed of the shock wave, and the high pressure in the shock tube is vented.

3.5 Numerical Simulation

Hydrodynamic computations are performed by another graduate student within the shock tube research group (Chris Weber) using a 2-D hydrodynamics code (*Raptor*) that solves the multi-fluid compressible Euler equations, with an ideal gas law equation of state. A shock-capturing scheme and higher-order Godunov solver is used to handle shock propagation accurately and suppress spurious oscillations [9]. The calculations utilize a fixed (Eulerian) grid in 2-D Cartesian geometry, 512 grid points in the transverse dimension, and two levels of adaptive mesh refinement (AMR) on the fluid interface. The computational initial condition is a single mode sinusoidal wave with the same initial amplitude and wavelength parameters as the experimental initial condition. The interface is then made diffuse by vertically applying a hyperbolic tangent fitted to the diffusion characteristics of the experimental interface. The relative concentrations of nitrogen and acetone vapor (for the acetone seeded case), and the strength of the incident shock wave, correspond to the experimentally determined values. The simulation results are compared to the experimentally measured growth rates.

Chapter 4

Visualization Results

Visualization results are obtained for eight experimental scenarios. These scenarios span a wide range of Atwood numbers, $0.29 < A < 0.95$, and shock strengths, $1.1 < M < 3$. The initial condition for each gas pair is characterized to determine the degree to which the perturbation is two-dimensional, single mode, and diffuse.

4.1 Experimental Overview

The Richtmyer-Meshkov instability is experimentally investigated for eight scenarios that form a parameter study of Atwood and Mach number space. Three gas pairs make up the current experimental campaign: (50% He + 50% Ar)/Ar, N_2/SF_6, and He/SF_6. Table 3 provides an overview of the parameter study. The initial and transmitted Mach number and pre-shock Atwood number is given for each gas pair along with the seeding material used to visualize the experiment. The seeded gas is given in parenthesis.

In order to achieve the wide range of Mach numbers listed in Table 3, various diaphragm and boost tank combinations are utilized. Table 4 indicates the diaphragm material, thickness, and rupture pressure for each scenario as well as the boost tank gas and pressure. Helium is used in the boost tanks to achieve high Mach numbers since it has a low density and therefore high sound speed.

For each of the scenarios in Table 3, between 10 and 25 experiments are analyzed.

Scenario No.	Light Gas	Heavy Gas	M	M_t	A	Tracer (Gas)
1	50% He + 50% Ar	Ar	1.30	1.35	0.29	Oil (Ar)
2	50% He + 50% Ar	Ar	1.90	2.07	0.29	Smoke (Ar)
3	N_2	SF_6	1.26	1.39	0.64	Acetone (N_2)
4	N_2	SF_6	2.05	2.65	0.68	Smoke (N_2)
5	N_2	SF_6	2.86	4.03	0.68	Oil (SF_6)
6	He	SF_6	1.13	1.27	0.95	Smoke (SF_6)
7	He	SF_6	1.41	1.88	0.95	Smoke (SF_6)
8	He	SF_6	1.95	3.08	0.95	Smoke (SF_6)

Table 3: Overview of the experimental study, including light and heavy gases as well as Mach number of the incident shock wave (M), transmitted shock wave (M_t), pre-shock Atwood number (A), and fluid tracer.

Scenario No.	Diaphragm Material	Diaphragm Thickness	Rupture (PSI)	Boost Gas	Boost (PSI)
1	Aluminum	0.064 cm	29	N_2	1000
2	Steel	0.152 cm	337	He	1500
3	Aluminum	0.041 cm	19	N_2	400
4	Steel	0.152 cm	384	N_2	2000
5	Steel	0.152 cm	337	He	1500
6	Aluminum	0.064 cm	30	CO_2	500
7	Steel	0.121 cm	309	N_2	1500
8	Steel	0.152 cm	338	He	1500

Table 4: Diaphragm rupture parameters for each scenario described in Table 3.

Pressure transducer data is used to determine the initial Mach number (M). The pre-shock initial amplitude (η_0^0) and wavelength (λ) are measured from experimental images. The post-shock initial amplitude (η_0^1) is calculated with Eq. (1.8). Table 5 gives the average quantity of each of these parameters along with the standard deviation for each of the length measurements because they vary by experiment due to slight inconsistencies in the diaphragm rupture. The standard deviation is defined as:

$$S = \left(\frac{1}{m-1} \sum_{j=1}^{m} (y_j - \bar{y})^2 \right)^{\frac{1}{2}}, \tag{4.1}$$

where m is the total number of objects within a set, and $\bar{y}$ is the average of the set given as:

$$\bar{y} = \frac{1}{m} \sum_{j=1}^{m} x_j, \tag{4.2}$$

The last column in Table 5 indicates the initial amplitude to wavelength ratio. An interface with $\eta_0^0/\lambda<0.1$ is expected to have an initial growth stage in the linear regime, whereas, $\eta_0^0/\lambda>0.1$ is understood to be in the nonlinear regime. Table 5 indicates that the experiments conducted for the (50% He + 50% Ar)/Ar gas pair definitely begin in the linear regime. The He/SF_6 have a η_0^0/λ ratio that is close to the nonlinear threshold of 0.1. These experiments are almost completely conducted in the nonlinear regime.

4.2 Amplitude and Wavelength Measurement

Utilizing a repeatable algorithm, the amplitude and wavelength of each experiment is measured by a direct visual inspection of the image within the framework of the imaging software. The peak-to-peak amplitude is measured by first determining the columns that contain the maximum and minimum perturbation amplitude. Next, the interface

Scenario No.	M	A^1	η_0^0 (cm)	η_0^1 (cm)	λ (cm)	k (cm^{-1})	η_0^0/λ
1	1.30	0.29	0.29±0.04	0.21±0.03	20.15±0.42	0.31±0.01	0.01
2	1.90	0.27	0.26±0.02	0.14±0.01	19.72±0.58	0.32±0.01	0.01
3	1.26	0.67	0.70±0.11	0.55±0.08	14.56±4.04	0.47±0.15	0.05
4	2.05	0.77	0.85±0.11	0.50±0.06	16.76±0.55	0.38±0.01	0.05
5	2.86	0.80	1.04±0.09	0.53±0.04	17.36±0.27	0.36±0.01	0.06
6	1.13	0.95	1.50±0.13	1.42±0.12	16.94±0.49	0.37±0.01	0.09
7	1.41	0.96	1.38±0.11	1.21±0.10	16.74±0.66	0.38±0.02	0.08
8	1.95	0.97	1.36±0.12	1.12±0.10	16.70±0.52	0.38±0.01	0.08

Table 5: Parameters of the experimental study (for each scenario described in Table 3) including the Mach number of the incident shock wave (M), the post-shock Atwood number (A^1), the pre-shock initial amplitude (η_0^0), the post-shock initial amplitude (η_0^1) from Eq. 1.8, the wavelength (λ), the wave number (k), and the initial amplitude to wavelength ratio.

location (in pixels) is determined by finding the 50% concentration level (based on pixel intensity) with respect to the concentration directly above and below the interface. The difference of the pixel location for the maximum and minimum amplitudes is multiplied by the pixel dimension (length/pixel) to obtain the peak-to-peak amplitude (η_{pp}). The reported amplitude, η, is then $\eta_{pp}/2$.

The wavelength is determined for each initial condition image utilizing the peak amplitude locations. The midpoint between the maximum and minimum amplitude locations is used to create a horizontal line that approximately intersects the points along the interface at which the curvature changes. One wavelength is then measured at the distance (pixels multiplied by the pixel dimension) between two consecutive rising (or falling) slopes that intersect the horizontal midpoint line. The 50% concentration criteria is utilized for determining the location of the intersection between the interface and the horizontal midpoint line.

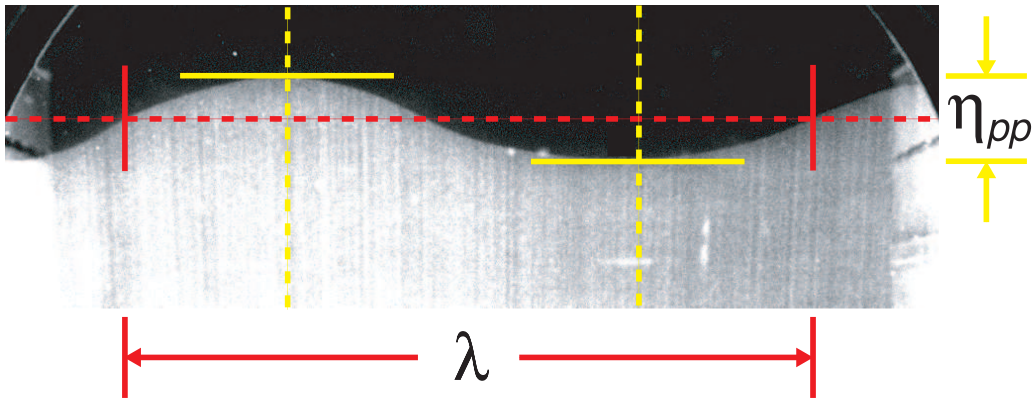

Figure 21: Schematic of how the amplitude and wavelength of a perturbation is determined.

Figure 21 is a schematic of how the amplitude and wavelength are measured after the 50% concentration locations are determined. The yellow, dashed vertical lines indicate the maximum and minimum amplitude columns. The red, dashed horizontal line is the wave midplane. The peak-to-peak amplitude is then given as the distance between the solid yellow lines and the wavelength is the distance between the solid red lines.

4.3 Image Correction

For the case of planar laser-induced fluorescence visualization, image post-processing is performed. A region of interest is extracted from the raw initial condition image, including either the entire width of the shock tube, or a single wavelength of the wave. This image is first corrected for the laser sheet divergence with a conformal mapping algorithm that places each light ray into a column, and corrects for the laser attenuation (due to the acetone) by integrating Beer's Law along the ray. This procedure is repeated for each ray. The Beer-Lambert law is outlined by Collins and Jacobs [10], and given in a differential form as:

$$dI = -\epsilon C_0 \xi I ds, \tag{4.3}$$

where I is the intensity of the light ray, ϵ is given as the extinction coefficient, C_0 is the tracer intensity at a location with maximum intensity, ξ=C/C_0 is the normalized intensity, and s is the location along a light ray. For each pixel in an image, the intensity value i is;

$$i = mC_0 \xi I, \tag{4.4}$$

where m is a collection efficiency constant. Equations (4.3) and (4.4) are combined and then integrated along individual light rays;

$$I - I_0 = -\frac{\epsilon}{m} \int i ds. \tag{4.5}$$

Then, combining Eq. (4.4) and (4.5) gives the tracer intensity as a function of measurable quantities;

$$\xi = \frac{i}{i_0 - \epsilon C_0 \int i ds}. \tag{4.6}$$

The image is then remapped to physical space, and a five pixel Gaussian blur is applied to each pixel, to reduce the levels of fine-scale noise in the image due to artifacts of the imaging technique such as a non-uniform laser sheet or dirt on the window. The "mean" interface point along each column is determined by the location of the 50% intensity point. A Fourier transform of the "mean" interface points is then evaluated to study its spectral content for use in the numerical simulations. An example of the corrective progression is given in Fig. 22.

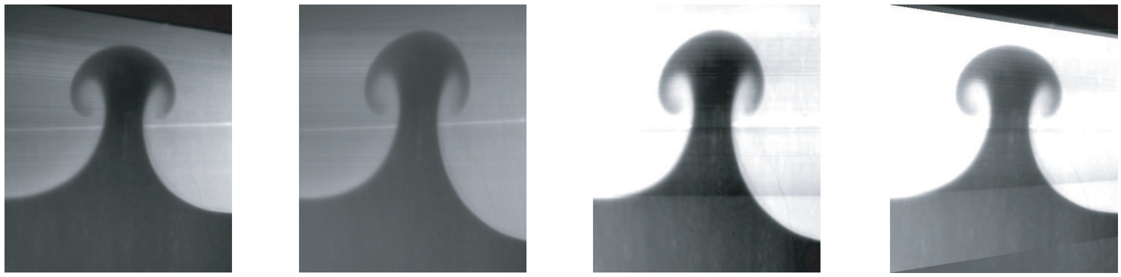

(a) (b) (c) (d)

Figure 22: The image correction process. (a) The initial image. (b) Mapped image. (c) Beer's law integrated along each ray of mapped image. (d) Final image remapped into original coordinate system.

4.4 Initial Condition Characterization

The initial condition is characterized by three parameters. The first method involves a three dimensional reconstruction of the initial condition. The second type of characterization is a modal content analysis. In addition to these two characterizations, the diffusion thickness for each gas pair is measured and estimated in a process that utilizes experimental parameters.

4.4.1 3-D Reconstruction

A three dimensional reconstruction is performed on the initial condition used for each gas pair in order to determine if the interface is two dimensional within the region of interest (the central portion of the shock tube). It is assumed that the interface will not be completely two dimensional due to viscous effects near the wall. Initially, a glass plate is installed on the bottom of the shock tube to allow the planar laser sheet to be scanned across the shock tube in one direction from the center plain. For this analysis, it is assumed that the perturbation is symmetric about the center plane (x=12.70 cm) of the shock tube. Five images are taken at each laser sheet location and then averaged. The averaged initial conditions are then compiled using a *MATLAB* script designed to create a 3-D reconstructive mesh. The 3-D reconstruction is then shown with a planar sheet imposed at the center of the shock tube where imaging would occur during an experiment. In order to image close to the shock tube wall, the laser sheet needs to be tilted at a slight angle. The maximum laser sheet angle is 3.0^o, which results in a measurement error of the interface position of less than 1%.

Figure 23 is a 3-D reconstruction of the (50% He + 50% Ar)/Ar interface. The reconstruction is based on nine plane locations within half of the shock tube. The nine locations chosen are: x=12.70 cm (center), x=11.43 cm, x=10.16 cm, x=8.89 cm, x=7.62 cm x=6.35 cm, x=5.08 cm, x=3.81 cm, and x=2.54 cm. The perturbation amplitude and shape appear two dimensional within the middle two-thirds of the shock tube. The amplitude reduces to a nearly flat profile at the wall.

Figure 24 is a 3-D reconstruction of the N_2/SF_6 interface. The reconstruction was based on five plain locations within half on the shock tube. The five locations chosen are: x=12.70 cm (center), x=10.36 cm, x=8.01 cm, x=5.69 cm, and x=2.54 cm. The perturbation amplitude and shape appear two dimensional within the middle half of the shock tube, and the amplitude stays fairly large throughout the entire shock tube.

Figure 25 is a 3-D reconstruction of the He/SF_6 interface. The reconstruction was based on the same nine plain location used for the (50% He + 50% Ar)/Ar gas pair. The perturbation amplitude and shape appear two dimensional within almost the entire shock tube.

Figures 23, 24, and 25 indicate that the interface creation method described in Section 3.2 is appropriate for producing a two dimensional interface within the central

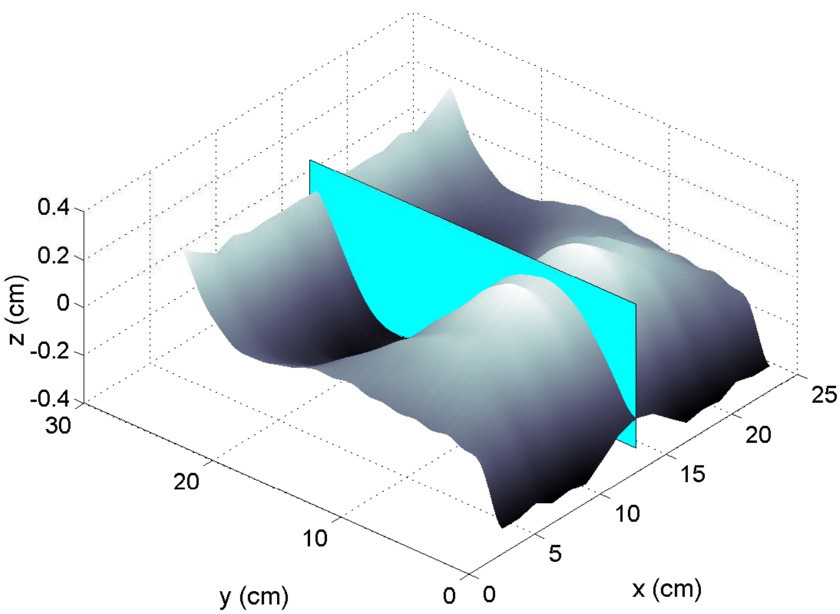

Figure 23: A 3-D reconstruction of the (50% He + 50% Ar)/Ar initial condition. The blue rectangle represents the plane imaged during a RM experiment.

portion of the shock tube. All of the reconstructions show that, to a certain degree, the interface amplitude decreases as it approaches the stationary walls. This effect appears more pronounced in Figures 23 and 24 because the z axis scale is not set equal to the x and y axis. The high Atwood number (He/SF_6) case appears to produce the most uniform interface throughout the shock tube in terms of amplitude and perturbation shape.

4.4.2 Modal Analysis

The modal content of the initial condition for each gas pair is determined in order to obtain a mathematical expression for the interface geometry. The goal of this analysis is to demonstrate the degree to which the initial perturbation is a single mode sinusoidal

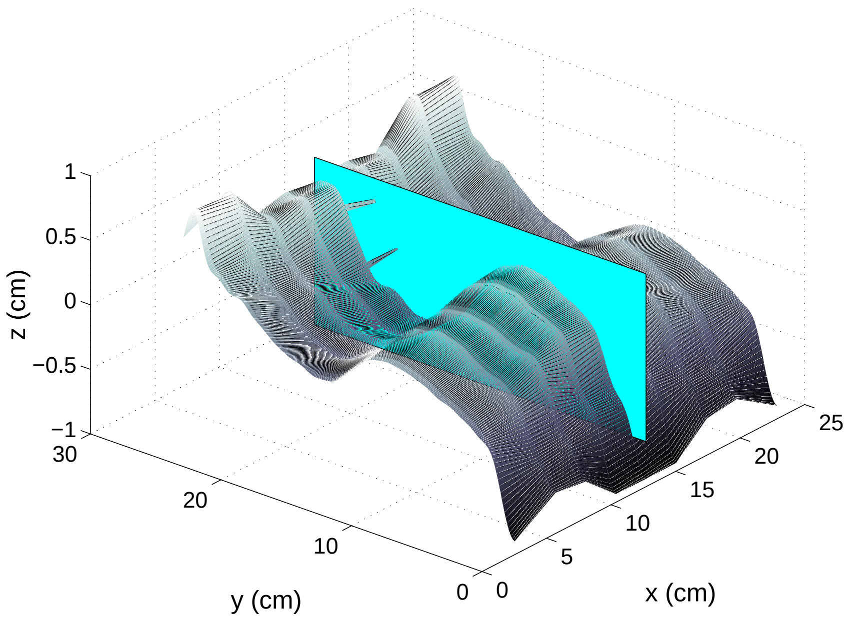

Figure 24: A 3-D reconstruction of the N_2/SF_6 initial condition.

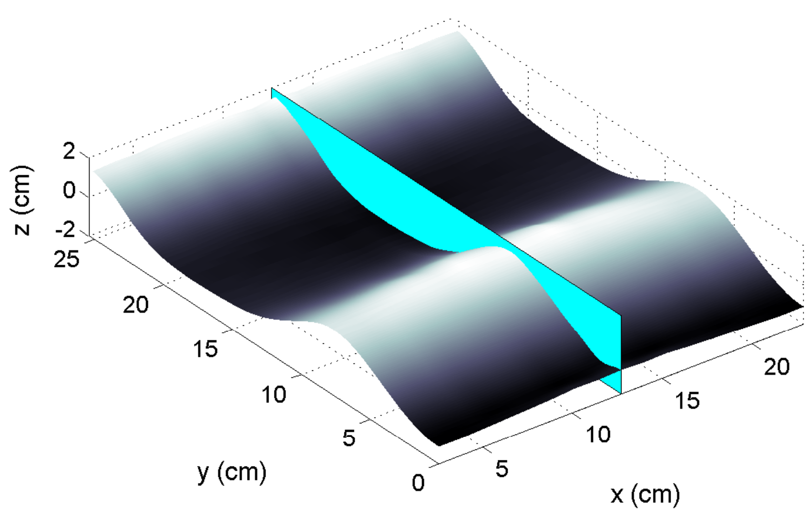

Figure 25: A 3-D reconstruction of the He/SF_6 initial condition.

wave. The analysis is performed on a representative set of experimental initial condition images. Within a *MATLAB* script, the shape of each initial condition is determined using an edge detection method that steps along each pixel column until a predetermined pixel intensity threshold is crossed. Next, a fast Fourier transform (FFT) of each initial condition is performed. The normalized amplitude (with respect to the maximum amplitude) of each mode is then averaged over all realizations. For a given experiment, the modal amplitude can be obtained by multiplying the normalized modal amplitude by the maximum amplitude as determined by the process described in Section 4.2. The average amplitude for each mode is plotted versus mode number, with error bars indicating the standard deviation of the amplitude data. For each of the gas pairs, the interface length is approximately 1.5 wavelengths. The FFT requires an integer number of wavelengths, therefore, the interface is mirrored on one edge. This results in three wavelengths, which corresponds to a single, dominant third mode.

Figure 26 is a plot of the modal content for the initial condition used in the (50% He + 50% Ar)/Ar experiments. The average represents 32 total experiments performed at M=1.30 and 1.90. The FFT is performed on the entire interface perturbation (*i.e.* the width of the shock tube), and not a single wavelength. The total length of the interface is between 1 and 1.5 wavelengths, therefore, a large first mode is present and the second mode has a large standard deviation. However, based on the rest of the model content, it can be concluded that the initial condition is predominantly single moded. The spectral information is almost entirely contained within the first seven modes, after which the largest non-dimensional amplitude of any mode is 2.1% of the predominant mode.

Figure 27 is a plot of the modal content for the initial condition used in the N_2/SF_6 experiments. The average represents 6 experiments performed at M=2.05. The initial

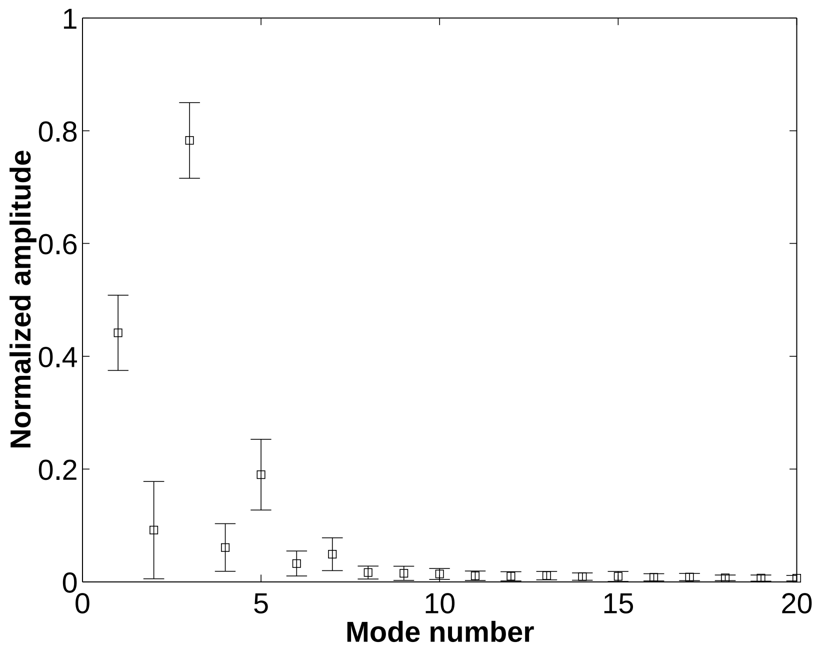

Figure 26: Modal content of the (50% He + 50% Ar)/Ar initial condition interface.

condition is predominantly single moded, with that mode having a non-dimensional amplitude that is approximately five times greater than the next largest mode. The spectral information is almost entirely contained within the first seven modes, after which the largest non-dimensional amplitude of any mode is 2.3% that of the predominant one.

Figure 28 is a plot of the modal content for the initial condition used in the He/SF_6 experiments. The average represents 65 total experiments preformed at M=1.13, 1.41, and 1.90. The modal content is very similar to the N_2/SF_6 modal content. There is one predominant mode. The second largest non-dimensional mode amplitude is 22% of the predominant mode. The spectral information is almost entirely contained within the first six modes, after which the largest non-dimensional amplitude of any mode is 3.8% of the predominant mode.

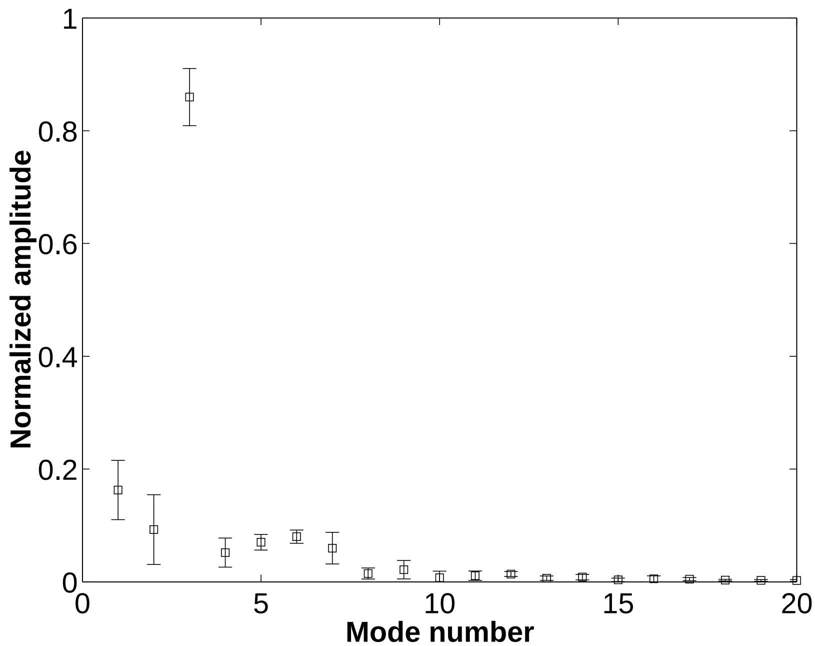

Figure 27: Modal content of the N_2/SF_6 initial condition interface.

4.4.3 Diffusion Thickness

The initial condition consists of a membraneless, continuous interface. Therefore, it is necessary to quantify the length of the initial molecular mixing region (diffusion thickness). The diffusion thickness is one of several inputs into the computer code *Raptor*, which is used to simulate the experiments. This length can either be measured directly from the initial condition image, or it can be calculated using parameters from the setup of the initial condition. Both analysis methods are performed and then compared.

In order to determine the experimental diffusion thickness, the pixel intensity for several columns of an initial condition image are averaged to minimize small scale variations. The average intensity is then corrected for attenuation, and fit with a hyperbolic tangent function. Two thresholds are used to evaluate the diffusion thickness. The first

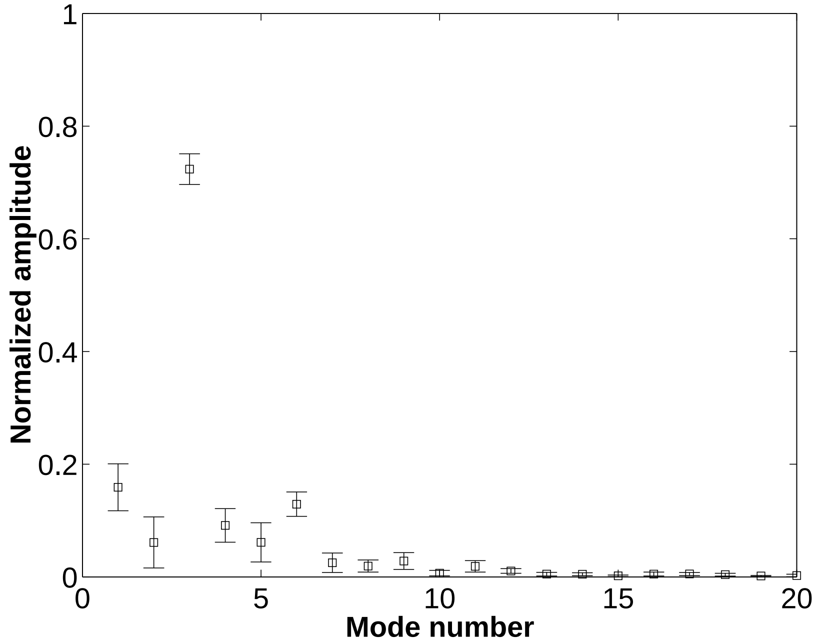

Figure 28: Modal content of the He/SF_6 initial condition interface.

is the length from 10% to 90% of the maximum concentration of seeded gas, and the second is the distance from 1% to 99%. The process is performed for both the spike and bubble. The left side of Figure 29 indicates the columns of an initial condition image used to create an average intensity. The right side is a plot of the normalized intensity in the vicinity of the interface, fit by a hyperbolic tangent function given as:

$$y = a \tanh(bx) + c, \tag{4.7}$$

where y is the pixel intensity, x is the location along the interface and a, b, and c are parameters used to fit the experimental data.

The second method is to calculate a maximum diffusion thickness based on the known parameters of the experiment. The diffusion thickness is given as [7]:

$$\delta = 2 \left(\pi D_{ab} \tau_D\right)^{\frac{1}{2}}, \tag{4.8}$$

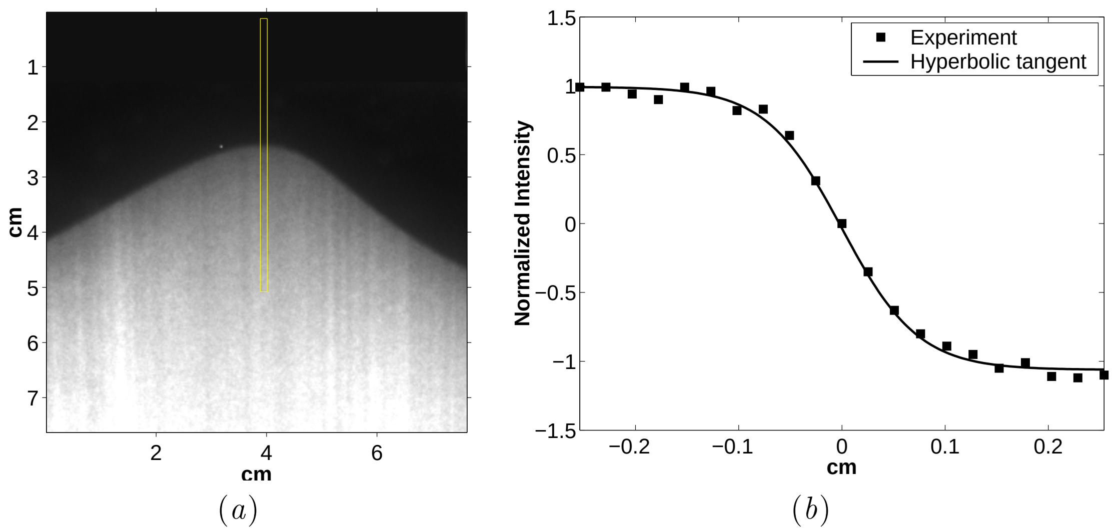

Figure 29: Hyperbolic tangent fit of an experimental interface. Box within image (a) indicates a region where the diffusion thickness is measured, and plot (b) is a zoomed-in lineout of the interface that is fit with a hyperbolic tangent.

where D_{ab} is the diffusion coefficient of a specific gas pair, and τ_D is the characteristic diffusion time. This time is indirectly obtained from the experimental parameters and is given as:

$$\tau_D = \tau_A + \tau_B, \tag{4.9}$$

where τ_A is the time a particle travels along the stagnation surface from the center of the shock tube to the edge, and τ_B is the amount of time that elapses between when the piston outflow is turned off and when the shock wave accelerates the interface. The value of τ_B is set constant at 50 ms for each gas pair. The value of τ_A is different for each gas pair and is primarily a function of inlet volumetric gas flow rates. Figure 30 is a schematic of the fluid flow along the stagnation surface.

The variable τ_A is given as:

$$\tau_A = \frac{\Delta x}{V_D}, \tag{4.10}$$

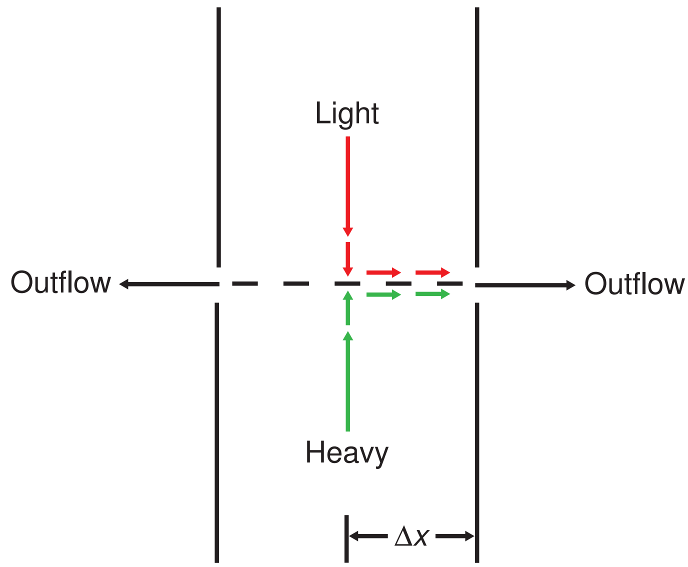

Figure 30: Schematic of the stagnation surface.

where Δx is the distance between the center and edge of the shock tube, and V_D is the outlet flow velocity which is the volumetric flow rate divided by the piston outflow cross-sectional area.

The diffusion coefficient (D_{ab}) is calculated by the procedure outlined in Reid *et al.* [44]. The value is calculated by the following equation:

$$D_{ab} = \frac{0.00266T^{\frac{3}{2}}}{PM_{ab}^{\frac{1}{2}}\sigma_{ab}^{2}\Omega_D}, \tag{4.11}$$

where T is temperature (300 K), P is pressure (98,274 Pa), σ_{ab} is the characteristic Lennard-Jones length, and Ω_D is the dimensionless diffusion collision integral which is related to temperature. The calculated diffusion coefficient for each gas pair is listed in Table 6.

The results of the diffusion analysis are summarized in Table 7. For each gas pair, the diffusion thickness for a spike and bubble of a typical initial condition is determined for

Gas Pair	σ_{ab} Å	Ω_D	Diffusion Coefficient (cm^2/s)
50% He + 50% Ar/Ar	3.05	0.75	0.72
N_2/SF_6	4.46	1.02	0.10
He/SF_6	3.84	0.81	0.41

Table 6: Diffusion coefficient for each gas pair determined using Eq. (4.11).

both a 10-90% and 1-99% maximum concentration threshold. The calculated diffusion thickness value is obtained from Eq. (4.8).

Gas Pair	Spike (cm)		Bubble (cm)		Calculated
	10-90%	1-99%	10-90%	1-99%	(cm)
50% He + 50% Ar / Ar	0.19	0.34	0.17	0.30	1.42
N_2 / SF_6	0.14	0.24	0.18	0.32	0.69
He / SF_6	0.22	0.39	0.17	0.31	1.13

Table 7: Measured and calculated diffusion thickness for each gas pair.

Table 7 indicates that for each gas pair the measured diffusion thickness for both the spike and bubble is approximately 0.2 cm for the 10-90% threshold, and 0.3 cm for the 1-99% threshold. The values do not appear to be a function of gas pair. The calculated diffusion thickness, however, indicates that the diffusion thickness is dependent on the interface gas pair and flow rates. The measured diffusion thickness is primarily the seeding particle diffusion thickness, which is not necessarily the molecular diffusion thickness of the interface gases. Equation (4.8) provides a more accurate estimate of the molecular diffusion thickness, and therefore these values are referred to as the diffusion thickness and used as an input into *Raptor*.

4.5 Experimental Visualizations

Visualization results are presented for the eight experimental scenarios listed in Table 3. For each scenario, a wave diagram indicates whether the shocked gas interfaced will be influenced by any reflected shocks or the rarefaction wave while the interface is within the experimental viewing windows. A table is presented for each scenario which indicates the experimental parameters used for data analysis. Lastly, a time sequence of images is presented for each scenario.

4.5.1 (50% He + 50% Ar)/Ar, M=1.30

A (50% He + 50% Ar)/Ar interface (A=0.29) is investigated at M=1.30. The heavy gas (Ar) is seeded with atomized hydrocarbon oil. A wave diagram ($x - t$ plot) of this scenario is given in Fig. 31. The red line originating at x=0 m is the contact surface between the driver and driven gases, and the red line originating at approximately x=5.2 m is the interface location. The first pair of dotted blue lines ($x \approx 5.1$ - 5.4 m) represents the initial condition window and the second pair of dotted blue lines ($x \approx 5.8$ - 6.1 m) represent the last experimental viewing window. Since the test section windows overlap each other, the first ($x \approx 5.1$ m) and last ($x \approx 6.1$ m) blue line outline the entire extent of the viewing area. The collection of black lines starting at x=0 m moving in the $-x$ direction as time increases represent the expansion fan (rarefaction) while the single black line starting at x=0 m moving in the $+x$ direction represents the initial shock wave. The goal for each set of experiments is to be able to image the shocked gas interface within the viewing area before the reflected shock (from the bottom of the shock tube) or reflected expansion fan interact with the interface. Subsequent wave diagrams for each additional gas pair/Mach number combination are set up the same way. Figure 31 indicates the rarefaction does not interact with the shocked interface within the viewing area, however, the reflected shock traverses the interface near the bottom of the last window at approximately t=15 ms (point A).

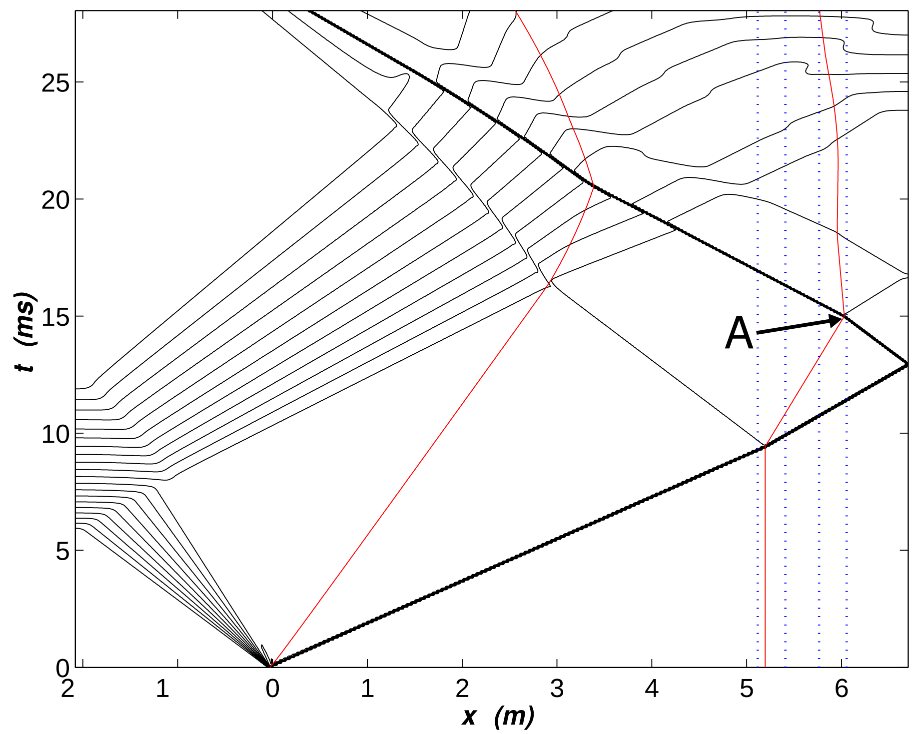

Figure 31: Wave diagram ($x-t$ plot) for the (50% He + 50% Ar)/Ar, M=1.30 scenario.

Table 8 lists the experimental parameters for each experiment conducted in this campaign. Growth rate data is obtained for 16 experiments. For each experiment, one post-shock image is obtained, and the time and amplitude of the post-shock perturbation are given as t_{PS1} and η_{PS1}, respectively. The post-shock time is relative to t=0 ms, which occurs when the incident shock wave traverses the bottom edge of the perturbation. Table 8 indicates that all of these experiments have a relatively small initial amplitude and long wavelength which, coupled with the small Atwood number, provides a reason why the post-shock amplitude remains small even at post-shock times of 5.2 ms.

Exp. No.	M	A^1	η_0^0 (cm)	η_0^1 (cm)	λ (cm)	k (cm^{-1})	t_{PS1} (ms)	η_{PS1} (cm)
435	1.31	0.29	0.18	0.13	20.07	0.31	0.706	0.24
436	1.32	0.29	0.28	0.20	19.43	0.32	0.875	0.39
437	1.27	0.29	0.28	0.21	20.22	0.31	0.428	0.25
438	1.29	0.29	0.25	0.19	19.96	0.31	0.619	0.30
439	1.30	0.29	0.25	0.19	19.56	0.32	0.224	0.20
440	1.31	0.29	0.30	0.22	20.55	0.31	1.744	0.62
442	1.31	0.29	0.29	0.21	20.63	0.30	1.169	0.52
443	1.28	0.29	0.27	0.20	20.37	0.31	1.432	0.52
444	1.29	0.29	0.29	0.22	20.45	0.31	2.058	0.75
445	1.32	0.29	0.34	0.25	20.55	0.31	2.341	0.94
446	1.29	0.29	0.24	0.18	20.07	0.31	2.815	0.74
451	1.31	0.29	0.33	0.24	20.50	0.31	3.504	1.22
454	1.32	0.29	0.34	0.25	20.14	0.31	3.109	1.18
455	1.32	0.29	0.32	0.24	19.28	0.33	4.232	1.45
456	1.30	0.29	0.34	0.25	20.63	0.30	4.737	1.46
457	1.30	0.29	0.30	0.23	20.09	0.31	5.237	1.56

Table 8: Experimental parameters for the (50% He + 50% Ar)/Ar, M=1.30 RM experimental campaign.

Figure 32 is a time sequence of experimental images from five of the experiments listed in Table 8. Each image is approximately 25 cm by 25 cm and is from an individual experiment. The images have not been post-processed because attenuation due to the atomized hydrocarbon oil is minimal. The first image is the initial condition image which is considered to be at time zero just prior to being accelerated. The actual image is obtained approximately 50 - 150 μs before the shock wave traverses the interface. This is acceptable because the initial condition oscillation is on the order of 300 - 500 ms. Figure 32 (a - e) confirms that, within the available viewing window, the perturbation remains in the linear regime, until later times (f) when the perturbation growth appears to become asymmetric.

4.5.2 (50% He + 50% Ar)/Ar, M=1.90

A second set of experiments are conducted on the (50% He + 50% Ar)/Ar interface (A=0.29). These experiments are conducted at M=1.90. For this case, the heavy gas (Ar) is seeded with cigarette smoke (Mie scattering). Smoke is utilized because it was experimentally determined that the atomized hydrocarbon oil will not survive the temperatures (650 K) realized in this set of experiments due to pyrolysis. A wave diagram of this scenario is given in Fig. 33. The $x-t$ plot indicates, that within the viewing area, the post-shock perturbation will not be influenced by either the expansion fan or any reflected shock waves.

Table 9 lists the experimental parameters for each experiment conducted in this campaign. Growth rate data is obtained for 16 experiments. As before in the M=1.30 case, one post-shock image is obtained for each experiment.

Figure 34 is a time sequence of experimental images from five of the experiments listed in Table 9. Each image is approximately 25 cm by 25 cm and has not been post-processed. The growth is similar to the growth seen in Fig. 32, however the growth occurs on a shorter time scale. In this case the overall amplitude growth appears to be linear while there also appear to be small perturbations developing along the interface (indicated by arrows in figure), which is shown by the jaggedness of the interface in Fig. 34 (f).

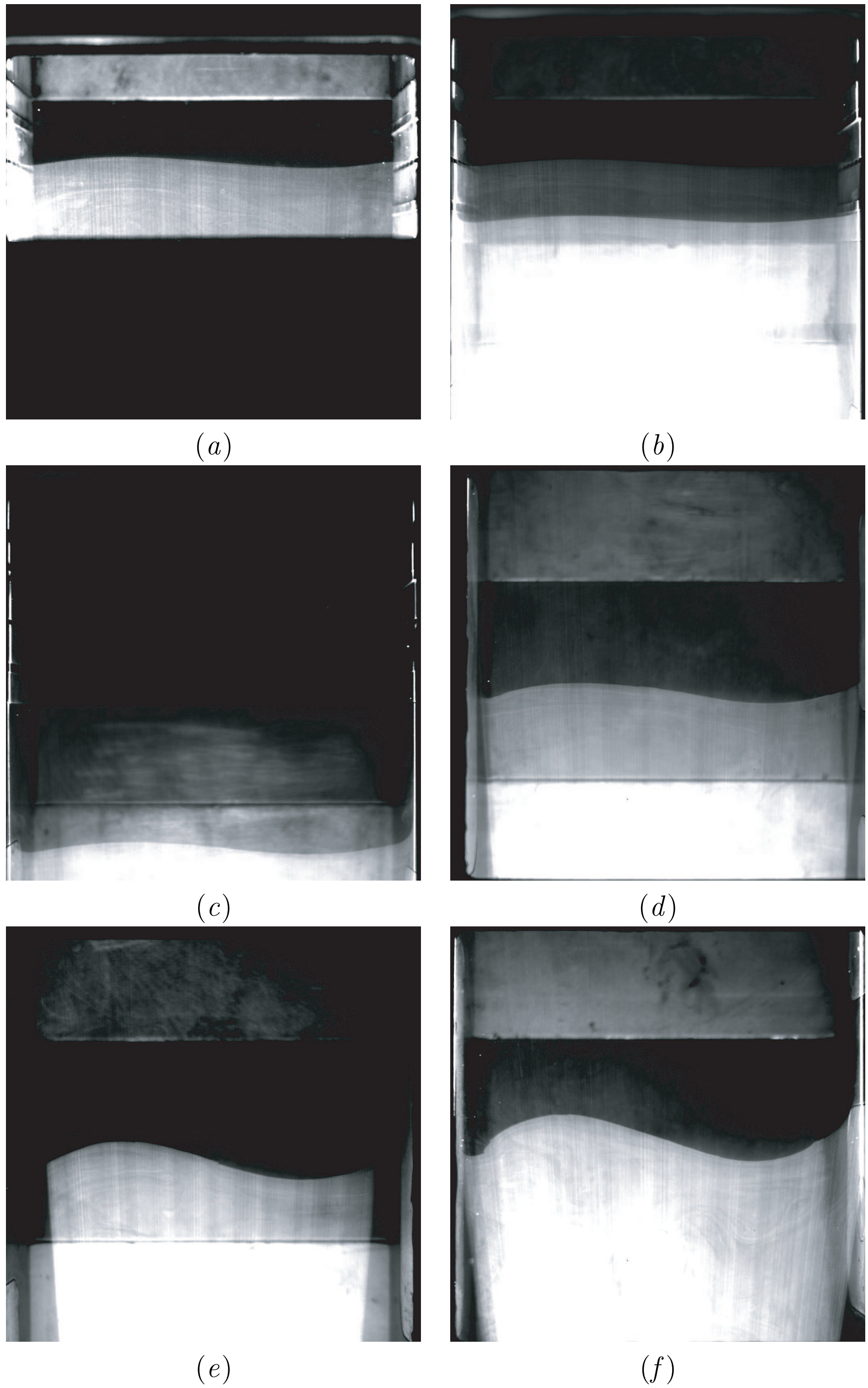

Figure 32: Time-sequence of experimental images for the (50% He + 50% Ar)/Ar, M=1.30: (a) t=0.000 ms, (b) t=0.224 ms, (c) t=0.875 ms, (d) t=1.744 ms, (e) t=3.109 ms, and (f) t=4.737 ms.

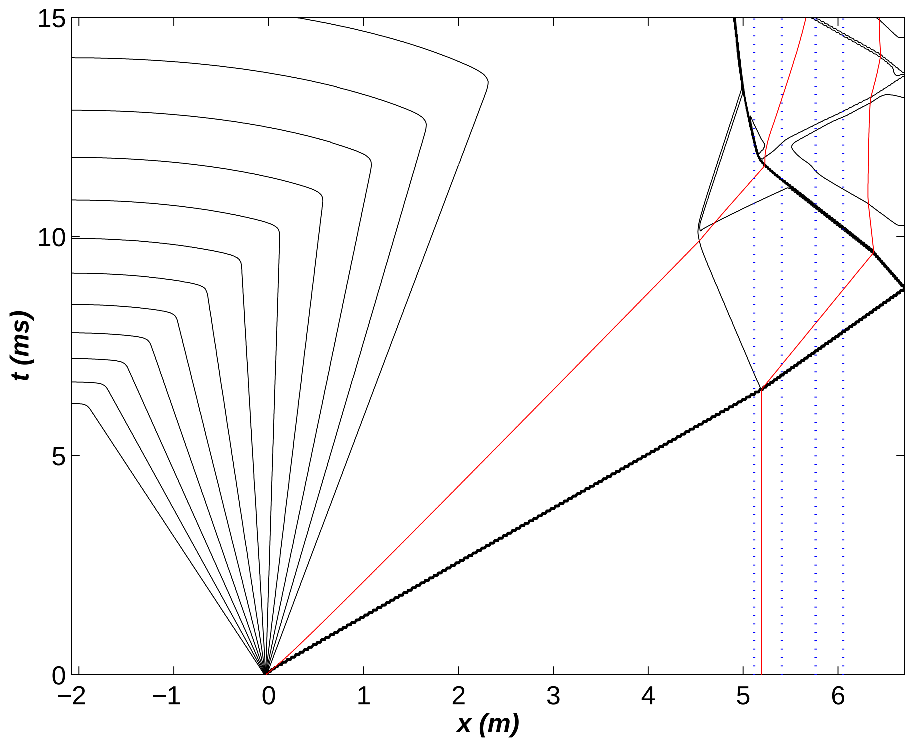

Figure 33: Wave diagram for the (50% He + 50% Ar)/Ar, M=1.90 scenario.

Exp. No.	M	A^1	η_0^0 (cm)	η_0^1 (cm)	λ (cm)	k (cm^{-1})	t_{PS1} (ms)	η_{PS1} (cm)
468	1.91	0.27	0.30	0.16	19.53	0.32	0.228	0.23
469	1.89	0.28	0.27	0.14	19.46	0.32	0.118	0.14
471	1.90	0.28	0.23	0.12	20.22	0.31	0.349	0.23
472	1.91	0.27	0.27	0.14	19.13	0.33	0.216	0.22
473	1.91	0.27	0.27	0.14	19.46	0.32	0.728	0.51
474	1.90	0.27	0.24	0.13	20.45	0.31	0.543	0.33
475	1.91	0.27	0.28	0.15	19.51	0.32	0.904	0.57
477	1.89	0.28	0.25	0.14	20.80	0.30	1.216	0.58
478	1.90	0.28	0.23	0.12	20.12	0.31	1.220	0.66
479	1.91	0.27	0.23	0.12	18.87	0.33	1.228	0.64
480	1.89	0.28	0.29	0.16	20.65	0.30	1.214	0.65
481	1.89	0.28	0.25	0.14	19.76	0.32	1.068	0.64
483	1.91	0.27	0.25	0.14	19.51	0.32	1.474	0.77
484	1.91	0.27	0.27	0.14	19.71	0.32	1.845	0.98
485	1.91	0.27	0.25	0.14	18.85	0.33	1.657	0.90
486	1.91	0.27	0.27	0.14	19.46	0.32	2.016	1.03

Table 9: Experimental parameters for the(50% He + 50% Ar)/Ar, M=1.30 RM experimental campaign.

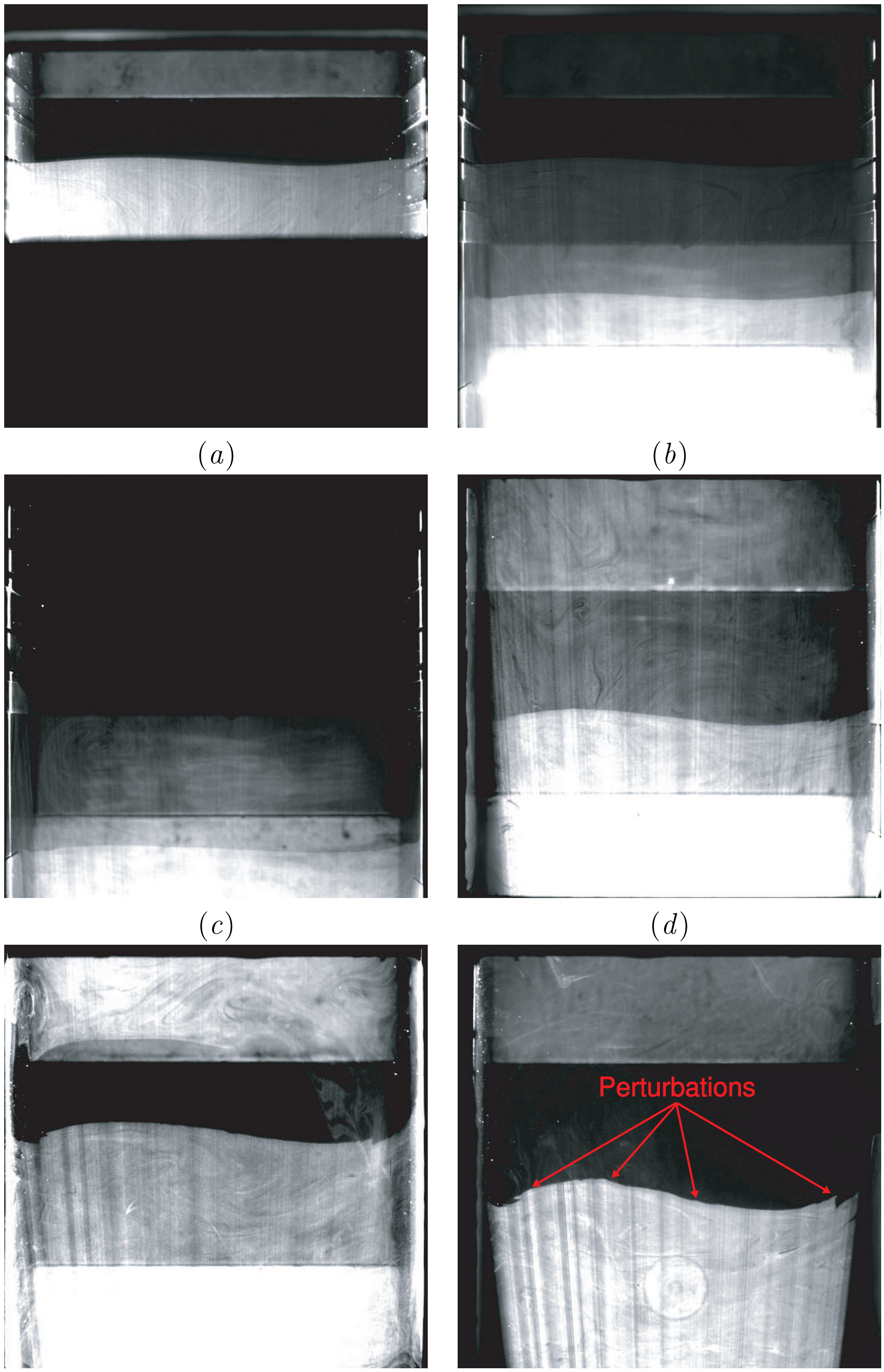

(a) (b) (c) (d) (e) (f)

Figure 34: Time-sequence of experimental images for the (50% He + 50% Ar)/Ar, M=1.90: (a) t=0.000 ms, (b) t=0.216 ms, (c) t=0.349 ms, (d) t=0.728 ms, (e) t=1.214 ms, and (f) t=1.845 ms.

4.5.3 N_2/SF_6, M=1.26

A N_2/SF_6 interface (A=0.64) is investigated at M=1.26. The light gas (N_2) is seeded with acetone vapor and the interface imaged with PLIF. A wave diagram of this scenario is given in Fig. 35. The $x-t$ plot indicates that within the viewing area, the post-shock perturbation will not be influenced by either the expansion fan or any reflected shock waves.

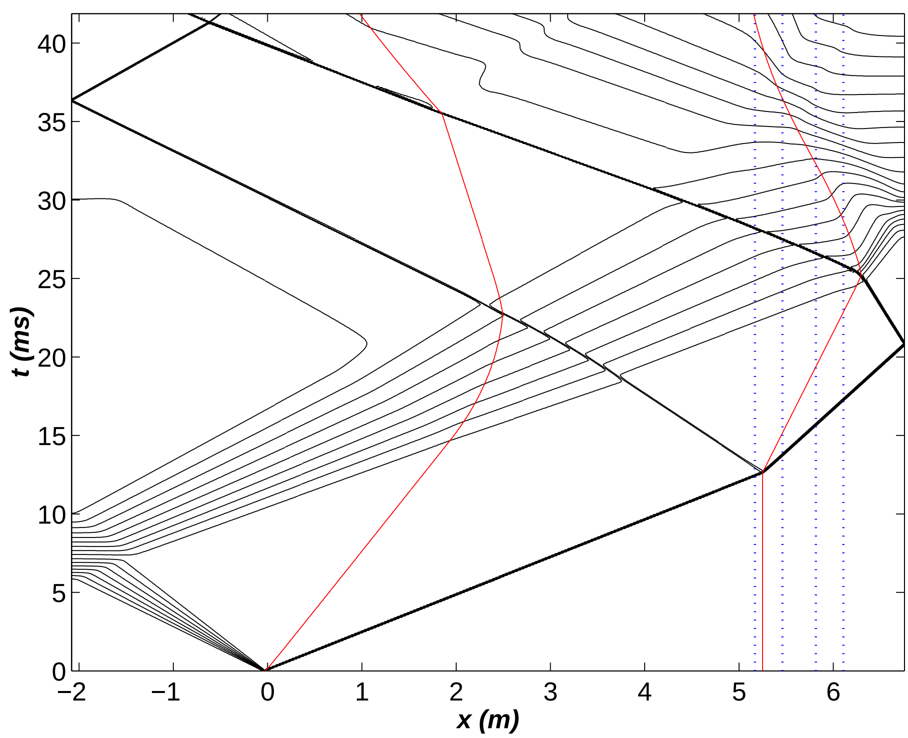

Figure 35: Wave diagram for the N_2/SF_6, M=1.26 scenario.

Growth rate data is obtained for ten experiments. The parameters for each experiment are summarized in Table 10. Two post-shock images are obtained for each experiment. The post-shock Atwood number tends to vary more in this case because of inconsistencies in the acetone seeding from one experiment to another. Three out of the ten experiments are conducted on a short wavelength perturbation ($\approx$ 9.3 cm), whereas, the rest of the experiments were conducted at a longer wavelength ($\approx$ 17.5 cm).

Exp. No.	M	A^1	η_0^0 (cm)	η_0^1 (cm)	λ (cm)	k (cm^{-1})	t_{PS1} (ms)	η_{PS1} (cm)	t_{PS2} (ms)	η_{PS2} (cm)
1	1.26	0.65	0.72	0.56	17.93	0.35	3.101	3.01	5.578	4.45
14	1.26	0.68	0.78	0.61	9.30	0.68	2.793	3.62	5.270	5.31
18	1.25	0.67	0.75	0.60	17.37	0.36	2.687	3.20	5.164	4.80
24	1.25	0.67	0.65	0.52	9.35	0.67	3.090	3.71	5.567	5.42
27	1.27	0.70	0.81	0.63	10.39	0.61	2.678	3.66	5.155	5.31
28	1.27	0.67	0.80	0.63	9.46	0.66	2.798	3.58	5.275	5.22
30	1.26	0.68	0.62	0.49	17.96	0.35	2.792	2.62	5.269	4.05
31	1.24	0.68	0.52	0.41	17.83	0.35	2.777	2.13	5.254	3.39
32	1.28	0.67	0.82	0.63	17.66	0.36	2.700	3.31	5.177	4.98
33	1.25	0.68	0.54	0.43	17.94	0.35	2.700	2.46	5.177	3.81

Table 10: Experimental parameters for the N_2/SF_6, M=1.26 RM experimental campaign.

Due to the attenuation of the excimer laser by the acetone, experimental images have been corrected with the post-processing methodology outlined in Section 4.3. A time sequence of images has been post-processed for the M=1.26 experimental campaign. Figure 36 depicts a sequence of corrected images for this case. All three images came from a single experiment (Exp. 14), and the images have been cropped to a size of approximately 10 by 13 cm. The first image is the nearly sinusoidal initial perturbation. By the first post-shock image, the interface is clearly in the non-linear growth regime where roll-up structures due to the Kelvin-Helmholtz instability are evident. The second post-shock image shows the interface progressing further into the non-linear regime to the point where secondary instabilities are starting to grow on the mushroom structure due to the Kelvin-Helmholtz instability.

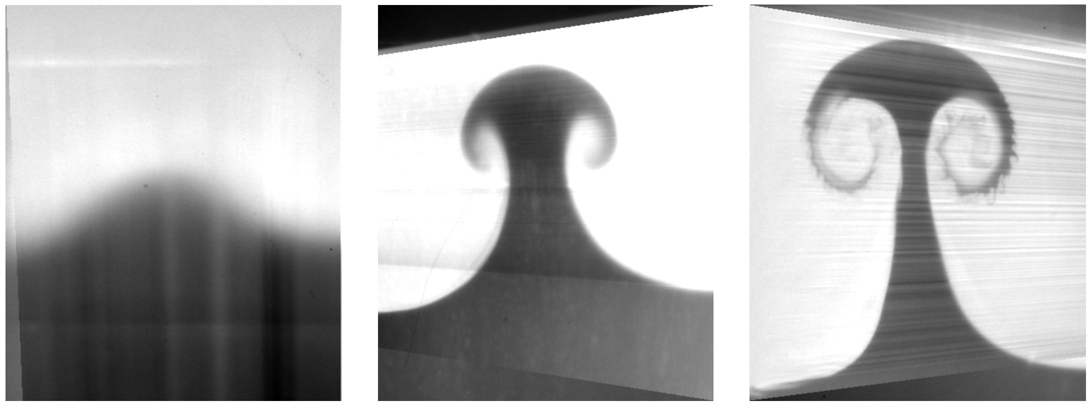

(a) (b) (c)

Figure 36: Time-sequence of experimental images for the N_2/SF_6, M=1.26 case: (a) t=0.000 ms, (b) t=2.973 ms, and (c) t=5.270 ms.

4.5.4 N_2/SF_6, M=2.05

The second set of N_2/SF_6 (A=0.68) experiments involve a gas interface accelerated by a M=2.05 shock wave. The light gas (N_2) is seeded with cigarette smoke and planar Mie scattering is used to visualize the interface. A wave diagram of this scenario is given in Fig. 37. The $x-t$ plot indicates that within the viewing area, the post-shock perturbation will not be influenced by either the expansion fan or any reflected shock waves.

Growth rate data are reported for 14 experiments. The parameters for each experiment are summarized in Table 11. One post-shock image is obtained for each experiment.

A time sequence of images for the M=2.05 case is shown in Fig. 38. Each image is approximately 25 by 25 cm and has not been post-processed. The first image of this sequence depicts the typical initial condition used for the M=2.05 experiments with the incident shock wave imaged 5.38 cm above the middle of the perturbation. This image is taken 75 μs before the shock traversed the interface. At t=0.790 ms the growth is in

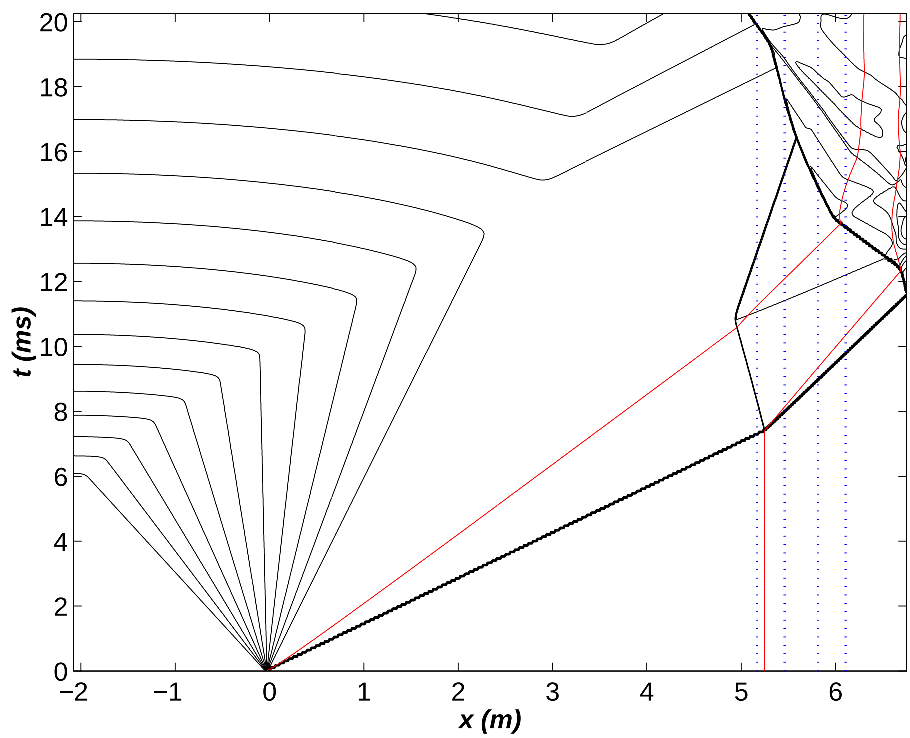

Figure 37: Wave diagram for the N_2/SF_6, M=2.05 scenario.

Exp. No.	M	A^1	η_0^0 (cm)	η_0^1 (cm)	λ (cm)	k (cm^{-1})	t_{PS1} (ms)	η_{PS1} (cm)
150	2.06	0.77	0.64	0.38	17.28	0.36	2.473	4.64
153	2.07	0.77	0.78	0.46	17.00	0.37	2.476	5.50
154	2.05	0.77	0.87	0.51	16.82	0.37	2.465	5.51
155	2.05	0.77	0.90	0.53	16.30	0.39	2.464	5.44
156	2.06	0.77	0.71	0.42	16.38	0.38	2.304	4.75
157	2.05	0.77	0.95	0.56	16.30	0.39	2.212	5.38
158	2.05	0.77	0.94	0.55	16.30	0.39	1.615	4.27
159	2.06	0.77	0.93	0.55	16.20	0.39	1.660	4.28
162	2.06	0.77	0.93	0.55	16.52	0.38	1.661	4.23
163	2.05	0.77	0.81	0.47	17.72	0.36	1.742	4.00
165	2.05	0.77	0.94	0.55	16.23	0.39	1.742	4.46
166	2.06	0.77	0.91	0.54	16.73	0.38	0.789	2.79
167	2.05	0.77	0.74	0.43	17.72	0.36	0.788	2.17
168	2.05	0.77	0.74	0.43	17.53	0.36	0.789	2.15
169	2.06	0.77	0.97	0.57	16.29	0.39	0.790	2.80

Table 11: Experimental parameters for the N_2/SF_6, M=2.05 RM experimental campaign.

the early stages of the non-linear regime. By a time of t=1.661 ms the development of the perturbation is similar to that seen in Fig. 36 at t=5.270 ms. The RM instability develops more rapidly for the case of the stronger shock. In Fig. 38, at t>2.0 ms the spike becomes more narrow and the bubble becomes flat as the stronger vorticity from the M=2.05 shock pulls more fluid from the bubble, through the spike, to the mushroom structure. The flattening of the bubble is due to compressibility effects, which occur when the velocity of the interface is greater than the sound speed in the shocked heavy gas ($V_0/c_{tr} \geq 1$). Compressibility effects will be discussed in more detail in Section 5.1.

4.5.5 N_2/SF_6, M=2.86

A third set of N_2/SF_6 (A=0.68) experiments involve a gas interface accelerated by a M=2.86 shock wave. The heavy gas (SF_6) is seeded with an atomized hydrocarbon oil and planar Mie scattering is used to visualize the interface. A wave diagram of this scenario is given in Fig. 39. The $x - t$ plot indicates that within the viewing area, the post-shock perturbation will not be influenced by either the expansion fan or any reflected shock waves.

Growth rate data is obtained for 11 experiments. The parameters for each experiments are summarized in Table 12. One post-shock image is obtained for each experiment.

A time sequence of images for the M=2.86 case is shown in Fig. 40. Each image is approximately 25 by 25 cm and has not been post-processed. The first image is the initial condition. At the first post-shock time (t=0.053), the amplitude of the interface is smaller than the initial pre-shock amplitude and the transmitted shock wave is directly below the interface (indicated by an arrow in the image). The transmitted shock wave

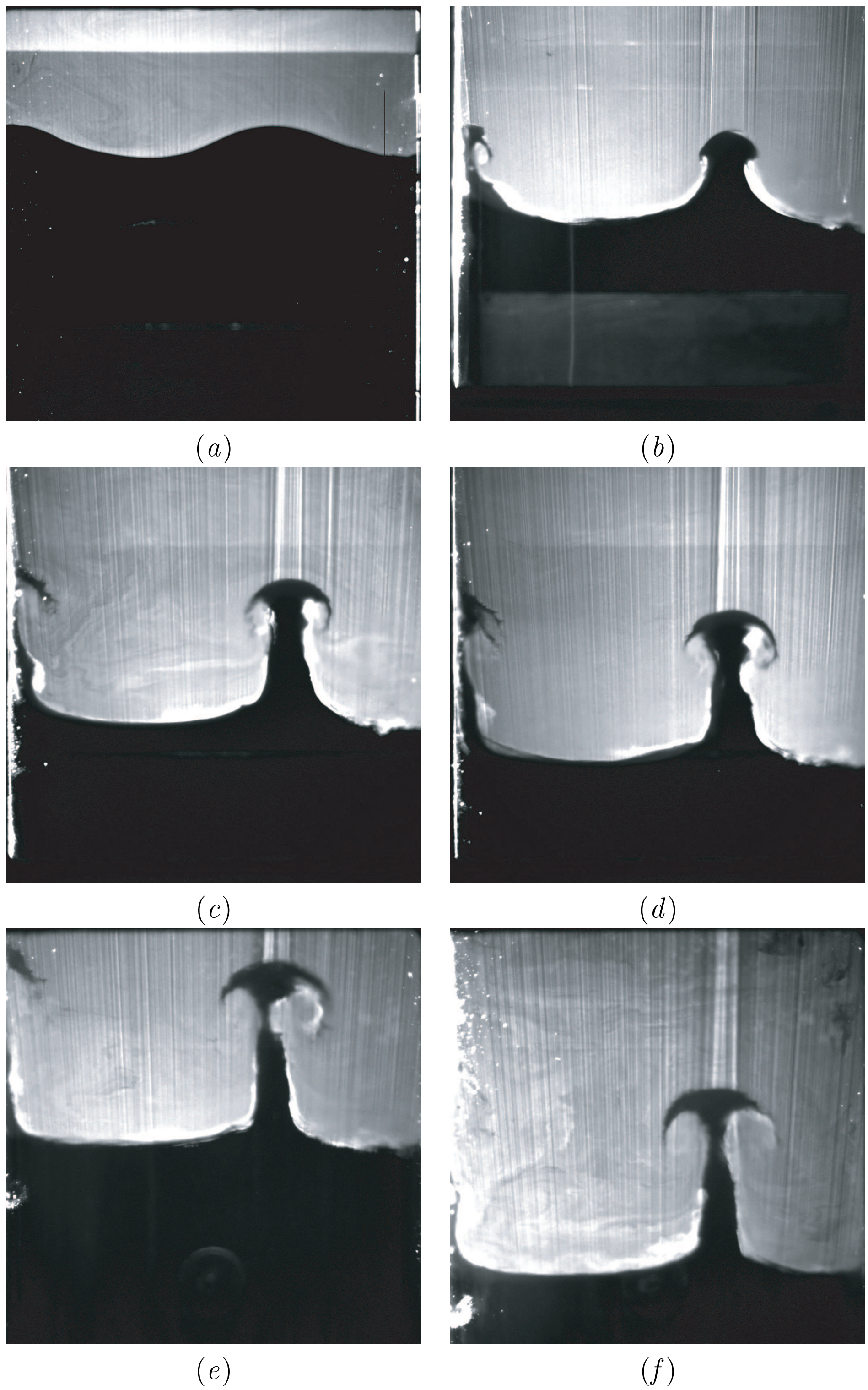

Figure 38: Time-sequence of experimental images for the N_2/SF_6, M=2.05 case: (a) t=0.000 ms, (b) t=0.790 ms, (c) t=1.661 ms, (d) t=1.742 ms, (e) t=2.212 ms, and (f) t=2.464 ms.

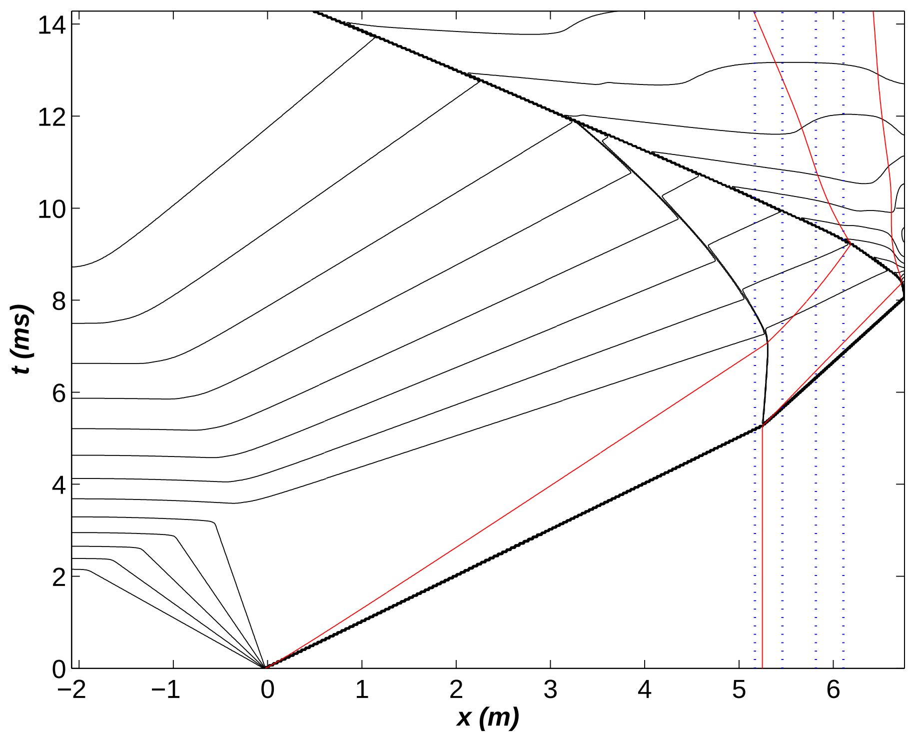

Figure 39: Wave diagram for the N_2/SF_6, M=2.86 scenario.

Exp. No.	M	A^1	η_0^0 (cm)	η_0^1 (cm)	λ (cm)	k (cm^{-1})	t_{PS1} (ms)	η_{PS1} (cm)
416	2.84	0.80	0.90	0.46	16.92	0.37	0.923	3.91
420	2.86	0.80	0.98	0.50	16.97	0.37	0.198	0.97
421	2.87	0.80	1.21	0.62	17.34	0.36	0.132	0.93
422	2.84	0.80	1.07	0.55	17.22	0.36	0.053	0.69
423	2.86	0.80	1.14	0.59	17.48	0.36	0.446	2.63
424	2.87	0.80	1.09	0.56	17.25	0.36	0.578	3.14
425	2.87	0.80	0.94	0.48	17.73	0.35	0.325	1.60
426	2.88	0.80	1.03	0.53	17.32	0.36	0.950	4.19
428	2.87	0.80	1.07	0.55	17.60	0.36	0.749	3.78
429	2.88	0.80	0.99	0.51	17.35	0.36	1.151	4.53
430	2.88	0.80	1.08	0.55	17.78	0.35	1.401	5.35

Table 12: Experimental parameters for the N_2/SF_6, M=2.86 RM experimental campaign.

front has been imprinted by the initial perturbation. The transmitted shock follows close to the interface throughout the entire viewing area because the difference in speed between the interface and the transmitted shock is relatively small (on the order of 50 m/s). At a post-shock time of t=0.950 ms the transmitted wave is once again planar. The non-linear growth regime appears to commence at approximately t=0.2 ms. At this time, small perturbation develop on the bubble portion of the interface. After this time the bubble region becomes a turbulent mixing region where there is no longer a sharp interface. At $t\approx$0.950, the spike forms the characteristic mushroom structure, however, the sides of the structure are not visible due to turbulent mixing. At t=1.401 the curvature of the bubble reduces to the point where the bubble is flat due to compressibility effects as mentioned for the N_2/SF_6, M=2.05 case. For this case, the boundary between the spike and the bubble approaches a right angle.

4.5.6 He/SF_6, M=1.13

A He/SF_6 interface (A=0.95) is investigated at M=1.13. The heavy gas (SF_6) is seeded with cigarette smoke and planar Mie scattering is used to visualize the interface. A wave diagram of this scenario is given in Fig. 41. The $x - t$ plot indicates that within the viewing area, the post-shock perturbation will not be influenced by either the expansion fan or the reflected shock wave off of the bottom of the shock tube. However, the $x - t$ plot does show that the interface will be subjected to a shock wave traveling in the same direction as the initial incident shock at approximately t=7 ms after the incident shock wave traverses the initial perturbation. This shock wave is a result of the initially reflected shock wave from the interface traversing the driver/driven contact surface and causing another reflected shock wave to travel back towards the interface. It is assumed

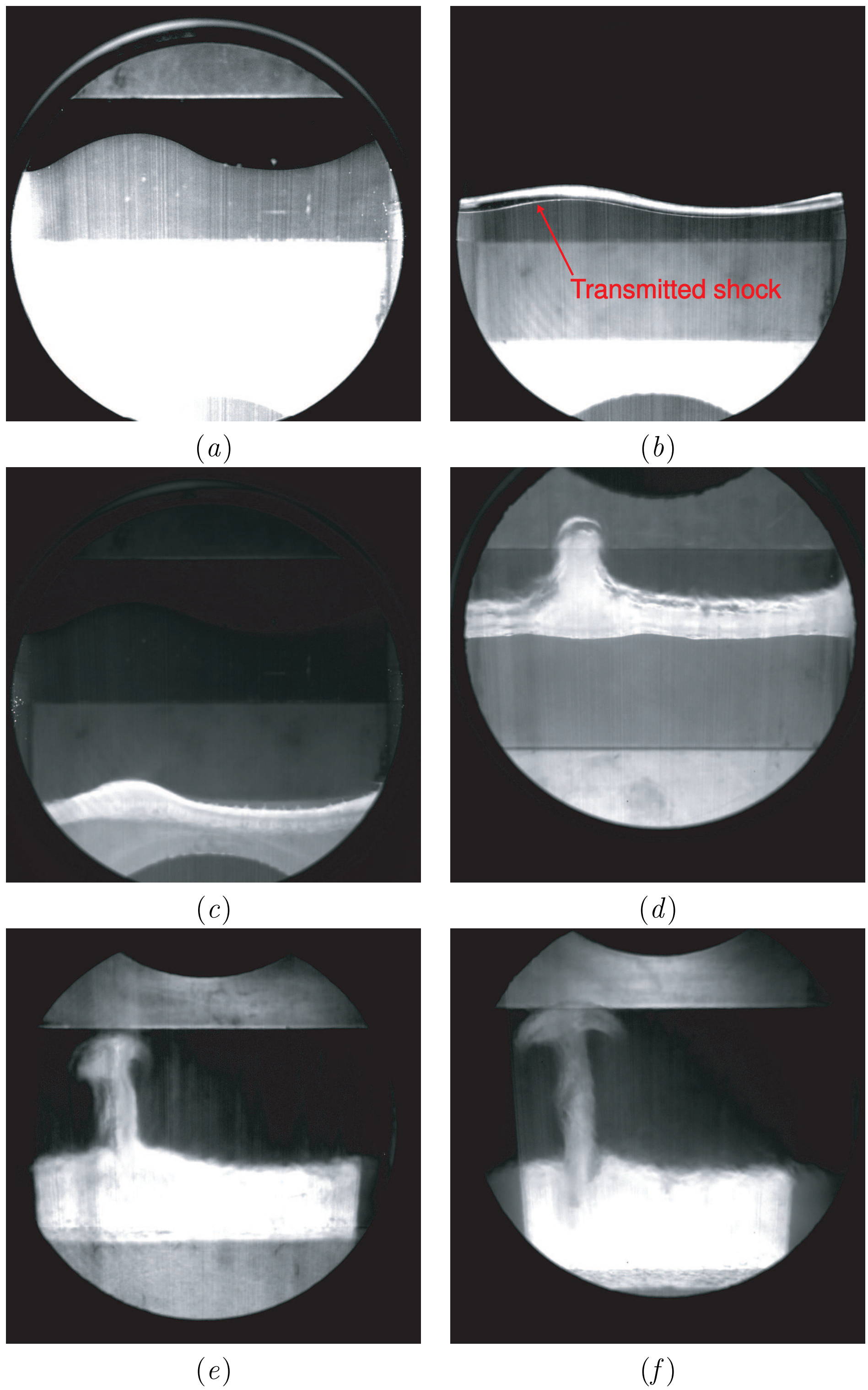

Figure 40: Time-sequence of experimental images for the N_2/SF_6, M=2.86 case: (a) t=0.000 ms, (b) t=0.053 ms, (c) t=0.198 ms, (d) t=0.446 ms, (e) t=0.950 ms, and (f) t=1.401 ms.

that the reflected shock wave traversing the interface at t=12 ms (point A in the figure) has only a small effect on the growth of the perturbation because it is a weak disturbance.

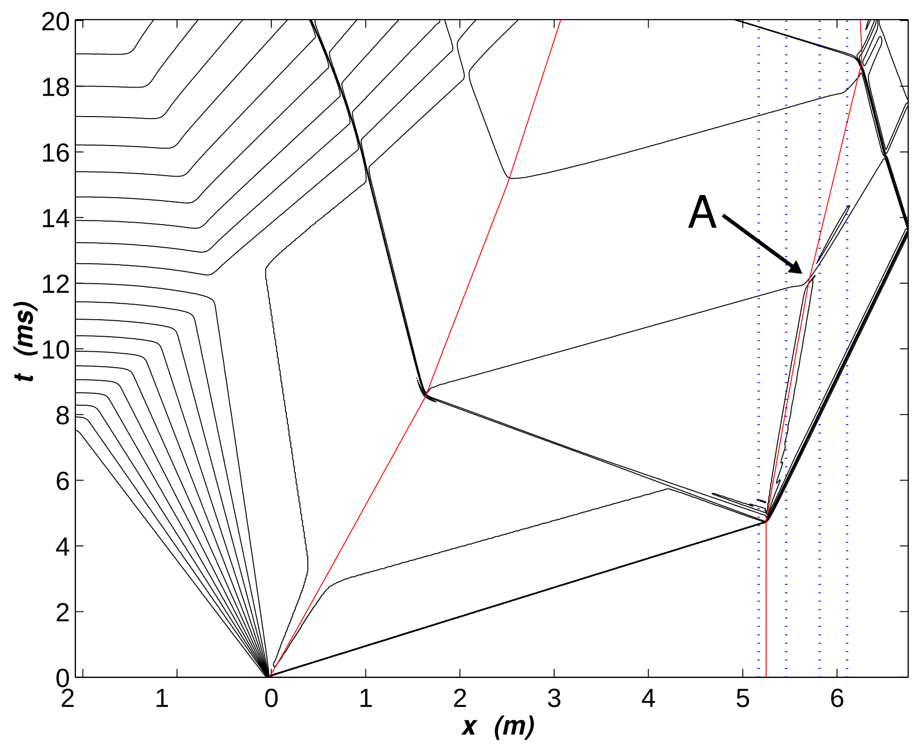

Figure 41: Wave diagram for the He/SF_6, M=1.13 scenario.

Growth rate data are obtained for 22 experiments. The parameters for each experiments are summarized in Table 13. One post-shock image is obtained for each experiment. The low Mach number studied for this campaign allows for the investigation of very late time (t≈9.0 ms) post-shock images. Peak-to-peak amplitudes for these late time images extend up to almost 37 cm, which is the largest perturbation amplitudes seen in the entire parameter study.

A time sequence of images for the M=1.13 case is shown in Fig. 42. Each image

Exp. No.	M	A^1	η_0^0 (cm)	η_0^1 (cm)	λ (cm)	k (cm^{-1})	t_{PS1} (ms)	η_{PS1} (cm)
282	1.13	0.95	1.21	1.14	17.81	0.35	2.361	5.35
283	1.14	0.95	1.52	1.44	17.09	0.37	2.669	6.79
284	1.13	0.95	1.66	1.57	16.64	0.38	3.317	8.01
285	1.13	0.95	1.56	1.48	16.99	0.37	1.017	3.91
286	1.13	0.95	1.27	1.20	17.70	0.35	0.359	1.85
287	1.13	0.95	1.57	1.49	17.15	0.37	0.196	1.93
289	1.13	0.95	1.57	1.49	17.12	0.37	1.567	5.04
291	1.14	0.95	1.55	1.46	16.66	0.38	3.618	8.46
292	1.13	0.95	1.57	1.49	16.38	0.38	4.517	9.49
295	1.14	0.95	1.46	1.38	16.97	0.37	5.519	10.80
296	1.13	0.95	1.35	1.28	17.68	0.36	6.517	11.29
298	1.13	0.95	1.50	1.42	17.35	0.36	7.036	12.50
299	1.13	0.95	1.28	1.22	17.53	0.36	6.038	10.62
300	1.14	0.95	1.52	1.44	16.38	0.38	5.038	10.24
302	1.14	0.95	1.51	1.43	16.36	0.38	6.239	11.85
303	1.13	0.95	1.55	1.47	17.45	0.36	8.716	16.37
304	1.13	0.95	1.47	1.39	16.26	0.39	9.238	16.24
306	1.13	0.95	1.61	1.52	16.38	0.38	9.717	18.21
307	1.13	0.95	1.66	1.57	16.97	0.37	9.615	18.36
308	1.14	0.95	1.49	1.40	16.56	0.38	9.020	16.75
309	1.14	0.95	1.51	1.43	16.31	0.39	9.379	16.94
310	1.13	0.95	1.68	1.58	16.94	0.37	9.016	17.55

Table 13: Experimental parameters for the He/SF_6, M=1.13 RM experimental campaign.

is approximately 25 by 40 cm and has not been post-processed. Large post-shock amplitudes have made it necessary to often splice images from two consecutive windows. When images are spliced together, they are attached at reference points within the shock tube that are the result of taking ruler images that span both windows. The first image is the initial condition. The initial amplitude is large with respect to the wavelength and this results in almost the entire growth sequence being in the non-linear growth regime. At t=0.359 ms the perturbation is definitely in the non-linear regime as the spike is starting to narrow as the bubble is broadening. A few centimeters below the interface is the transmitted shock which has been imprinted by the initial condition. At t=2.669 ms a mushroom structure is starting to develop. From this image forward, an asymmetry develops which favors additional growth on the side of the mushroom structure that is nearest the center of the tube. This is primarily due to reflected shock and rarefaction waves bouncing off the sides walls and interacting with the spike.

As the growth develops further into the non-linear regime, the spike narrows and starts to bend. Throughout the entire image sequence, the mushroom structure does not roll-up as seen in Fig. 36 (c). Instead, the fluid just flows down the sides of the mushroom, without rolling up. Although there is a lack of a roll-up structure, there is still vorticity at the tip of the spike pulling the heavier gas up the shaft of the spike. This is causing the shaft of the spike to elongate as well as the lengthening of the mushroom sides. The reason the roll-up structure is not witnessed is because the light helium fluid does not have enough momentum to roll-up the heavy SF_6, and therefore, the SF_6 flows down the side of the mushroom.

At times greater than t=6.0 ms, secondary instabilities are seen along the mushroom structure and the spike shaft due to differences in velocity between the light and heavy

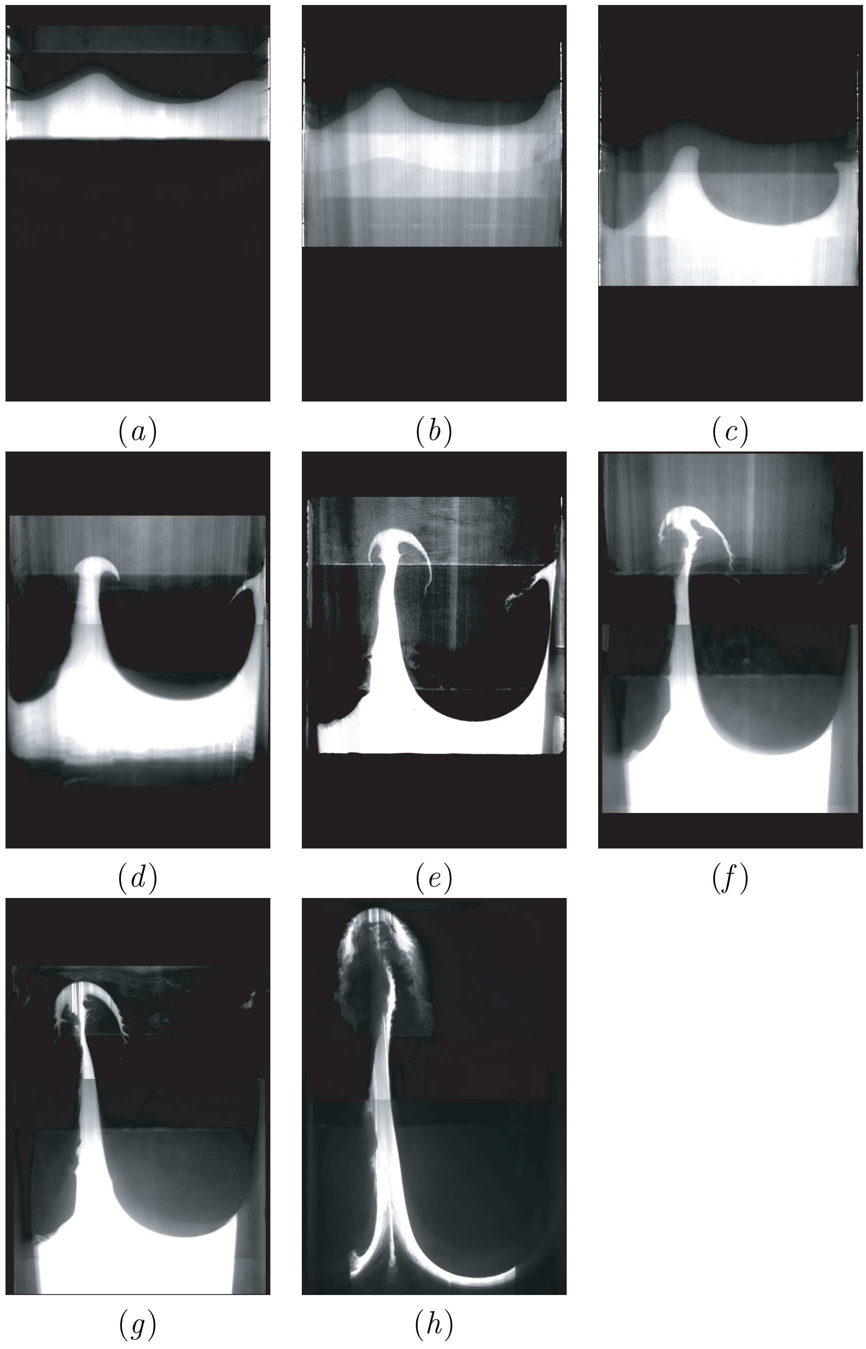

Figure 42: Time-sequence of experimental images for the He/SF$_6$, M=1.13 case: (a) t=0.000 ms, (b) t=0.359 ms, (c) t=1.017 ms, (d) t=2.669 ms, (e) t=4.517 ms, (f) t=6.239 ms, (g) t=7.036 ms, and (h) t=9.615 ms.

fluids. At t=9.615 ms turbulent mixing is seen along the ends of the mushroom structure and the tip of the spike is starting to "pinch off" from the spike shaft. The vorticty at the tip of the spike is continually trying to pull fluid up the spike shaft. As the spike elongates, it narrows to a point where no more fluid can be transported to the tip, and the tip pinches off. The cigarette smoke seeding also enables the viewing of a slip surface at the base of the spike at t=9.615 ms. The slip surface is a result of heavy fluid being pulled up the spike by the vorticity at the tip of the spike. The heavy fluid is pulled from the two bubble regions adjacent to the spike which creates a region where fluid being pulled up the spike has a different velocity than the fluid not being pulled up the spike. The slip surface is present at all times, however the reason it is visualized at the late time is because the thickness of the pre-shock cigarette smoke layer is smaller than the other experiments presented. Therefore, the slip surface is outlined by the smoke instead of being covered by a sheet of smoke that extends past the slip surface.

4.5.7 He/SF_6, M=1.41

A He/SF_6 interface (A=0.95) is investigated at M=1.41. The heavy gas (SF_6) is seeded with cigarette smoke and planar Mie scattering is used to visualize the interface. A wave diagram of this scenario is given in Fig. 43. The $x-t$ plot indicates that within the viewing area, the post-shock perturbation is influenced by a reflected shock wave off of the driver/driven contact surface in the same manner as the M=1.13 case. The contact-surface-reflected shock wave traverses the interface approximately 4 ms after the initial incident shock wave traverses the interface (approximately t=8 ms).

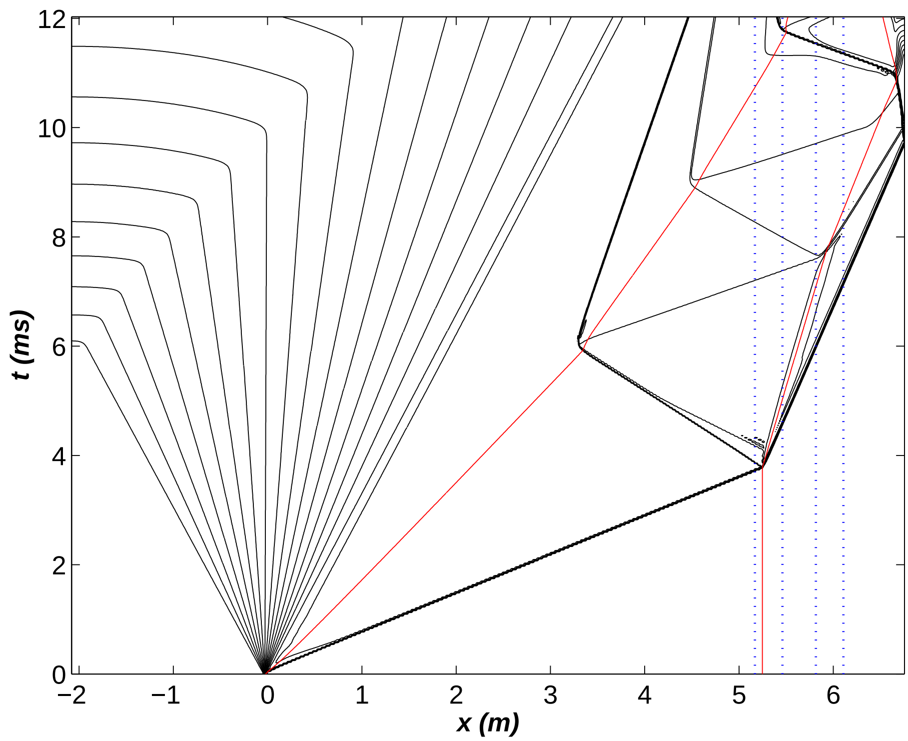

Figure 43: Wave diagram for the He/SF_6, M=1.41 scenario.

Growth rate data is obtained for 25 experiments. The parameters for each experiments are summarized in Table 14. One post-shock image is obtained for each experiment.

Exp. No.	M	A^1	η_0^0 (cm)	η_0^1 (cm)	λ (cm)	k (cm^{-1})	t_{PS1} (ms)	η_{PS1} (cm)
314	1.41	0.96	1.32	1.16	15.98	0.39	0.525	2.95
316	1.39	0.96	1.47	1.30	16.94	0.37	0.521	3.11
317	1.41	0.96	1.17	1.03	15.72	0.40	0.769	3.48
318	1.40	0.96	1.42	1.25	17.09	0.37	1.066	4.98
319	1.40	0.96	1.32	1.16	15.98	0.39	1.367	5.49
322	1.41	0.96	1.24	1.09	17.63	0.36	1.669	6.15
323	1.41	0.96	1.47	1.30	16.97	0.37	1.667	6.91
324	1.42	0.96	1.45	1.27	17.15	0.37	0.369	2.46
325	1.42	0.96	1.33	1.17	15.88	0.40	0.170	1.57
326	1.41	0.96	1.44	1.26	16.46	0.38	0.068	1.32
327	1.42	0.96	1.40	1.23	17.30	0.36	0.034	1.12
328	1.41	0.96	1.40	1.23	17.17	0.37	1.218	5.38
329	1.42	0.96	1.44	1.26	16.69	0.38	0.634	3.52
330	1.41	0.96	1.19	1.05	17.86	0.35	0.910	3.99
331	1.41	0.96	1.35	1.18	17.32	0.36	1.969	7.37
336	1.42	0.96	1.50	1.31	16.64	0.38	2.269	8.80
337	1.43	0.96	1.16	1.01	15.34	0.41	2.572	8.04
338	1.43	0.96	1.42	1.25	16.31	0.39	2.770	9.77
339	1.42	0.96	1.50	1.31	16.59	0.38	2.970	10.54
340	1.42	0.96	1.54	1.35	16.51	0.38	2.119	8.57
342	1.42	0.96	1.36	1.19	15.93	0.39	2.420	8.60
344	1.42	0.96	1.46	1.28	16.89	0.37	3.569	11.72
345	1.42	0.96	1.18	1.04	17.83	0.35	3.272	10.16
347	1.42	0.96	1.42	1.25	17.32	0.36	3.770	12.21
348	1.42	0.96	1.49	1.30	16.94	0.37	4.019	13.01

Table 14: Experimental parameters for the He/SF_6, M=1.41 RM experimental campaign.

A time sequence of images for the M=1.41 case is shown in Fig. 44. Each image is approximately 25 by 40 cm and has not been post-processed, although the pixel intensity and contrast are both adjusted. The first image (a) is the initial condition. The development of the perturbation for the M=1.41 case is similar to the M=1.13 case. Similar features are seen at an earlier time. The shape of Fig. 44 (f) looks the same as Fig. 42 (e), each has a similarly shaped mushroom structure, however the M=1.41 images occur 2.548 ms before the M=1.13 one. From t=1.367 ms forward, small pockets of fluid develop along a slip surface (same slip surface discussed for the M=1.13 case) that do not contain cigarette smoke. The pockets of fluid without smoke are small voritices along the slip surface that, due to a centripetal force, eject the smoke to the edge of the vorticy. These fluid pockets also outline additional slip surfaces that are created due to reflected pressure and expansion waves that are present between the interface and the transmitted shock front.

Some of the images at t>1.0 ms also exhibit a triangle structure (indicated by arrows in figure) that is outlined by the slip surface, but also extends past the smoke layer in other parts of the interface. The cigarette smoke layer has a finite thickness that does not extend to the bottom of the shock tube. The finite smoke layer is compressed by the shock wave, and travels at the post-shock particle velocity in the same direction as the incident shock wave. The vorticity at the tip of the spike pulls some of the fluid up the spike causing a relative reduction in the overall velocity of the fluid in the incident shock wave direction. The velocity within the bounds of the slip surface is not as influenced by the spike vorticty and therefore has a greater velocity which makes the triangle appear to be jetting away from the spike. It is also observed that at late times the curvature of the bubble reduces to the point where the bubble is nearly flat due to compressibility effects.

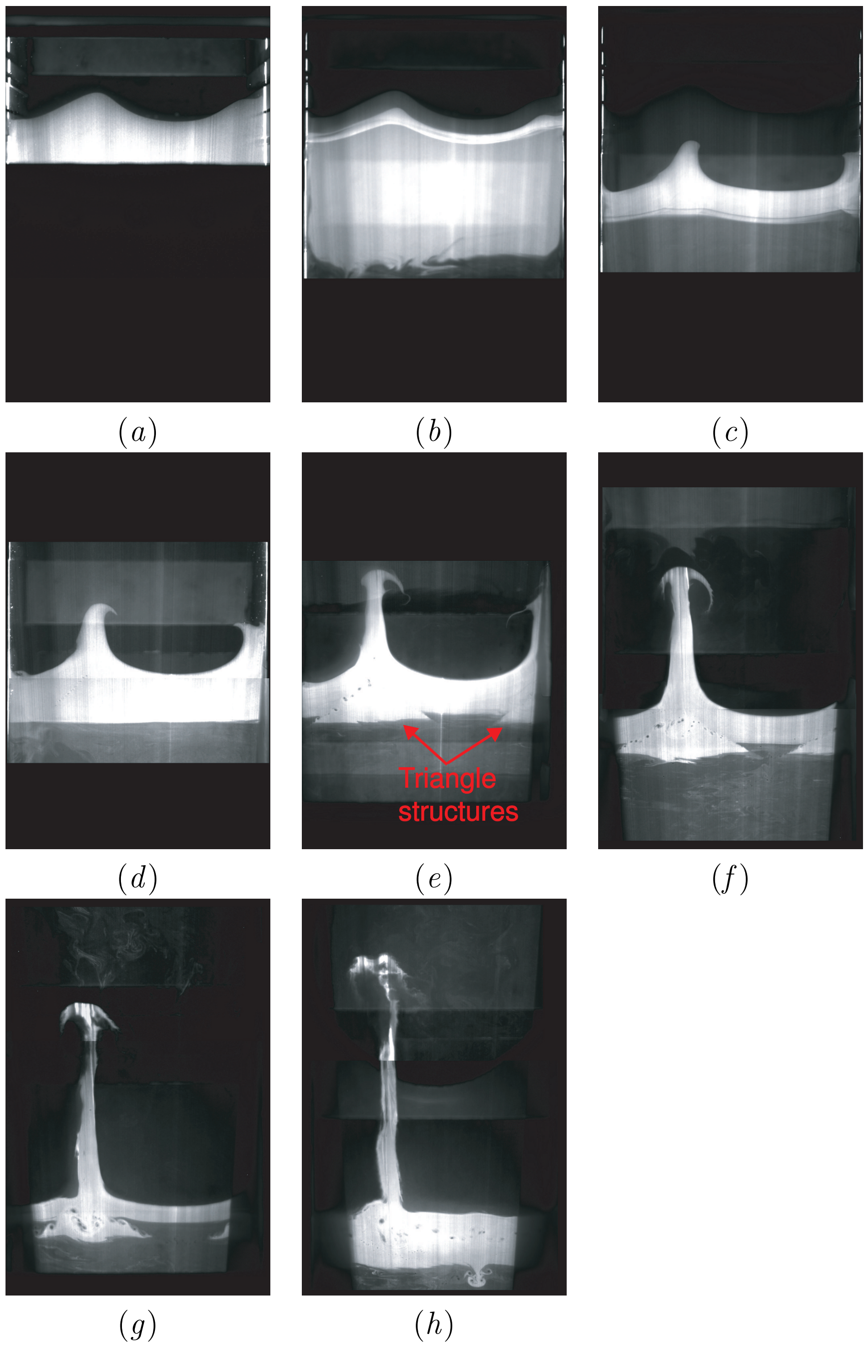

Figure 44: Time-sequence of experimental images for the He/SF_6, M=1.41 case: (a) t=0.000 ms, (b) t=0.068 ms, (c) t=0.369 ms, (d) t=0.769 ms, (e) t=1.367 ms, (f) t=1.969 ms, (g) t=2.770 ms, and (h) t=3.770 ms.

4.5.8 He/SF$_6$, M=1.95

A He/SF$_6$ interface (A=0.95) is investigated at M=1.95. The heavy gas (SF$_6$) is seeded with cigarette smoke and planar Mie scattering is used to visualize the interface. A wave diagram of this scenario is given in Fig. 45. The $x-t$ plot indicates that within the viewing area, the post-shock perturbation is influenced by a reflected shock wave from the driver/driven contact surface in the same manner as the M=1.13 case. The contact surface reflected shock wave traverses the interface at approximately 2 ms after the initial incident shock wave traverses the interface (approximately t=5 ms).

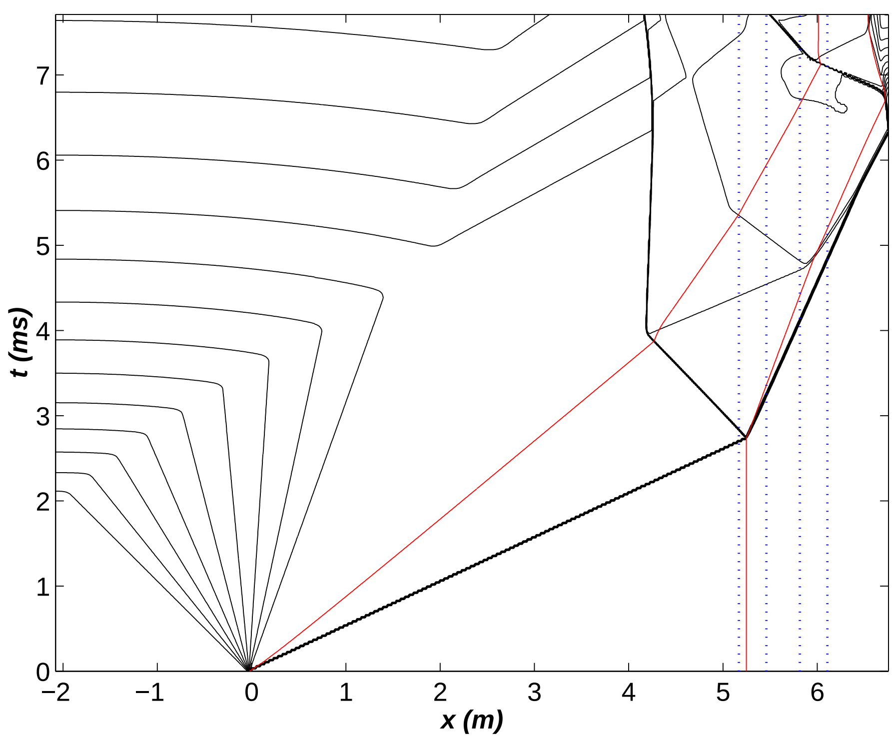

Figure 45: Wave diagram for the He/SF$_6$, M=1.95 scenario.

Growth rate data is obtained for 18 experiments. The parameters for each experiments are summarized in Table 15. One post-shock image is obtained for each experiment.

Exp. No.	M	A^1	η_0^0 (cm)	η_0^1 (cm)	λ (cm)	k (cm^{-1})	t_{PS1} (ms)	η_{PS1} (cm)
368	1.96	0.97	1.46	1.20	17.02	0.37	0.388	3.26
369	1.96	0.97	1.54	1.26	17.37	0.36	0.272	2.68
370	1.96	0.97	1.42	1.16	17.04	0.37	0.172	1.91
372	1.95	0.97	1.44	1.18	16.59	0.38	0.072	1.31
373	1.95	0.97	1.41	1.16	16.84	0.37	0.221	2.13
374	1.94	0.97	1.41	1.16	17.53	0.36	0.670	4.74
375	1.95	0.97	1.41	1.16	16.97	0.37	0.521	3.48
376	1.96	0.97	1.19	0.98	16.03	0.39	0.273	2.18
377	1.96	0.97	1.42	1.16	16.97	0.37	0.073	1.28
378	1.96	0.97	1.03	0.84	15.44	0.41	0.824	4.65
379	1.95	0.97	1.27	1.04	16.43	0.38	0.822	5.46
380	1.95	0.97	1.45	1.19	17.04	0.37	1.071	6.71
381	1.95	0.97	1.46	1.20	17.04	0.37	1.271	8.05
382	1.96	0.97	1.24	1.02	15.95	0.39	1.474	8.56
383	1.95	0.97	1.33	1.09	16.31	0.39	1.472	8.83
385	1.95	0.97	1.47	1.21	16.89	0.37	1.771	10.66
386	1.94	0.97	1.31	1.07	16.74	0.38	1.970	11.10
388	1.95	0.97	1.27	1.04	16.41	0.38	1.621	9.07

Table 15: Experimental parameters for the He/SF_6, M=1.13 RM experimental campaign.

A time sequence of images for the M=1.95 case is shown in Fig. 46. Each image is approximately 25 by 40 cm and has not been post-processed. The growth of the perturbation at M=1.95 occurs on a shorter time scale than the previous lower Mach number He/SF_6 experiments due to more baroclinic vorticity being generated on the interface as a result of a larger pressure jump across the stronger shock wave. In the non-linear regime, the sides of the mushroom structure do not extend downward past the tip of the spike. This is a result of the heavy fluid coming up the spike to the tip followed by turbulently mixing. At late times, the entire interface (spike shaft, spike tip, and bubble) appears to be turbulently mixing. In the M=1.95 case, the vorticity pockets visualized in the M=1.41 case are larger and more pronounced. Below the spike (Fig. 46 (e), (f), (g), and (h)), a circular area of vorticity is being generated at the intersection of the two major slip surfaces. This may be considered an extension and evolution of the triangular structure described in Section 4.5.7. As seen in the M=1.41 case, the bubble flattens out in this case at $t \approx 1.5$ ms.

4.6 Re-shock: (50% He + 50% Ar)/Ar, M=1.30

A preliminary study of a re-shocked (50% He + 50% Ar)/Ar interface is conducted at M=1.30 to provide verification that this type of study is feasible. The re-shock campaign consists of four experiments that probe the extents of time in which re-shock images can be obtained, which is the time between when the interface is traversed by a second shock wave traveling in the opposite direction as the initial shock wave (due to reflection from the shock tube end wall) and when the expansion fan interacts with the interface. Due to the setup of the modular driven section, the actual re-shock of the interface occurs just below the last window. For future studies, the shock tube would need to be rearranged to better suit this experimental campaign. Figure 47 is a time sequence of re-shocked images. Each image is approximately 25 by 25 cm and has not been post-processed. The circular object on the back wall of the shock tube in each image is a pressure transducer flange.

The first image is the initial condition for the initial incident shock wave. Figure 47

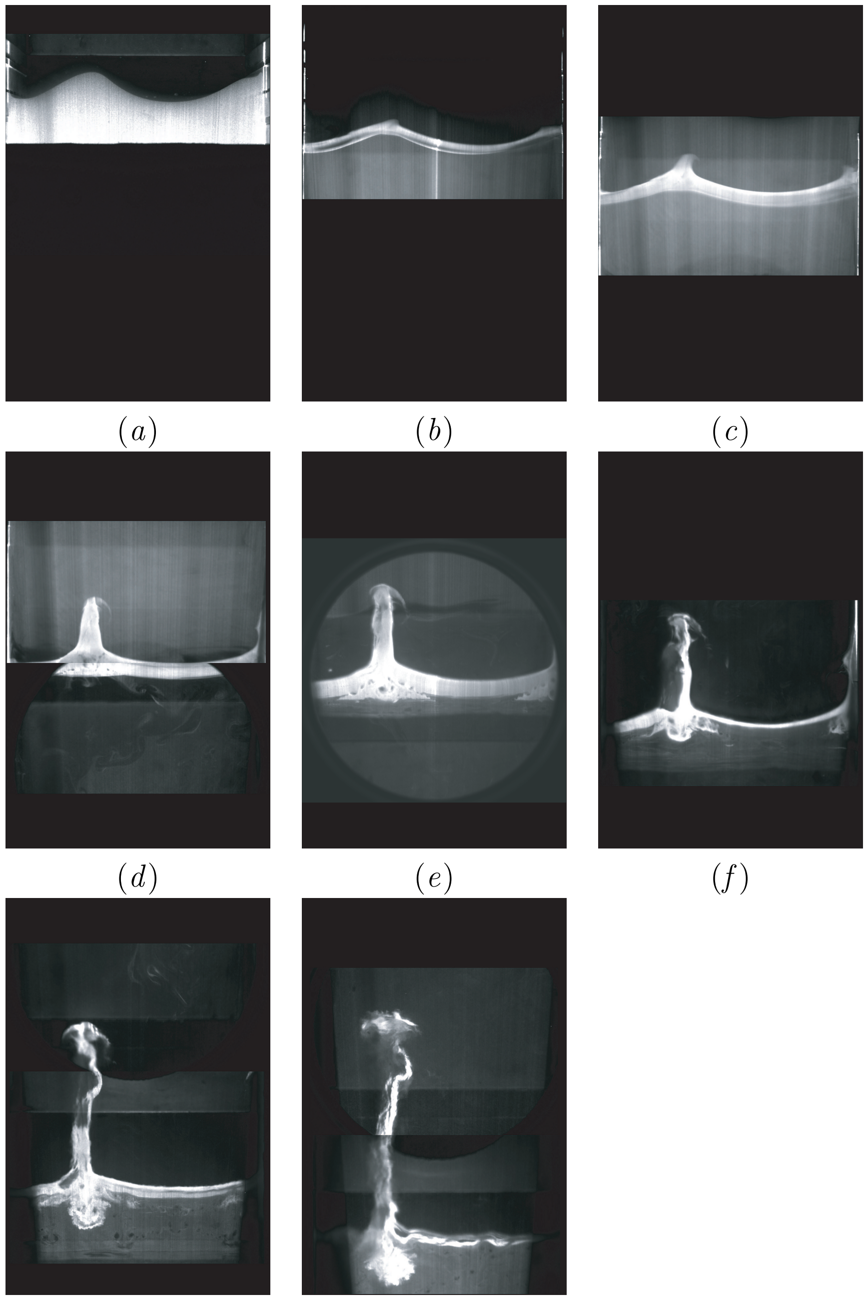

(a) (b) (c) (d) (e) (f) (g) (h)

Figure 46: Time-sequence of experimental images for the He/SF_6, M=1.95 case: (a) t=0.000 ms, (b) t=0.073 ms, (c) t=0.172 ms, (d) t=0.388 ms, (e) t=0.670 ms, (f) t=0.822 ms, (g) t=1.271 ms, and (h) t=1.771 ms.

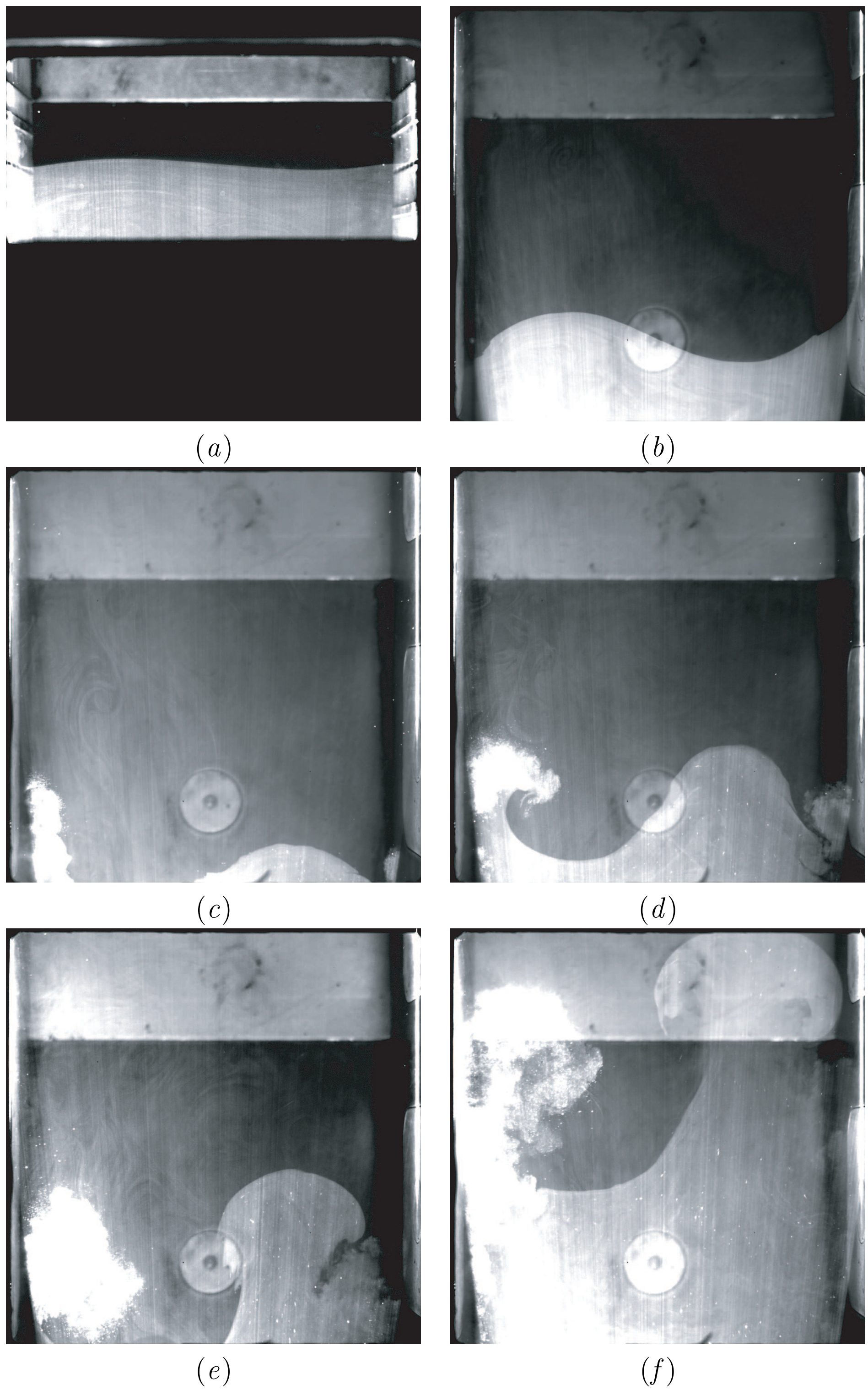

Figure 47: Time-sequence of experimental images for the re-shocked (50% He + 50% Ar)/Ar, M=1.30 interface: (a) t=0.000 ms, (b) t=5.237 ms (0.224 ms before re-shock), (c) t=7.209 ms (1.860 ms after re-shock), (d) t=8.700 ms (3.313 ms after re-shock), (e) t=11.710 ms (6.386 ms after re-shock), and (f) t=15.669 ms (10.122 ms after re-shock, approximately 3 ms after the expansion wave interacts with interface).

(b) is the latest experimental image before the re-shock occurs. This can be considered the re-shock initial condition, which occurs approximately 0.2 ms before re-shock. From Fig. 32, it's clear that the amplitude does not change by much over such short interval. The interface is then re-shocked at the bottom of the last viewing window. According to Fig. 31 (the $x-t$ plot for the (50% He + 50% Ar)/Ar, M=1.30 experimental campaign), the re-shocked interface can be imaged for approximately 7 ms. After this time, the expansion fan interacts with the interface. The re-shocked interface undergoes a phase reversal because the reflected shock wave now travels through the interface from the Ar to the 50% He + 50% Ar, which is called a heavy over light interface configuration. This causes the initial bubble to spike into the lighter, once shocked 50% He + 50% Ar gas. All of the re-shocked images have a turbulent plume originating on the left side of the image. This is residual atomized hydrocarbon vacuum oil that, prior to re-shock, is stationary within the gas flow inlet port. After re-shock, these oil particles turbulently jet into the shock tube flow. This should not be considered part of the re-shock interface. At t=8.700 ms (3.313 ms after re-shock), the interface amplitude is larger than the re-shock initial condition (t=5.237 ms, 0.224 ms before re-shock). This shows that, in 3.313 ms, the interface has gone from the initial amplitude to zero amplitude (due to phase inversion) to a re-shock amplitude that is larger than the initial amplitude which took 5.237 ms to be realized. At t=11.710 ms (6.386 ms after re-shock), a mushroom structure begins to develop at the tip of the spike. Approximately 7 ms after re-shock, the expansion fan interacts with the interface. The last image in Fig. 47 occurs approximately 3 ms after the expansion fan interacts with the re-shocked interface. This interaction causes the interface to be pulled up the tube and stretched out due to a large pressure differential.

Chapter 5

Analysis and Discussion

The experimental data presented in Chapter 4 is analyzed and compared to the numerical simulations performed on the hydrodynamics code *Raptor*. This data is then modeled by one linear and three non-linear models. The data is presented in a non-dimensional format that takes into account the interfacial molecular diffusion. The compressibility effects mentioned in Chapter 4 are discussed in detail and the Reynolds number for each scenario described in Section 4.1 is determined utilizing the initial circulation.

5.1 Compressibility Effects

In Chapter 4, the visualization results for the N_2/SF_6 M=2.05 and 2.86 cases as well as the He/SF_6 M=1.41 and 1.95 cases indicate a flattening of the bubble at late experimental times. This phenomenon is a result of compressibility effects. Jacobs and Sheeley [20] found that after the initial acceleration (due to the incident shock wave) there is a pressure field that is created between the perturbation and the transmitted shock wave. This pressure field (pressure gradient) interacts with the perturbation (density gradient) and results in secondary baroclinic vorticity generation which is a function of the Atwood number.

After the initially planar shock wave traverses the perturbation, the transmitted shock wave becomes deformed due to the shape of the initial perturbation (see Fig. 42

(b)). The shape of the transmitted shock acts like a converging lens beneath the spike and a diverging lens beneath the bubble. This refraction of the transmitted shock wave results in a pressure wave field between the perturbation and transmitted shock wave. If the interface velocity (V_0) is subsonic (M_{tr}<1) compared to the speed of sound in the fluid that is shocked (c_{tr}) by the transmitted shock wave, then acoustic waves create the pressure field. If the interface velocity is supersonic ($M_{tr}\geq1$), shock waves create the pressure field. Table 16 indicates the interface Mach number, M_{tr} (V_0/c_{tr}), for each experimental scenario.

Scenario No.	Gas Pair	M	A	M_{tr}
1	50% He + 50% Ar / Ar	1.30	0.29	0.39
2	50% He + 50% Ar / Ar	1.90	0.29	0.81
3	N_2 / SF_6	1.26	0.64	0.61
4	N_2 / SF_6	2.05	0.68	1.92
5	N_2 / SF_6	2.86	0.68	2.73
6	He / SF_6	1.13	0.95	0.45
7	He / SF_6	1.41	0.95	1.20
8	He / SF_6	1.95	0.95	2.20

Table 16: Interface Mach number derived from one-dimensional gas dynamic equations.

Table 16 shows that the four scenarios that have a $M_{tr}\geq1$ are the same scenarios that are found in Chapter 4 to have a bubble that flattens at late experimental times. This indicates that when shock waves create the pressure field between the perturbation and transmitted shock, the generated secondary vorticity is great enough to influence the bubble in such a manner that the bubble flattens. This would tend to indicate that the secondary vorticity in the bubble region is opposite in sign to the originally deposited vorticity. Experimentally, in the cases where M_{tr}<1 the bubble retained its round shape throughout the entire image sequence, therefore, the deposited secondary vorticity is small compared to the originally deposited vorticity. Thus, when $M_{tr}\geq 1$ the post-shock flow is considered compressible which results in a bubble that flattens as the spike narrows.

5.2 Initial Circulation and Reynolds number

The Richtmyer-Meshkov instability provides a mechanism for mixing two fluids of different density. The flow can either be categorized as laminar or turbulent depending on the Reynolds number of the flow. Dimotakis [14] determined the transition from laminar to turbulent flow to occur at a Reynolds number of 1-2$\times 10^4$ for all types of flow including the Richtmyer-Meshkov instability. The transitional Reynolds number indicates whether or not the initial deposition of vorticity (due to the impulsive acceleration) is sufficient to drive the flow all the way into a turbulent mixing regime [37]. The vortex Reynolds number [17] (Re_Γ) is an appropriate formulation of the Reynolds number when the flow is dominated by vortices (such as the Richtmyer-Meshkov instability), and is given by:

$$Re_\Gamma = \frac{\Gamma_0}{\nu}, \tag{5.1}$$

where Γ_0 is the initial circulation and ν is the kinematic viscosity of the interface given as:

$$\nu = \frac{\mu_1 + \mu_2}{\rho_r + \rho_t}, \tag{5.2}$$

where μ_1 and μ_2 are the dynamic viscosities of the two interface fluids, ρ_r is the density of the light fluid that has been accelerated by the incident shock wave and the reflected shock wave, and ρ_t is the density of the heavy fluid that has been accelerated by the transmitted shock wave. Circulation is defined as the area integral of vorticity (described in Section 1.1.2):

$$\Gamma = \int_A \omega dA, \tag{5.3}$$

where ω is vorticity and A is area. When Stoke's theorem is applied, the circulation is also equal to the integration of velocity (V) along a path (S) that encloses the area A:

$$\Gamma = \oint_S V dS. \tag{5.4}$$

Oakley [37] detailed a formulation of the initial circulation for a sinusoidal perturbation based on Eq. (5.4). The initial circulation is given as:

$$\Gamma_0 = u_t \left(W_r + W_t\right) t - u_2 \left(W_i + W_r\right) t, \tag{5.5}$$

where u_t is the fluid velocity behind the transmitted shock wave, W_r is the reflected shock wave speed, W_t is the transmitted shock wave speed, u_2 is the fluid velocity behind the incident shock wave, W_i is the incident shock wave speed, and t is the shock wave interaction time which is given as:

$$t = \frac{2\eta_0}{W_i}, \tag{5.6}$$

where η_0 is the pre-shock perturbation amplitude.

Table 17 lists the initial circulation, kinematic viscosity, and vortex Reynolds number for each experimental scenario. The table indicates that the magnitude of circulation increases with both Mach and Atwood number. A similar trend is witnessed for the vortex Reynolds number. For each scenario, the vortex Reynolds number was larger than the Dimotakis [14] transitional Reynolds number (1-2$\times 10^4$) indicating that, within the flow, inertial forces dominate viscous forces and turbulent mixing will be observed at the interface.

Scenario No.	Gas Pair	M	Γ_0 (m^2/s)	ν (m^2/s)	Re_Γ
1	50% He + 50% Ar / Ar	1.30	-0.43	1.25×10^{-5}	3.47×10^{4}
2	50% He + 50% Ar / Ar	1.90	-0.81	7.93×10^{-6}	1.02×10^{5}
3	N_2 / SF_6	1.26	-1.60	2.67×10^{-6}	5.99×10^{5}
4	N_2 / SF_6	2.05	-5.55	9.43×10^{-7}	5.89×10^{6}
5	N_2 / SF_6	2.86	-9.85	5.49×10^{-7}	1.79×10^{7}
6	He / SF_6	1.13	-8.75	3.91×10^{-6}	2.24×10^{6}
7	He / SF_6	1.41	-20.56	1.95×10^{-6}	1.05×10^{7}
8	He / SF_6	1.95	-37.26	9.01×10^{-7}	4.13×10^{7}

Table 17: Reynolds number derived from initial circulation and viscosity.

5.3 Dimensionless Parameters

Previous experimental studies have set forth a set of dimensionless parameters to analyze RM data [19], [51]. These dimensionless parameters have been adopted for the current experimental study. The non-dimensional amplitude is given as:

$$\phi = k\left(\eta - \eta_0^1\right), \tag{5.7}$$

where η_0^1 is the initial amplitude immediately after the shock wave traverses the interface. The non-dimensional time τ is:

$$\tau = k\dot{\eta}_0 t, \tag{5.8}$$

where $\dot{\eta}_0$ is the initial growth rate. In experiments where $\dot{\eta}_0$ can not be measured directly, it can be approximated with the impulsive model:

$$\dot{\eta}_0 \approx k\eta_0^1 A^1 V_0. \tag{5.9}$$

Strictly, this approximation is valid only for weak shocks [19], but since $\dot{\eta}_0$ cannot be experimentally determined in the present study, the approximation is used to analyze all of the experimental data. All of the information pertaining to the shock strength and interfacial density difference is contained within the $\dot{\eta}_0$ term, thus making it extremely important in the comparison of data from experiments with different Atwood numbers and shock strengths. The next section will discuss how the $\dot{\eta}_0$ term can be modified to extend its usefulness across the parameter space examined in this experimental study.

5.4 Growth Reduction Factor

Experimental results obtained by Brouillette and Sturtevant [7] indicate that the growth rate of a perturbation subjected to an impulsive acceleration is a function of the interfacial density profile. Moreover, the growth rate decreases as the diffusion thickness increases [7]. Richtmyer's [47] original formulation of the impulsive model in Section 1.1.1 is based on a discontinuous interface. Therefore, a non-dimensional growth reduction factor, ψ, must be introduced to correct the impulsive model for the case of a continuous interface. The corrected initial growth rate is given as:

$$\dot{\eta}_\psi = \frac{\dot{\eta}_0}{\psi}, \tag{5.10}$$

where $\dot{\eta}_0$ is the initial growth rate given by the impulsive model. Since $\dot{\eta}_0$ cannot be reliably measured directly from the experiments in this experimental campaign, the growth reduction factor will play a role in the calculation of non-dimensional time and the evaluation of the analytical models discussed in Section 2.2.

The growth reduction factor is determined by three methods. The first method calculates the growth reduction factor following the process described in Brouillette and Sturtevant [7] which utilizes empirical parameters. Duff *et al.* [16] formulated a linear eigenvalue equation that is independent of the interface's acceleration history [7] in order to determine the velocity of a sinusoidal perturbation. The eigenvalue equation is given as:

$$\frac{d}{dx}\left(\rho\frac{d\dot{\eta}}{dx}\right) = \dot{\eta}k^2\left(\rho - \frac{\psi_E}{\bar{A}k}\frac{d\rho}{dx}\right), \tag{5.11}$$

where $\dot{\eta}$ is the perturbation velocity, k is the wavenumber, ψ_E is the calculated growth reduction factor, $\bar{A}$ is an average of the pre- and post-shock Atwood number, and ρ is the diffusion profile. The diffusion profile, ρ, is given as:

$$\rho(x) = \bar{\rho}\left(1 + \bar{A}\,\mathrm{erf}\left(\frac{x}{\bar{\delta}}\right)\right), \tag{5.12}$$

where $\bar{\rho}$ is an average of the pre- and post-shock density ratio and $\bar{\delta}$ is an average of the pre- and post-shock diffusion thickness. The pre-shock diffusion thickness is the value calculated in Section 4.4.3 and the post-shock diffusion thickness is given as:

$$\delta^1 = \frac{1}{2}\delta\left(\frac{\rho_1^0}{\rho_1^1}\right) + \frac{1}{2}\delta\left(\frac{\rho_2^0}{\rho_2^1}\right), \tag{5.13}$$

where ρ_1^0 and ρ_1^1 are the pre- and post-shock density values for gas 1, and δ is the pre-shock diffusion thickness. The growth reduction factor is obtained by integrating Eq. (5.11) numerically with a finite difference scheme for the density profile given in Eq. (5.12). For each pre-shock Atwood number/Mach number pair, the value of ψ_E is determined by iteration so that the value of $\dot{\eta}$, when integrated from x = -∞ to $x = +\infty$ and from $x = +\infty$ to x = -∞, equals zero at x = -∞ and $x = +\infty$.

The second method for determining the growth reduction factor involves running two *Raptor* numerical simulations for each pre-shock Atwood number/Mach number combination utilizing average parameters from the experimental campaign. The first simulation is run with the minimum allowable diffusion thickness (virtually a discontinuous interface) and the second run utilizes the diffusion thicknesses calculated in Section 4.4.3 (continuous interface). Equation (5.10) is rearranged to solve for ψ. The resulting growth reduction factor, ψ_R, is then given as:

$$\psi_R = \frac{\dot{\eta}_D}{\dot{\eta}_C}, \tag{5.14}$$

where $\dot{\eta}_D$ is the amplitude growth rate for the discontinuous *Raptor* simulation, and $\dot{\eta}_C$ is the amplitude for the continuous *Raptor* simulation.

A third approach to calculating the growth reduction factor involves comparing the amplitude growth rate for the diffuse, continuous *Raptor* simulation to the impulsive model. The impulsive model provides a modeled initial growth rate for a discontinuous interface which acts like the $\dot{\eta}_D$ value in the second approach. The resulting growth reduction factor, ψ_{RI}, is then given as:

$$\psi_{RI} = \frac{\dot{\eta}_0}{\dot{\eta}_C}, \tag{5.15}$$

Table 18 indicates both the calculated growth reduction factor (ψ_E) and the raptor growth reduction factors (ψ_R and ψ_{RI}).

Scenario No.	Gas Pair	M	A	ψ_E	ψ_R	ψ_{RI}
1	50% He + 50% Ar / Ar	1.30	0.29	1.283	1.040	0.981
2	50% He + 50% Ar / Ar	1.90	0.29	1.250	1.006	0.883
3	N_2 / SF_6	1.26	0.64	1.132	1.039	1.223
4	N_2 / SF_6	2.05	0.68	1.079	1.008	1.457
5	N_2 / SF_6	2.86	0.68	1.067	1.024	1.682
6	He / SF_6	1.13	0.95	1.063	1.022	1.262
7	He / SF_6	1.41	0.95	1.047	1.033	1.617
8	He / SF_6	1.95	0.95	1.037	1.020	2.164

Table 18: Calculated and derived growth reduction factors for each Atwood number, Mach number combination.

Table 18 indicates that ψ_E and ψ_R compare well with each other, although ψ_E is consistently larger. The general trend of the ψ values is to decrease for an increase in Atwood number. Within each Atwood number, the ψ value decreases as the Mach number increases due to a greater compression of the post-shock diffusion layer. The ψ_{RI} values for the two (50% He + 50% Ar)/Ar cases are not physically possible, because a ψ value of one corresponds to a discontinuous interface (no diffusion thickness). A characteristic of the current experimental campaign is that the interface must have a finite diffusion thickness. The ψ values less than one are most likely due to the impulsive model not correctly predicting the initial growth. The ψ_{RI} values approach two for the high Atwood and Mach number cases, which indicates that the growth rate should be reduced by half the impulsive model value. It would be expected that the ψ_R value would best collapse the experimental data onto the *Raptor* simulation because, all other things being equal, it quantifies the difference between the numerical simulation with and without a diffusion thickness. Figure 48 is a plot of the non-dimensional time *vs.* amplitude (as outlined in Section 5.3) of the *Raptor* simulation and the experimental data. The experimental non-dimensional time is given as $\tau = k\dot{\eta}_0 t$ where $\dot{\eta}_0$ is given by Eq. (5.10) which allows for the comparison of the three growth reduction factors. The non-dimensional time for *Raptor* is determined by directly measuring the $\dot{\eta}_0$ from the numerical simulation.

Figure 48 indicates that the best agreement between the experimental data and the *Raptor* simulation, for the given set of non-dimensional parameters, is achieved when the experimental initial growth rate is modeled by the impulsive model divided by the *Raptor* growth reduction factor that compares a diffuse interface with the impulsive model (ψ_{RI}). This is expected, since the non-dimensional parameter τ is calculated with the impulsive model. The non-dimensional experimental data presented from this point on will utilize an $\dot{\eta}_0$ value that is reduced by the ψ_{RI} growth reduction factor.

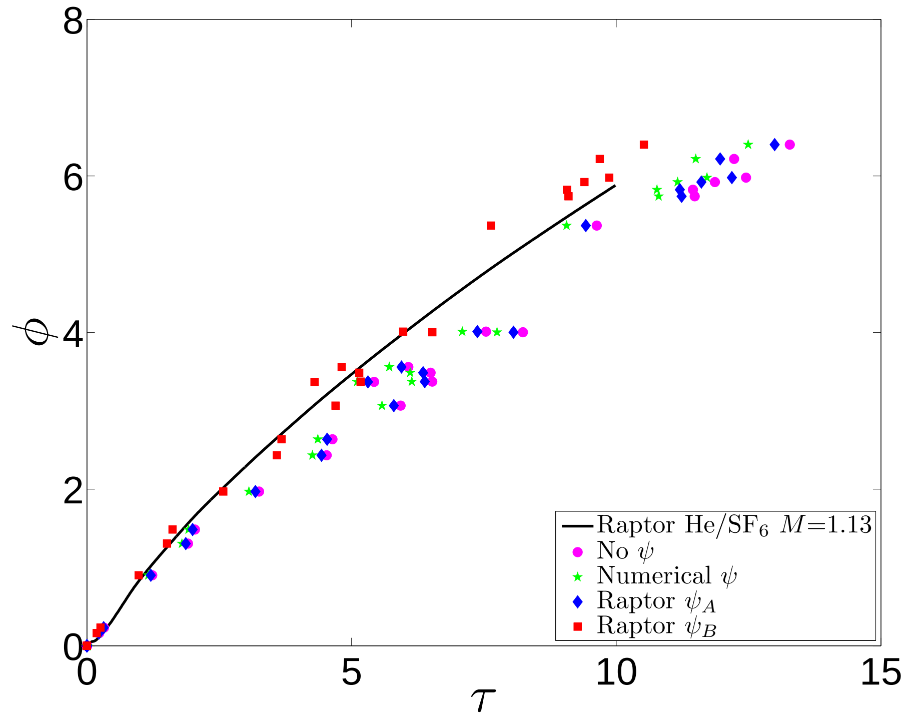

Figure 48: Non-dimensional experimental data compared to *Raptor* simulation for the He/SF$_6$, M=1.13 scenario. Non-dimensional time (τ) is based on several different values of ψ.

5.5 Repeatability

In order to ensure a meaningful data analysis, it is prudent to quantify the degree to which an experimental set is repeatable. A repeatability study is performed for two gas pair/Mach number combinations: (50% He + 50% Ar)/Ar at M=1.90 and N_2/SF_6 at M=2.05. For each case, four consecutive experiments are conducted for the same post-shock timing. The actual timing of the post-shock image varies for each experiment due to slight variations in the initial Mach number. The factor that most affects the repeatability is the amount of time it takes to physically rupture the metal diaphragm. This dictates the initial amplitude and wavelength of the perturbation, which ultimately manifests itself as the final post-shock amplitude. Thus, repeatability is a measure of the scatter of the experimental data points. Figure 49 contains the four (50% He + 50% Ar)/Ar, M=1.90 repeated experiments while Fig. 50 contains the repeated N_2/SF_6, M=2.05 experiments. For each set of images, the left image is the initial condition and the right image is the post-shock image.

The overall amplitude growth for each set of repeated experiments is similar. However, Fig. 50 indicates that for a given post-shock time, the initial amplitude and wavelength play a significant role in the development of the instability. Initial conditions (c) and (e) have a similar waveform that has a slightly smaller initial amplitude and larger wavelength than initial conditions (a) and (g). This directly corresponds to images (d) and (f) being in the early non-linear growth regime, whereas, images (b) and (h) are later in the non-linear growth regime to the point where the tip of the spike is starting to roll-up into a mushroom structure due to the Kelvin-Helmholtz instability. Figure 49 indicates very little difference between the four initial condition images or the

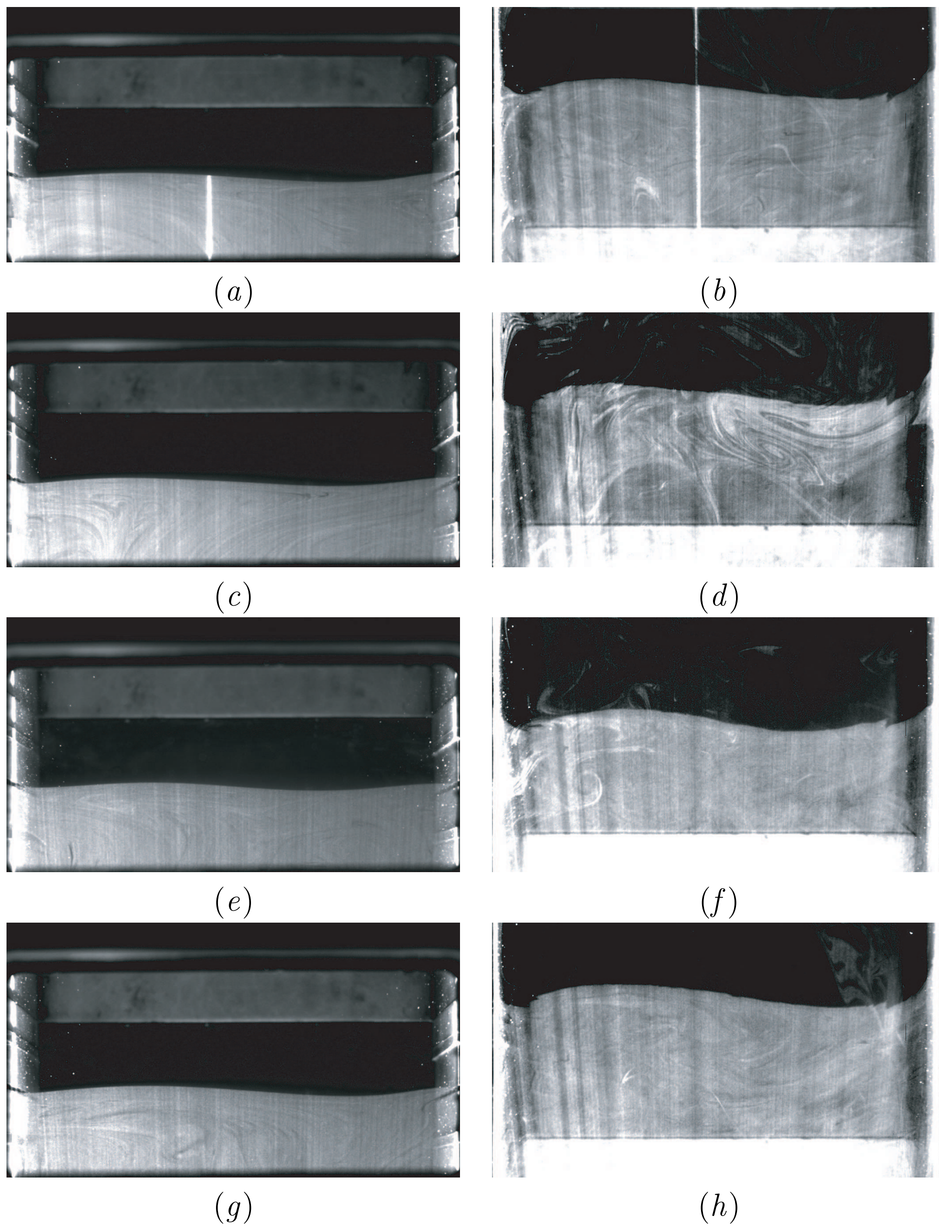

Figure 49: Experimental initial condition/post-shock image pairs for the (50% He + 50% Ar)/Ar, M=1.90 case (repeatability study): (a) Test 477: t=0.000 ms, (b) Test 477: t=1.216 ms, (c) Test 478: t=0.000 ms, (d) Test 478: t=1.220 ms, (e) Test 479: t=0.000 ms, (f) Test 479: t=1.228 ms, (e) Test 480: t=0.000 ms, and (f) Test 480: t=1.214 ms.

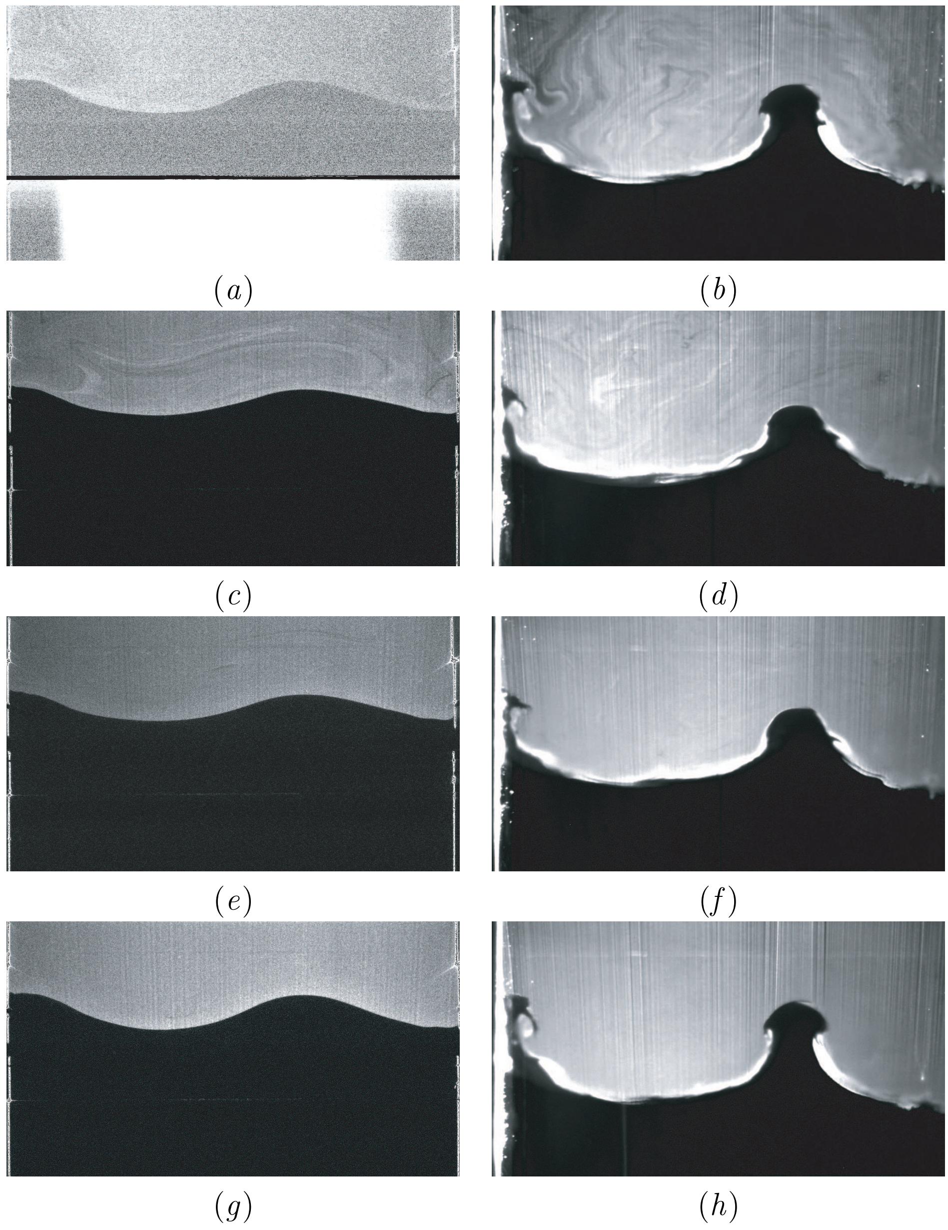

Figure 50: Experimental initial condition/post-shock image pairs for the N_2/SF_6, M=2.05 case (repeatability study): (a) Test 166: t=0.000 ms, (b) Test 166: t=0.789 ms, (c) Test 167: t=0.000 ms, (d) Test 167: t=0.788 ms, (e) Test 168: t=0.000 ms, (f) Test 168: t=0.789 ms, (g) Test 169: t=0.000 ms, and (h) Test 169: t=0.790 ms.

four post-shock images that are all within the linear growth regime. Table 19 indicates the average quantity with standard deviation for the four measured parameters of the repeatability study. Table 20 indicates the standard deviation as a percentage of the averaged measured quantities. The standard deviation is given by Eq. (4.1). For each case, information for individual experiments is obtained from Tables 9 and 11.

Gas Pair	M	η_0^0 (cm)	λ (cm)	t_{PS1} (ms)	η_{PS1} (cm)
50% He + 50% Ar/Ar	1.90	0.25±0.03	20.11±0.88	1.220±0.006	0.63±0.04
N_2/SF_6	2.05	0.84±0.12	17.07±0.67	0.789±0.001	2.48±0.37

Table 19: Average quantities of repeated experiments with standard deviation.

Gas Pair	M	η_0^0	λ	t_{PS1}	η_{PS1}
50% He + 50% Ar/Ar	1.90	12.00%	4.38%	0.492%	6.35%
N_2/SF_6	2.05	14.29%	3.93%	0.127%	14.92%

Table 20: Standard deviation of averaged quantities as a percentage of the averaged quantity.

The results of Tables 19 and 20 indicate that spread of the time data due to variations in the initial Mach strength are very small, with a maximum of approximately 0.5%. The spread of the initial amplitude and wavelength due to variations in the length of time needed to rupture the diaphragm is approximately equal for both gas pair/Mach number combinations. The spread of the post-shock amplitude data is larger (14.92%) for the non-linear N_2/SF_6, M=2.05 case than the linear (50% He + 50% Ar)/Ar, M=1.90 case. It is assumed that the non-linear case represents an upper bound (15%) of the experimental spread for all of the experimental scenarios.

5.6 Uncertainties and Error Propagation

In Section 5.5, an estimate of the experimental data spread was achieved by analyzing four similar experiments. It is also important to understand and estimate the error associated with each measurement, and how the error propagates through derived quantities. The measurement errors associated with this experimental campaign include the length measurements of amplitude and wavelength and the time precision of input and output triggers which dictate the time at which an image is obtained. The propagation of error for a function $F = f(x, y, z, ...)$, with independent variables x, y, z, etc., proceeds from the total differential of F:

$$dF = \left(\frac{\partial f}{\partial x}\right) dx + \left(\frac{\partial f}{\partial y}\right) dy + \left(\frac{\partial f}{\partial z}\right) dz + ... \tag{5.16}$$

The quantities dx, dy, dz, ... represent the uncertainty for the the variables x, y, z, ..., and are renamed $dx = \delta x$, $dy = \delta y$, etc. The total standard deviation (error) of F is then given as:

$$\delta F^2 = \left(\frac{\partial f}{\partial x}\right)^2 \delta x^2 + \left(\frac{\partial f}{\partial y}\right)^2 \delta y^2 + \left(\frac{\partial f}{\partial z}\right)^2 \delta z^2 + ... \tag{5.17}$$

The error associated with measuring the amplitude and wavelength of a perturbation results from the uncertainty of determining the 50% pixel intensity (analogous to concentration) location (discussed in Section 4.2) of the interface in several locations along the interface. In each case, the desired length is derived by subtracting one 50% pixel intensity location from another. The uncertainty of each 50% pixel intensity location measurement is estimated to be ± 1 pixel (in most cases 1 pixel equals 0.0254 cm). Utilizing Eq. (5.17), the error for each length measurement is 0.0359 cm. Due to the high speed PCI-6110E data acquisition computer card, the error for each time measurement is ± 0.001 ms.

Experimental data is presented in a non-dimensional form discussed in Section 5.3. The error propagation formulas for the non-dimensional parameters are derived from Eq. (5.17), and are given as:

$$\delta\phi = \sqrt{\left(\frac{\partial\phi}{\partial k}\right)^2 \delta k^2 + \left(\frac{\partial\phi}{\partial(\eta-\eta_0^1)}\right)^2 \delta(\eta-\eta_0^1)^2}, \tag{5.18}$$

and

$$\delta\tau = \sqrt{\left(\frac{\partial\tau}{\partial k}\right)^2 \delta k^2 + \left(\frac{\partial\tau}{\partial\eta_0^1}\right)^2 \delta\eta_0^{1\,2} + \left(\frac{\partial\tau}{\partial V_0}\right)^2 \delta V_0^2 + \left(\frac{\partial\tau}{\partial t}\right)^2 \delta t^2 + \left(\frac{\partial\tau}{\partial A^1}\right)^2 \delta A^{1\,2}}, \tag{5.19}$$

where $\delta\eta_0^1$=0.0359 cm, δt=0.00001 s, and $\delta V_0 = LV_0$ where the constant L is determined from the error analysis of deriving the initial wave speed from two consecutive pressure transducers. The uncertainty of the wavenumber, k, is given as:

$$\delta k = \sqrt{\left(\frac{\partial k}{\partial\lambda}\right)^2 \delta\lambda^2}, \tag{5.20}$$

where $\delta\lambda$=0.0359 cm. The uncertainty of the Atwood number is given as:

$$\delta A = \sqrt{\left(\frac{\partial A}{\partial\rho_1}\right)^2 \delta\rho_1^2 + \left(\frac{\partial A}{\partial\rho_2}\right)^2 \delta\rho_2^2}, \tag{5.21}$$

where ρ_x is given as P/R_xT, and the associated uncertainty is defined as:

$$\delta\rho_x = \sqrt{\left(\frac{\partial\rho_x}{\partial P}\right)^2 \delta P^2 +, \left(\frac{\partial\rho_x}{\partial R_x}\right)^2 \delta R_x^2 + \left(\frac{\partial\rho_x}{\partial T}\right)^2 \delta T^2}, \tag{5.22}$$

where P=98274 Pa, δP=2948 Pa (3% of P), T=300 K, δT=9 K (3% of T), and R_x is defined as $\mathcal{R}/MW_x$ where $\mathcal{R}$ is the universal gas constant (8314 J/(kg mol K)) and MW_x is the molecular weight of a given gas. The uncertainty of R_x is then given as:

$$\delta R_x = \sqrt{\left(\frac{\partial R_x}{\partial MW_x}\right)^2 \delta MW_x^2}, \tag{5.23}$$

where δMW_x=0.001.

Table 21 lists the non-dimensional time and amplitude along with the uncertainty calculated with Eq. (5.18) and (5.19) for a single experiment in each experimental scenario. The $\delta\phi$ values are fairly consistent across all of the scenarios, whereas the $\delta\tau$ values are not constant. This is expected since the value of $\delta\tau$ is proportional to the experimental post-shock image time. The (50% He + 50% Ar)/Ar $\delta\tau$ values are smaller than the other $\delta\tau$ values because their τ values are smaller.

Gas Pair	M	τ	$\delta\tau$	ϕ	$\delta\phi$
50% He + 50% Ar / Ar	1.30	0.18	0.03	0.16	0.02
50% He + 50% Ar / Ar	1.90	0.18	0.05	0.16	0.02
N_2 / SF_6	1.26	2.95	0.18	1.72	0.03
N_2 / SF_6	2.05	3.03	0.21	1.89	0.02
N_2 / SF_6	2.86	2.28	0.16	1.69	0.02
He / SF_6	1.13	3.59	0.08	2.43	0.02
He / SF_6	1.41	3.06	0.09	2.08	0.02
He / SF_6	1.95	3.34	0.10	2.53	0.02

Table 21: Non-dimensional time and amplitude with associated uncertainty for one experiment in each experimental scenario.

The uncertainty for a specific data point in Table 21 can be broken down into its individual components. For the (50% He + 50% Ar)/Ar, M=1.90 case, $\delta\tau$=0.05. The $\left(\frac{\partial\tau}{\partial\eta_0^1}\right)^2 \delta{\eta_0^1}^2$ term (from Eq. (5.19)) contributes approximately 87% of the uncertainty, while the $\left(\frac{\partial\tau}{\partial A^1}\right)^2 \delta{A^1}^2$ term contributes approximately 13%, and the remaining terms are negligible. The $\delta\phi$ value is 0.02, and the $\left(\frac{\partial\phi}{\partial(\eta-\eta_0^1)}\right)^2 \delta(\eta-\eta_0^1)^2$ term (from Eq. (5.18)) contributes nearly 100% of the uncertainty.

5.7 Growth Rate Data

Amplitude growth rates for the experimental scenarios described in Section 4.1 are presented in a dimensional form (η (cm) *vs.* t (ms)) as well as the non-dimensional form discussed in Section 5.3 (ϕ *vs.* τ).

5.7.1 Growth Rate Data: Dimensional

The dimensional amplitude growth rate for each experimental scenario is presented in the form of amplitude *vs.* time (η (cm) *vs.* t (ms)). Figure 51 is a plot of all the experimental scenarios. Figure 52 is a plot of the two (50% He + 50% Ar)/Ar scenarios compared to the results of the corresponding *Raptor* numerical simulations. Figures 53 and 54 present the dimensional experimental data compared to *Raptor* for the three N_2/SF_6 scenarios and the three He/SF_6 scenarios respectfully.

Figure 51 clearly shows that if the Atwood number (gas pair) is held constant, the amplitude growth rate increases as the Mach number is increased. For a relatively constant Mach number (for instance (50% He + 50% Ar)/Ar (M=1.90), N_2/SF_6 (M=2.05), and He/SF_6 (M=1.95)) the amplitude growth rate increases as the Atwood number increases, although this effect is harder to quantify from Fig. 51 because the initial amplitude of the (50% He + 50% Ar)/Ar cases is quite smaller than the other two gas pairs. All of the experimental data appears to fit within the 15% scatter prediction determined in Section 5.5 except the N_2/SF_6, M=1.26 case. The reason for the large data scatter in this scenario is that the post-shock flow is visualized with laser sheets that enter the side of the shock tube instead of the bottom. This results in a small viewing area, which means that the times at which images can be acquired is restricted. The solution is to hold the post-shock time constant and vary the initial amplitude instead of attempting to hold the initial amplitude constant while varying the post-shock time.

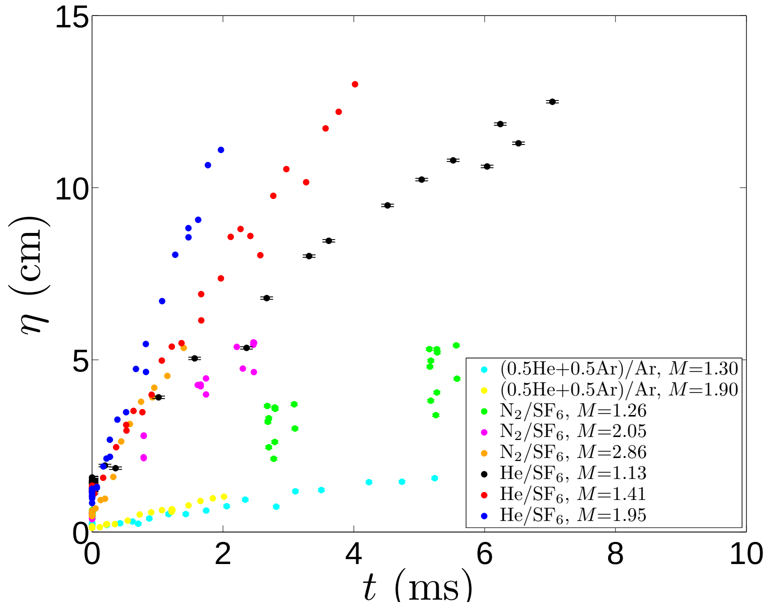

Figure 51: Dimensional plot of amplitude (cm) *vs.* time (ms) for every experimental scenario.

Figures 52, 53, and 54 show that, in general, the single mode *Raptor* simulations (described in Section 3.5) simulate the experimental data very well. This indicates that the final conclusion of Section 4.4.2, that the interface is a predominately single-moded one, is valid. The three figures show that *Raptor* best follows the experimental data for the (50% He + 50% Ar)/Ar (M=1.30), N_2/SF_6 (M=2.86), and He/SF_6 (M=1.13) cases. In all other cases, *Raptor* tends to overpredict the experimental growth rate.

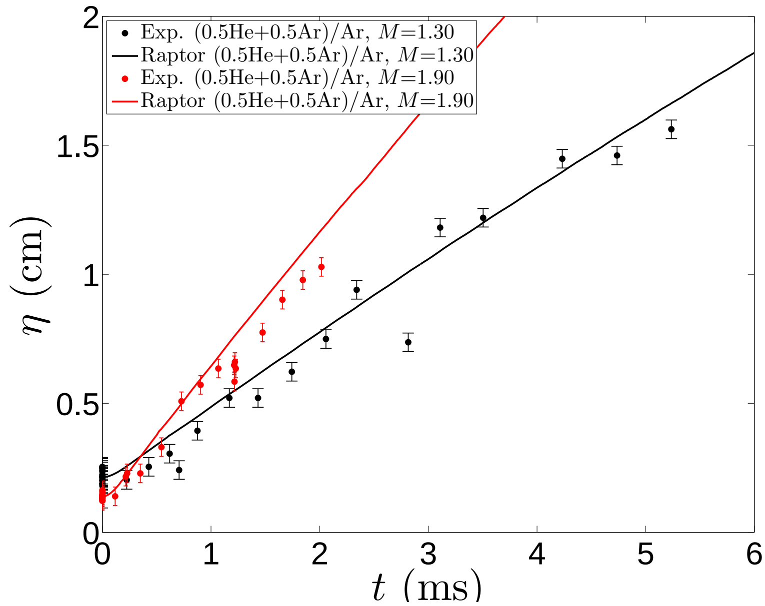

Figure 52: Plot of amplitude (cm) *vs.* time (ms) for the (50% He + 50% Ar)/Ar gas pair.

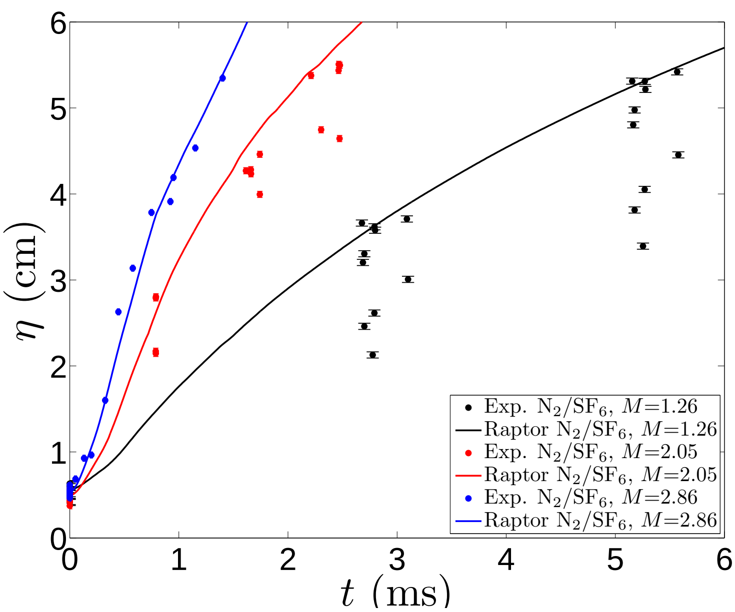

Figure 53: Plot of amplitude (cm) *vs.* time (ms) for the N_2/SF_6 gas pair.

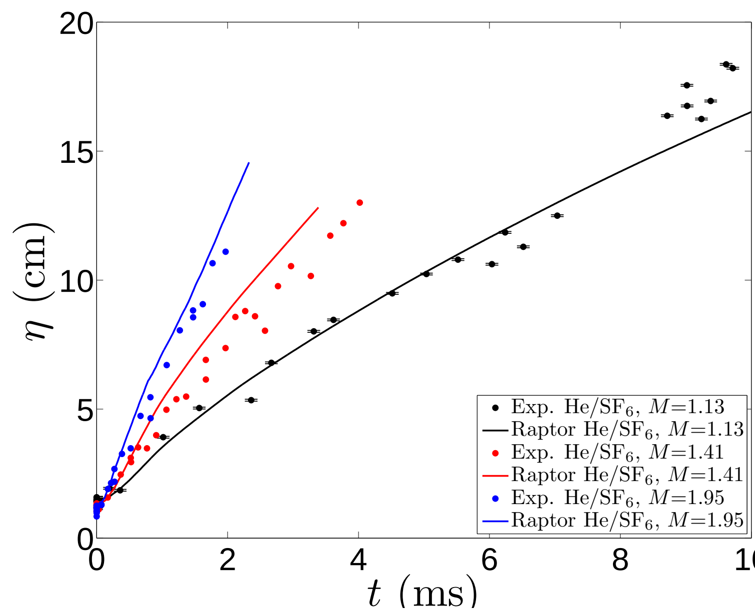

Figure 54: Plot of amplitude (cm) *vs.* time (ms) for the He/SF$_6$ gas pair.

5.7.2 Growth Rate Data: Non-Dimensional

The non-dimensional amplitude growth rate for each experimental scenario is presented in the form of a non-dimensional amplitude vs. time (ϕ vs. τ) as described in Section 5.3. Figure 55 is a plot of all the experimental scenarios. All of the plots in Figures 56, 57, and 58 contain the non-dimensional experimental and *Raptor* simulation data. Each of the four plots within each figure corresponds to a different model. In each case, plot (a) is the impulsive model, (b) the Sadot *et al.* model, (c) the Mikaelian model, and (d) the Dimonte & Schneider model. In each of these plots, a horizontal error bar is introduced due to the non-dimensional time, τ, being a multiplication of five parameters (see Eq. (5.8) and (5.9)) that each have a finite measurable error. The error propagation expression is given in Eq. (5.19).

One of the ultimate goals of the present research is to utilize the parameter study to determine if specific non-dimensional scaling laws collapse all of the Richtmyer-Meshkov experimental data onto a single line. Figure 55 indicates that the non-dimensional parameters utilized in the present study collapse the data very well for a non-dimensional time of $\tau \leq 4$. To a certain extent, this should be expected at low τ values because the initial growth rate of all the experimental data is approximated by the linear, impulsive model and the data is then scaled by this initial growth rate. The impulsive model produces a straight line and therefore, will collapse to a single line when scaled by itself. When $4 < \tau < 6$ the non-dimensional parameters collapse the data, however there is much more scatter in the collapse. For $\tau \geq 6$ there is insufficient data to determine how well the non-dimensional parameters collapse the data.

Figure 56 shows that the non-dimensional *Raptor* growth rate is slightly greater than the experimental data for the (50% He + 50% Ar)/Ar scenarios. However, the two experimental data sets collapse well onto each other as well as the *Raptor* simulations. The impulsive model predicts the growth for the early times well because the interface is in the linear regime for most of the experimental time, but *Raptor* and the impulsive model (a) deviate at later non-dimensional times because the interface progresses into the non-linear regime. Both the Sadot *et al.* (b) and Mikaelian (c) models predict the growth of the experimental data well and the transition to the non-linear regime, however, they both slightly underpredict the *Raptor* simulations at late non-dimensional times. The Dimonte & Schneider (d) model grossly underpredicts the experimental and numerical data. This indicates that the experimentally determined θ_b value presented by Dimonte & Schneider is not valid for a predominantly single moded interface. The data seems to suggest that the θ values must be larger in order for the model to correctly predict the experimental and numerical data.

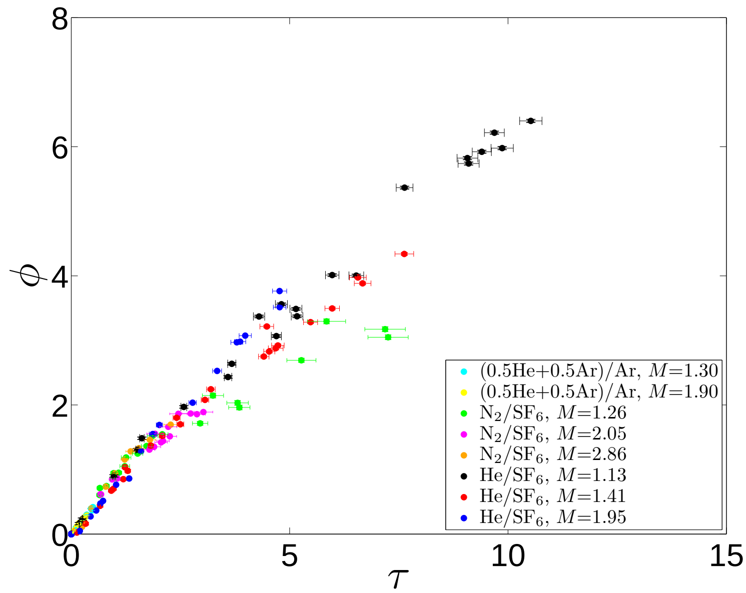

Figure 55: Non-dimensional plot of amplitude *vs.* time for every experimental scenario.

Figure 57 shows the non-dimensional experimental data and *Raptor* simulations for the N_2/SF_6 experimental campaigns. The experimental and *Raptor* data both collapse well onto each other for $\tau<2$. After this point the different M experimental data collapse well onto one another and the *Raptor* data collapse well onto itself, however the *Raptor* data has a slightly greater growth rate than the experiment for all M. The impulsive model (a) predicts the data for non-dimensional times approximately less than 1 while the interface is in the linear regime. The Sadot *et al.* (b) model predicts the data well for $\tau\leq 2$, and then afterwards slightly overpredicts the data. The Mikaelian (c) model also predicts the data well for $\tau\leq 2$, but then afterwards slightly underpredicts the data. In each case the curvature of the model in the non-linear regime is similar to the data. The Dimonte & Schneider (d) model underpredicts the data in the linear and non-linear regime.

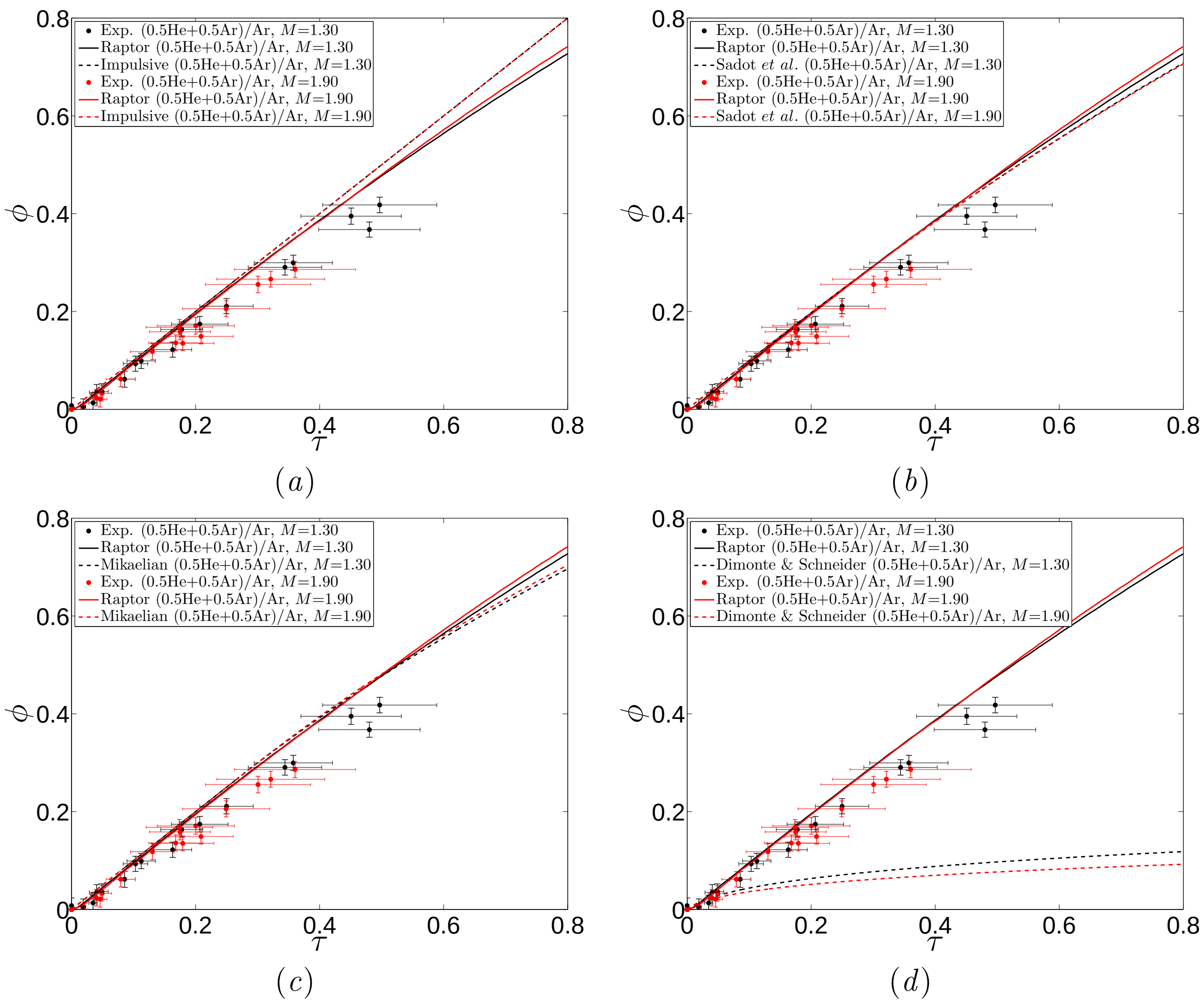

Figure 56: Non-dimensional plot of amplitude *vs*. time for the (50% He + 50% Ar)/Ar gas pair. Experiments and *Raptor* are compared to four models: (a) impulsive, (b) Sadot *et al.*, (c) Mikaelian, and (d) Dimonte & Schneider.

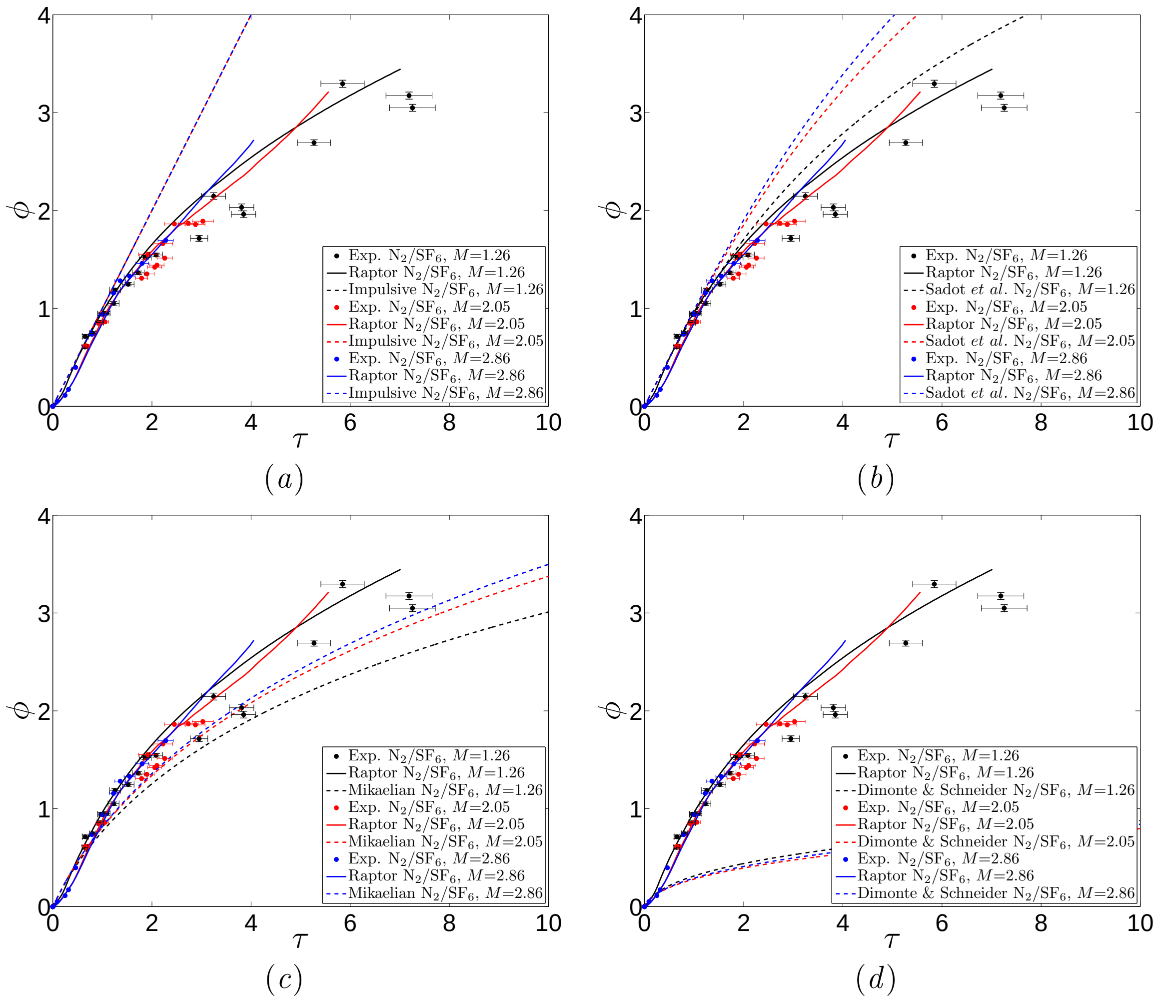

Figure 57: Non-dimensional plot of amplitude *vs.* time for the N_2/SF_6 gas pair. Experiments and *Raptor* are compared to four models: (a) impulsive, (b) Sadot *et al.*, (c) Mikaelian, and (d) Dimonte & Schneider.

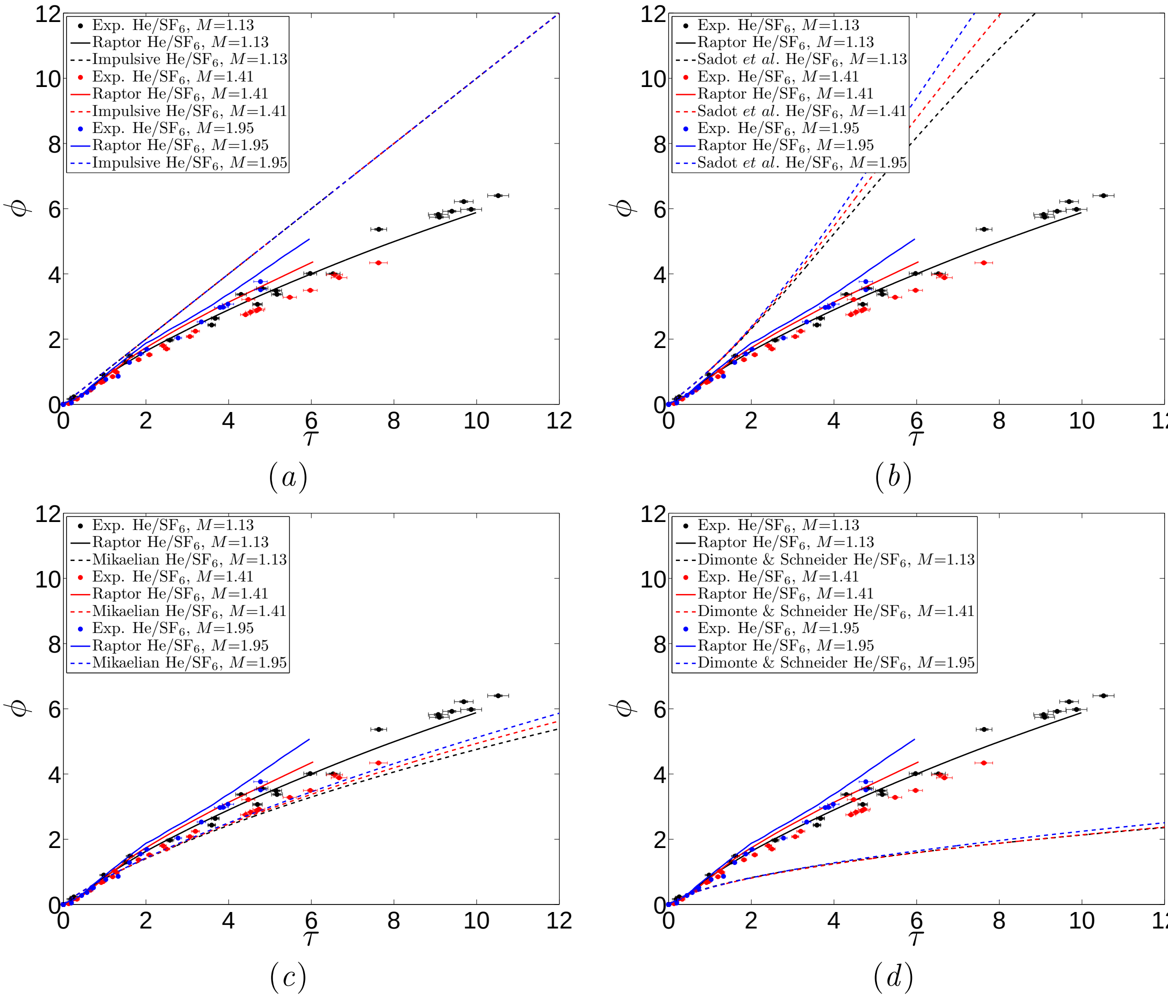

Figure 58: Non-dimensional plot of amplitude *vs.* time for the He/SF$_6$ gas pair. Experiments and *Raptor* are compared to four models: (a) impulsive, (b) Sadot *et al.*, (c) Mikaelian, and (d) Dimonte & Schneider.

Figure 58 shows the non-dimensional experimental data and *Raptor* simulations for the He/SF_6 experimental campaigns. The experimental and *Raptor* data both collapse well onto each other for $\tau<4$. The non-dimensional experimental data shows some scatter for $\tau>4$, while the *Raptor* simulations also diverge. However, the experimental data and the *Raptor* simulations collapse fairly well at late non-dimensional times. The impulsive model (a) predicts the data for $\tau<2$ when the instability development remains in the linear regime. The Sadot *et al.* (b) model diverges from the data at $\tau\approx1$. This is because the model does not correctly capture the non-linear regime for $A\gtrsim0.9$ [51]. The Mikaelian (c) model predicts the data well for $\tau\leq2$, and then afterwards slightly underpredicts the data. Lastly, the Dimonte & Schneider (d) model underpredicts the experimental and computational data.

Chapter 6

Conclusions and Future Work

An experimental parameter study of the Richtmyer-Meshkov instability has been conducted for a membraneless, two dimensional, predominately single mode gas interface. The parameter study contains eight scenarios encompassing a wide range of Atwood numbers, $(0.29 < A < 0.95)$, and shock strengths, $(1.1 < M < 3)$ which greatly increase the size of the experimental Richtmyer-Meshkov instability database. The importance of this data is that it can be used as a test matrix to evaluate various hydrodynamic computer codes and analytical models. The current study is the first to investigate the Richtmyer-Meshkov instability for a He/SF_6 interface which has an Atwood number approaching unity. These results will be of great interest to the Inertial Confinement Fusion community which designs fusion fuel pellets that may have an Atwood number approaching one [4]. The current study is also the first to conduct membraneless experiments for a Mach number approximately equal to, and greater than, M=2. This feat is accomplished for each investigated gas pair.

The initial condition characterization results indicate that the current experimental apparatus is adequate for creating membraneless, two dimensional, predominantly single mode interfaces. A three-dimensional reconstruction study shows that the interface is mostly two-dimensional within the middle half of the shock tube, which is considered the region of interest. A Fourier analysis is performed on a set of experimental initial condition images. This analysis indicates that the initial perturbation has a single dominant mode, however approximately 5-7 additional modes exist which have a non-zero amplitude. The measured diffusion thickness is determined to be that of the fluid seeding material and not the molecular diffusion thickness of the interface gases.

Visualization results indicate that the qualitative shape of the instability is dependent on the interfacial Atwood number. Due to the small Atwood number associated with the (50% He + 50% Ar)/Ar interface, the overall growth of the perturbation is minimal over the entire experimental time. The characteristic mushroom roll-up structure is observed for the N_2/SF_6 scenarios. In addition, secondary instabilities are witnessed on the side of the mushroom structure. For the He/SF_6 scenarios a mushroom structure is observed but the mushroom sides extend outward instead of rolling up. This is due to the light helium not having enough momentum to roll-up the heavy SF_6 which results in the SF_6 flowing down the side of the mushroom. The spike is observed bending and eventually the tip disconnects from the spike. At late times the heavy fluid within the spike shaft and tip as well as the mushroom structure are observed mixing turbulently with the light gas.

Compressibility effects play a significant role in the generation of secondary baroclinic vorticity which cause the bubble to flatten while the spike narrows. In each of the four experimental scenarios where a flattened bubble is observed, $M_{tr}\geq 1$ where M_{tr} is the Mach number of the interface with respect to the sound speed in the gas that is shocked by the transmitted shock wave. When $M_{tr}<1$, the bubble retains its curved shape throughout the entire time sequence of images.

The amplitude growth rate of the experimental data is compared to the hydrodynamic computer code *Raptor* and several analytical models. The single mode *Raptor* simulations predict the experimental amplitude very well. This provides further evidence that the initial perturbation is predominantly single moded and that the other small amplitude modes have little effect on the growth of the perturbation. The Mikaelian model consistently predicts the experimental and *Raptor* amplitude growth rate better than the other evaluated models. This could be because the model is created for a single mode interface and utilizes separate equations for the linear and non-linear regimes. The non-dimensional parameters used to scale the experimental data do not constitute a fully universal scaling law, however they do collapse the data well for early to moderate non-dimensional times.

The most logical next step for future work would involve a comprehensive study of a re-shocked interface. Initial experiments presented in Section 4.6 show that a full scale re-shock campaign could be conducted if the modular shock tube is rearranged to ensure that the entire re-shock sequence is viewable within a window. In addition to re-shock, the once shocked interface could be examined at later times within the non-linear growth regime if the interface section is located closer to the top of the shock tube.

The current study has been concerned with measuring perturbation amplitude and thus gaining knowledge of the amplitude growth rate. Future work could focus on the utilization of a diverse set of visualization methods in order to determine molecular density variations and small scale velocity measurements which would allow for direct vorticity and turbulence measurements.

Bibliography

[1] U. Alon, J. Hecht, D. Mukamel, and D. Shvarts, *Scale invariant mixing rates of hydrodynamically unstable interfaces*, Phys. Rev. Let. 72 (1994), pp. 2867–2870.

[2] U. Alon, J. Hecht, D. Ofer, and D. Shvarts, *Power laws and similarity of Rayleigh-Taylor and Richtmyer-Meshkov mixing fronts at all density ratios*, Phys. Rev. Let. 74 (1995), pp. 534–537.

[3] M. H. Anderson, B. P. Puranik, J. G. Oakley, P. W. Brooks, and R. Bonazza, *Shock tube investigation of hydrodynamic issues related to inertial confinement fusion*, Shock Waves, 10 (2000), p. 377.

[4] R. Betti, R. McCrory, and C. Verdon, *Stability analysis of unsteady ablation fronts*, Phys. Rev. Let. 71 (1993), pp. 3131–3134.

[5] J. Birks, *Excimers*, Rep. Prog. Phys. 38 (1975), pp. 903–974.

[6] M. Brouillette, *The Richtmyer-Meshkov instablity*, Annu. Rev. Fluid Mech. 34 (2002), pp. 445–468.

[7] M. Brouillette and B. Sturtevant, *Experiments on the Richtmyer-Meshkov instability: single-scale perturbations on a continuous interface*, J. Fluid Mech. 263 (1994), pp. 271–292.

[8] J. M. Budzinski, R. F. Benjamin, and J. W. Jacobs, *Influence of initial conditions on the flow patterns of a shock-accelerated thin fluid layer*, Phys. Fluids, 6 (1994), pp. 3510–3512.

[9] P. Colella, *A direct Eulerian MUSCL scheme for gas dynamics*, SIAM J. Sci. Stat. Comput., 6 (1985), pp. 104–117.

[10] B. Collins and J. Jacobs, *PLIF flow visualization and measurements of the Richtmyer-Meshkov instability of an air/SF_6 interface*, J. Fluid Mech. 464 (2002), pp. 113–136.

[11] G. Dimonte, C. E. Frerking, M. Schneider, and B. Remington, *Richtmyer-Meshkov instability with strong radiatively driven shocks*, Phys. Plasmas, 3 (1996), pp. 614–630.

[12] G. Dimonte and B. A. Remington, *Richtmyer-Meshkov experiments on the Nova laser at high compression*, Phys. Rev. Let. 70 (1993), pp. 1806–1809.

[13] G. Dimonte and M. Schneider, *Density ratio dependence of Rayleigh-Taylor mixing for sustained and impulsive acceleration histories*, Phys. Fluids, 12 (2000), pp. 304–320.

[14] P. Dimotakis, *Turbulent mixing*, Annu. Rev. Fluid Mech. 37 (2005), pp. 329–356.

[15] R. Drake, *Hydrodynamic instabilities in astrophysics and in laboratory high-energy-density systems*, Plasma Phys. Control. Fusion, 47 (2005), pp. 419–440.

[16] R. Duff, F. Harlow, and C. Hirt, *Effects of diffusion on interface instabiliy between gases*, Phys. Fluids, 15 (1962), pp. 753–759.

[17] A. Glezer, *The formation of vortex rings*, Phys. Fluids, 31 (1988), pp. 3532–3542.

[18] R. L. Holmes, G. Dimonte, B. Fryxell, M. L. Gittings, J. W. Grove, M. Schneider, D. H. Sharp, A. L. Velikovich, R. P. Weaver, and Q. Zhang, *Richtmyer-Meshkov instability growth: experiment, simulation and theory*, J. Fluid Mech. 389 (1999), pp. 55–79.

[19] J. Jacobs and V. Krivets, *Experiments on the late-time development of single-mode Richtmyer-Meshkov instability*, Phys. Fluids, 17 (2005), pp. 034105–1 – 034105–10.

[20] J. Jacobs and J. Sheeley, *Experimental study of incompressible Richtmyer-Meshkov instability*, Phys. Fluids, 8 (1996), pp. 405–415.

[21] J. W. Jacobs, D. G. Jenkins, D. L. Klein, and R. F. Benjamin, *Experimental study of instability growth patterns of a shock-accelerated, thin fluid layer*, Proc. 4th Intl. Workshop on the Physics of Compressible Turbulent Mixing, (1993), pp. 223–229. Cambridge.

[22] ——, *Nonlinear growth of the shock-accelerated instability of a thin fluid layer*, J. Fluid Mech. 295 (1995), pp. 23–42.

[23] J. W. Jacobs, D. Klein, D. Jenkins, and R. Benjamin, *Instability growth patterns of a shock-accelerated thin fluid layer*, Phys. Rev. Let. 70 (1993), pp. 583–586.

[24] M. Jones and J. Jacobs, *A membraneless experiment for the study of Richtmyer-Meshkov instability of a shock-accelerated gas interface*, Phys. Fluids, 9 (1997), pp. 3078–3085.

[25] B. Jun, T. Jones, and M. Norman, *Interaction of Rayleigh-Taylor fingers and circumstellar cloudlets in young supernova remnants*, Astrophysical Journal, 468 (1996), pp. 59–63.

[26] R. Klein, *The interaction of supernova remnants with interstellar clouds: experiments on the Nova laser*, Astrophysical Journal, 583 (2003), pp. 245–259.

[27] D. Layzer, *On the instability of superposed fluids in a gravitational field*, Astrophysical Journal, 122 (1955), pp. 1–12.

[28] J. Lighthill, *Waves in fluids*, Cambridge University Press, United Kingdom, 1st ed., 1978.

[29] J. Lindl, *Development of the indirect-drive approach to inertial confinement fusion and the target physics basis for ignition and gain*, Phys. Plasmas, 2 (1995), pp. 3933–4024.

[30] A. Lozano, B. Yip, and R. Hanson, *Aceton: a tracer for concentration measurements in gaseous flows by planar laser-induced fluorescence*, Experiments in Fluids, 13 (1992), pp. 369–376.

[31] F. Marble, G. Hendricks, and E. Zukoski, *Progress toward shock enhancement and control of supersonic combustion processes*, in 23th AIAA, SAE, ASME, and ASEE Joint Propulsion Conference, San Diego, CA, June 29 - July 2, 1987.

[32] P. Meekunnasombat, J. G. Oakley, M. H. Anderson, and R. Bonazza, *Experimental study of shock-accelerated liquid layers*, Shock Waves, 15 (2006), pp. 383–397.

[33] Y. Y. Meshkov, *Instability of a shock wave accelerated interface between two gases*, NASA Technical Translation, NASA TT F-13,074 (1970).

[34] K. A. Meyer and P. J. Blewett, *Numerical investigation of the stability of a shock-accelerated interface between two fluids*, Phys. Fluids, 15 (1972), pp. 753–759.

[35] K. Mikaelian, *Analytic approach to nonlinear Rayleigh-Taylor and Richtmyer-Meshkov instabilities*, Phys. Rev. Let. 80 (2003), pp. 508–511.

[36] ——, *Explicit expressions for the evolution of single-mode Rayleigh-Taylor and Richtmyer-Meshkov instabilities at arbitrary Atwood numbers*, Phys. Rev. E, 67 (2003), pp. 026319–1 – 026319–7.

[37] J. Oakley and R. Bonazza, *Circulation model, phase reversal, and vorticity cancellation for compressible gas interfaces*, Phys. Rev. E, In review (2008).

[38] J. G. Oakley, *Experimental study of shocked gas interfaces with visualized initial conditions*, PhD thesis, University of Wisconsin - Madison, Madison, WI, 2001.

[39] J. Ongena and G. V. Oost, *Energy for future centuries. will fusion be an inexhaustible, safe and clean energy source?*, Trans. Fusion Sci. Technol. 41 (2002), pp. 3–14.

[40] P. B. Puranik, J. G. Oakley, M. H. Anderson, and R. Bonazza, *Experimental study of the Richtmyer-Meshkov instability induced by a Mach 3 shock wave*, Shock Waves, 13 (2004), p. 413.

[41] D. Ranjan, M. Anderson, J. Oakley, and R. Bonazza, *Experimental investigation of a strongly shocked gas bubble*, Phys. Rev. Let. 94 (2005), pp. 184507–1 – 184507–4.

[42] D. Ranjan, J. Niederhaus, B. Motl, M. Anderson, J. Oakley, and R. Bonazza, *Experimental investigation of primary and secondary features in high-mach-number shock-bubble interaction*, Phys. Rev. Let. 98 (2007), p. 024502.

[43] L. Rayleigh, *Investigation of the character of the equilibrium of an incompressible heavy fluid of variable density*, Scientific Papers, V. II, (1964), pp. 200–207. Dover Pub., NY, reprinted the 1900 papers.

[44] R. Reid, J. Prausnitz, and B. Poling, *Properties of gases and liquids*, McGraw-Hill, New York, 4rd ed., 1987.

[45] B. A. Remington, S. W. Haan, S. G. Glendinning, J. D. Kilkenny, D. H. Munro, and R. J. Wallace, *Large growth Rayleigh-Taylor experiments using shaped laser pulses*, Phys. Rev. Let. 67 (1991), pp. 3259–3262.

[46] B. A. Remington, S. V. Weber, M. M. Marinak, S. W. Haan, J. D. Kilkenny, R. Wallace, and G. Dimonte, *Multimode Rayleigh-Taylor experiments on Nova*, Phys. Rev. Let. 73 (1994), pp. 545–548.

[47] R. D. Richtmyer, *Taylor instability in shock accleration of compressible fluids*, Commun. Pure Appl. Math., 13 (1960), pp. 297–319.

[48] P. Rightley, P. Vorobieff, R. Benjamin, and R. Martin, *Experimental observation of the mixing transition in a shock-accelerated gas curtain*, Phys. Fluids, 11 (1999), pp. 186–200.

[49] P. M. Rightley, P. Vorobieff, and R. F. Benjamin, *Evolution of a shock-accelerated thin fluid*, Phys. Fluids, 9 (1997), pp. 1770–1782.

[50] K. V. Riper, *Stellar core collapse: II. Inner core bounce and shock propagation*, Astrophysical Journal, 257 (1982), pp. 793–820.

[51] O. Sadot, L. Erez, U. Alon, D. Oron, L. Levin, G. Erez, G. Ben-Dor, and D. Shvarts, *Study of nonlinear evolution of single-mode and two-bubble interaction under Richtmyer-Meshkov instability*, Phys. Rev. Let. 80 (1998), pp. 1654–1657.

[52] J. Seitzman and R. Hanson, *Instrumentation for flows with combustion. Chapter 6: Planar fluorescence imaging in gases*, Acedemic Press Inc., San Diego, 1st ed., 1993.

[53] L. Smarr, J. Wilson, R. Barton, and R. Bowers, *Rayleigh-Taylor overturn in supernova core collapse*, Astrophysical Journal, 246 (1981), pp. 515–525.

[54] J. Stone, J. Xu, and L. Mundy, *Formation of 'bullets' by hydrodynamical instabilities in stellar outflows*, Nature, 377 (1995), pp. 315–317.

[55] G. I. Taylor, *The instability of liquid surfaces when accelerated in a direction perpendicular to their planes*, I. Proc. R. Soc. A (1950), pp. 192–196.

[56] M. Thurber, F. Grisch, B. Kirby, M. Votsmeier, and R. Hanson, *Measurements and modeling of acetone laser-induced fluorescence with implications for temperature-imaging diagnostics*, Applied Optics, 37 (1998), pp. 4963–4978.

[57] A. L. Velikovich and G. Dimonte, *Nonlinear perturbation theory of the incompressible Richtmyer-Meshkov instability*, Phys. Rev. Let. 76 (1996), pp. 3112–3115.

[58] I. Waitz, F. Marble, and E. Zukoski, *An investigation of a contoured wall injector for hypervelocity mixing augmentation*, in 27th AIAA, SAE, ASME, and ASEE Joint Propulsion Conference, Sacramento, CA, June 24-26, 1991.

[59] Q. Zhang and S. Sohn, *Nonlinear theory of unstable fluid mixing driven by shock waves*, Phys. Fluids, 5 (1997), pp. 417–425.